Journal of Electromagnetic Analysis and Applications

ISSN: 1942-0730 (Print), 1942-0749 (Online)

Volume 2, Number 1, January 2010

www.scirp.org/journal/jemaa

Scientific Research

JOURNAL EDITORIAL BOARD

ISSN: 1942-0730 (Print) 1942-0749 (Online)

http://www.scirp.org/journal/jemaa

J. Electromagnetic Analysis & Applications, **2010**
Published Online January 2010 in SciRes (www.SciRP.org/journal/jemaa)

CONTENTS

Vol. 2 No. 1 **January 2010**

Journal of Electromagnetic Analysis and Applications (JEMAA)

Journal Information

SUBSCRIPTIONS

The *Journal of Electromagnetic Analysis and Applications* (Online at Scientific Research Publishing, www.SciRP.org) is published quarterly by Scientific Research Publishing, Inc., USA.

E-mail: jemaa@scirp.org

Subscription rates: Volume 2 2010

Print: $50 per copy.

Electronic: free, available on www.SciRP.org.

To subscribe, please contact Journals Subscriptions Department, E-mail: jemaa@scirp.org

Sample copies: If you are interested in subscribing, you may obtain a free sample copy by contacting Scientific Research Publishing, Inc at the above address.

SERVICES

Advertisements

Advertisement Sales Department, E-mail: jemaa@scirp.org

Reprints (minimum quantity 100 copies)

Reprints Co-ordinator, Scientific Research Publishing, Inc., USA.

E-mail: jemaa@scirp.org

COPYRIGHT

PRODUCTION INFORMATION

For manuscripts that have been accepted for publication, please contact:

E-mail: jemaa@scirp.org

J. Electromagnetic Analysis & Applications, **2010, 2: 1-6**
doi:10.4236/jemaa.2010.21001 Published Online January 2010 (http://www.SciRP.org/journal/jemaa)

Coupling of the Magnetostriction and Hall Effect in the Porous Magnetorheological Composite

Stanislaw BEDNAREK

Department of Physics and Applied Informatics, University of Lodz, Lodz, Poland.
Email: bedastan@uni.lodz.pl

Received August 4th, 2009; revised September 13th, 2009; accepted September 20th, 2009

ABSTRACT

The first part of this paper is presents a method for producing the composite which shows ferromagnetic, highly-elastic and electrically-conducting properties. This composite consists of ferromagnetic particles of the size 0.15-0.25 *mm made of the chemically pure iron. The mentioned particles were dispersed in the elastic porous silicone the matrix with pores of the size* 0.15-0.25 *mm. Colloidal graphite particles of the size not exceeding* 0.5 μm *were added to the matrix to increase electrical conductivity. The production method consist in mixing particles of iron, graphite and sodium chloride with non-polymerized silicone and rinsing salt particles by water after the matrix polymerization. In its second part the paper provides a description of the measurement system for longitudinal magnetostriction and the Hall voltage. The magnetic field with the induction of* ± 8 *T produced by the Bitter type magnet was applied to the composite samples. The supplying voltage was applied to these samples and the Hall voltage was measured at the electrodes glued to them. The longitudinal magnetostriction was measured by means of the capacitor with a variable capacity placed at the upper surface of these samples. The linear magnetostriction exceeding* ± 6 *% and the Hall voltage reaching* ± 5.5 *nV were detected by the conducted measurements. Both the longitudinal magnetostriction and the Hall voltage show nonlinear changes and hysteresis lopes during the magnetic field application and the supplying current flow. The coupling of these changes and other regularities observed in the investigated composites and especially their non-linearity and hysteresis, are discussed in the final part of the paper.*

Keywords*: *Hall Effect, Magnetostriction, Non-linearity, Hysteresis, Composite, Porous, Elastic, Ferromagnetic

1. Introduction

The mechanism of magnetostriction involves the changes in the dimension of the magnetized body as a result of its magnetization when placed in the external magnetic field [1,2]. The Hall effect refers to the potential difference on the opposite sides of an electrical conductor through which an electric current is flowing, created by a magnetic field with induction perpendicular to the current flow [3,4]. In normal conductors each of these phenomena appears to occur independently and thus is discussed independently. The paper aims to present both the measurement results of the longitudinal magnetostriction and the Hall voltage. These measurements have been obtained using the samples of elastic porous ferromagnetic composite.

2. The Preparation of Samples

For the measurements, the samples in a cuboid shape, size: 35 mm long, 21 mm wide, and 21 mm high, were used. The sample dimensions in horizontal cross-section were restricted by the Bitter magnet aperture. The magnet with the 43 mm aperture was used to create a magnetic field. The width-to-length ratio of 5:3 of a sample measuring approximately 35 by 21 mm, was assumed. The structure of the samples produced is presented in the cross-section in Figure 1 [5]. Prior to the sample production, the composites containing ferromagnetic particles of chemically pure iron, size 0.15-0.25 mm, as well as the particles of colloidal graphite of the size not exceeding 0.5 μm, were produced first. The pores in the samples were produced through resolving and rinsing sodium chloride grains of the size 0.15-0.25 mm. The particles of iron and sodium chloride of desirable sizes were obtained as a result of grinding and sieving.

In order to produce the composites, chemically pure particles of iron, sodium chloride particles and colloidal graphite particles were measured in appropriate proportions. The quantity of the particles used for the mixture was determined by the filling factor p_s [6,7]. The filling factor is defined as the ratio of the volume of a given

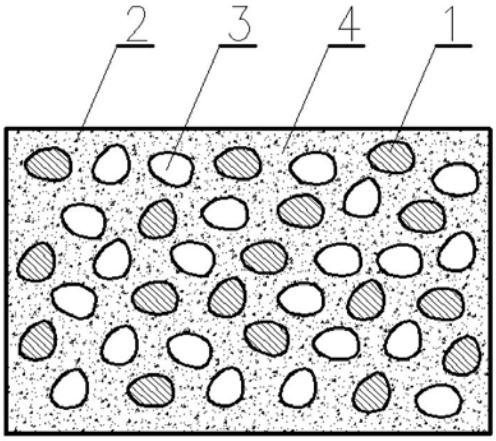

Figure 1. Structure of the elastic, porous, ferromagnetic composite presented in cross section: 1—particle of chemically pure iron with dimensions 0.15-0.20 mm, 2—particle ofcolloidal graphite with dimensions not exceeding 0.5μm, 3—pore with dimensions 0.15-0.20mm, 4—silicone matrix

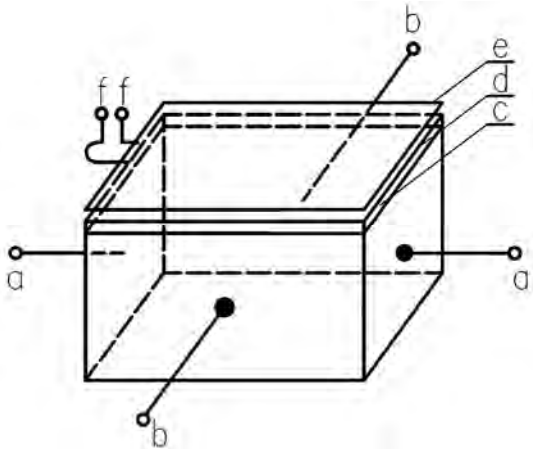

Figure 2. Preparation of the connections of sample to measurements: a-a—ends of the supply Voltage wires, b-b—ends of wires for the Hall voltage measurement, c—pad made ofTeflon, d—movable capacitor plate, e—immovable capacitor plate, f-f—ends of capacitor plates

component V_s to the total composite volume V_k, which can be expressed by the general formula:

$$p_s = \frac{V_s}{V_k} \tag{1}$$

The volumes of particles were mixed together for 15 min.

A bonding substance was added to the mixture which constituted the composite matrix. The substance contained non-polymerized silicone available commercially as the adhesive/sealing mass. The silicone has a gel consistency and is sold in hermetically sealed tubes as it contains polymerization initiator which is easily activated by atmospheric air. The particles were mixed with a measured quantity of silicone for 20 min. The mixture obtained in the process was formed into cuboid shape at the above mentioned sizes.

The cuboids which were obtained from the mixture were left to remain at the temperature of 20 ºC for 48 hours, during which time a complete polymerization of silicone occurred. Subsequently, pores were produced through resolving and rinsing sodium chloride. To obtain this effect, the cuboid was submitted to the water flux and was periodically kneaded with hands. The successive resolution and rinsing of sodium chloride were conducted for 3 hours. Following the process of pore formation the samples obtained in the process were dried up in the flux of hot air produced by the supercharger at the temperature of 35 ºC.

3. The Measurement System

The way of establishing connections between the composite sample and the measurement process is outlined in Figure 2. In the centers of the two opposing walls which make squares at 21 mm at one side, the ends of wires *a-a* were glued as a means for supplying voltage. Impacted by the voltage activity, an electric current flowed through the sample causing the Hall effect. To glue the ends, graphite glue composed of colloidal graphite and non-polymerized silicone was applied for better contact and conductivity, with a volume filling factor for graphite of 0.6.

Then, in the centers of the two opposite sides making rectangles of 35 by 21 mm at the sides, the ends of wires *b-b* were glued for measuring the Hall voltage. The same graphite glue was applied to attach the ends. At the top of the sample, the pad *c* made of 1 mm thick Teflon, was applied to the sample with a pure non-polymerized silicone. An electrode *d* in the form of a rectangular strip of copper foil was also glued with pure silicone.

The electrode consisted of a movable plate of the condenser with a variable capacity, which was employed to measure magnetostriction [8]. Non-movable plate *e* of the condenser was a rectangular strip of copper foil of the identical size as the movable plate. Into the edge of each of the plates, the ends of wires *f-f* were soldered to connect them to the capacity meter. The end of wire connected to the movable pad was made of a flexible material such as lice and supplied with a loop. Such a solution allowed for an easy adjustment of the necessary distance between the capacitor plates.

The setup applied for the simultaneous measurements of the Hall voltage and longitudinal magnetostriction is presented in Figure 3. A sample of elastic porous ferromagnetic composite 1 of the dimensions provided above was placed on a horizontal insulation base plate 2 of textolite. The base plate was fastened into two vertical brass rods 3 and inserted into the aperture of the Bitter magnet coil 4. The ends of wires for the voltage supply *a-a* as

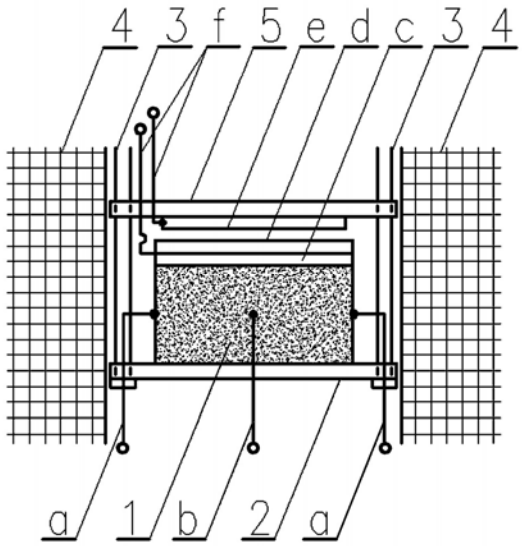

Figure 3. Construction of the measurement system: 1—sample of elastic, porous, ferromagnetic composite, 2—basis, 3—brass rood, 4—winding of Bitter magnet coil, 5—insulating plate; the remaining letters have the same significance as in caption under Figure 2

well as the ends for measuring the Hall voltage *b-b* were glued into the sample. The sample was fixed with a pad *c* of Teflon and a movable condenser plate *d*. Above the sample on the rods 3 an isolation plate 5 cut out from an electrical insulating material—textolite was placed, to which immovable capacitor plate *e* was attached. The ends *f-f* were soldered into each of the capacitor plates connecting them into the bridge specially designed for measuring capacitance. The sensitivity of the bridge amounted to 0.01 pF.

The Bitter magnet at the International Laboratory of the High Magnetic Field and Low Temperatures in Wroclaw was employed to generate the magnetic field in which the sample was placed. The magnet could practically create the magnetic fields with the maximum induction 8 T, with an option to invert their direction. The supply voltage of 3000 V came from the constant current generator. To disperse the Joule heat produced by the current flow, the magnet coil was cooled with water flowing along axial direction.

4. The Discussion of Results

While using the setup described above, the measurements of the Hall voltage U_H and longitudinal magnetostriction—measured by the relative elongation $\Delta l/l_0$ on dependence of the magnetic induction of B the applied magnetic field—were conducted. The magnetic field induction was changed from 0 T to + 8 T and to – 8 T, and eventually to 0 T. The measurements were carried out for the samples with varied filling factors for ferromagnetic particles of chemically pure iron p_f, and for colloidal graphite particles p_g, with the filling factor for ferromagnetic particles amounting to 0.3, 0.2 or 0.1 and correspondingly for graphite particles to 0.2 or 0.3. However, the porosity factor p_p amounted to 0.2 and remained constant for all the samples. In sum, five samples were investigated. The results of the Hall voltage dependencies U_H and longitudinal magnetostriction $\Delta l/l_0$ on the value of the magnetic induction B are presented in Figure 4-8. To obtain the curves as presented in the figures, the least square method was applied [9].

When analyzing the charts it is easy to observe that the dependences of both the Hall voltage U_H and longitudinal magnetostriction $\Delta l/l_0$ on the value of the magnetic field induction B have a non-linear character. A review of the hitherto known cases of the occurrence of the Hall effect in conductors and semiconductors, the Hall voltage revealed a linear dependence on the value of the magnetic field induction B [7]. The evidence of non-linearity ascertained in our investigation can be regarded as something of a novelty. Together with the increase in the magnetic field induction B, there is an increase in the Hall voltage U_H and longitudinal magnetostriction [10,11]. The extreme Hall voltage amounting to 5.5 nV in the magnetic field with the induction of 8 T was found in the sample with the following filling factors: $p_f = 0.3$, $p_g = 0.2$, $p_p = 0.2$ and in the sample with the filling factors: $p_f = 0.2$,

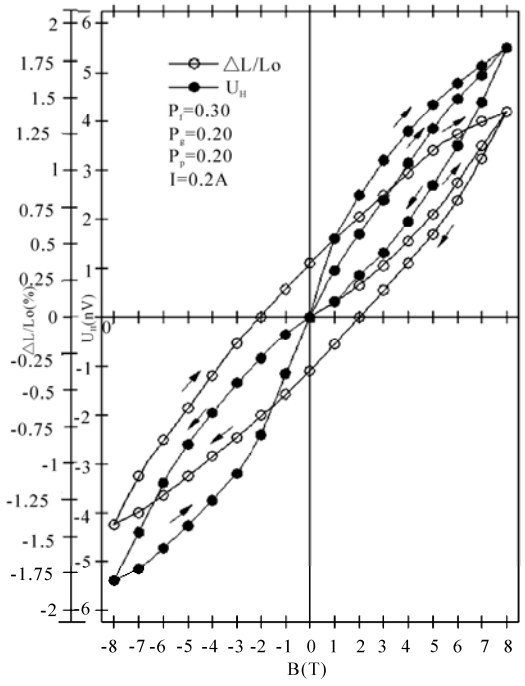

Figure 4. Dependences of longitudinal magnetostriction $\Delta l/l_0$ and the Hall voltage U_H on the magnetic induction B for sample with filling factor for with ferromagnetic particles $p_f = 0.3$, filling factor for graphite particles $p_g = 0.2$, porosity factor $p_p = 0.2$. The intensity of supply current I = 0.2 A

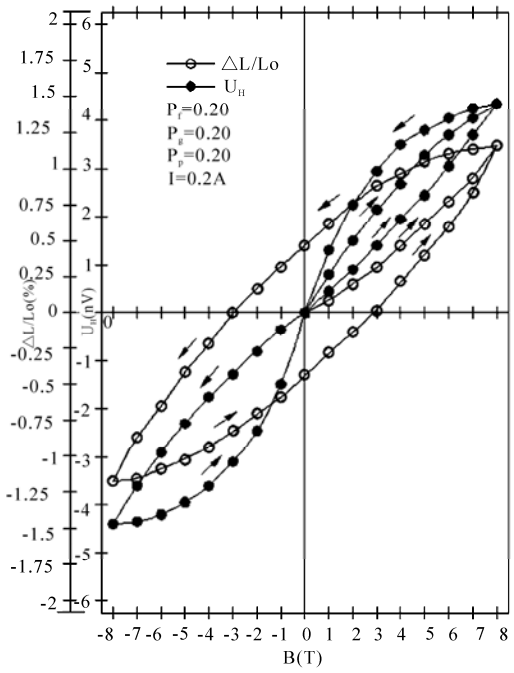

Figure 5. Dependences of longitudinal magnetostriction $\Delta l/l_0$ and the Hall voltage U_H on the magnetic induction B for sample with filling factor for ferromagnetic particles p_f = 0.2, filling factor for graphite particles p_g = 0.2, porosity factor p_p = 0.2. The intensity of supply current I = 0.2 A

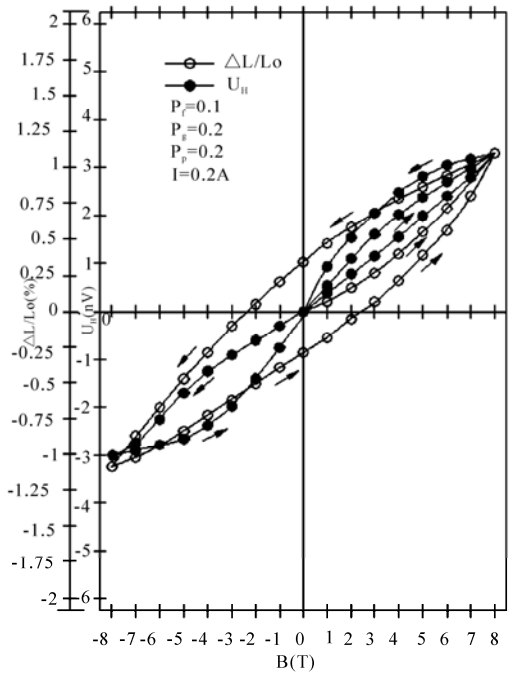

Figure 6. Dependences of longitudinal magnetostriction $\Delta l/l_0$ and the Hall voltage U_H on themagnetic induction B for sample with filling factor for ferromagnetic particles p_f = 0.1, filling factor for graphite particles p_g = 0.2, porosity factor p_p = 0.2. Theintensity of supply current I = 0.2 A

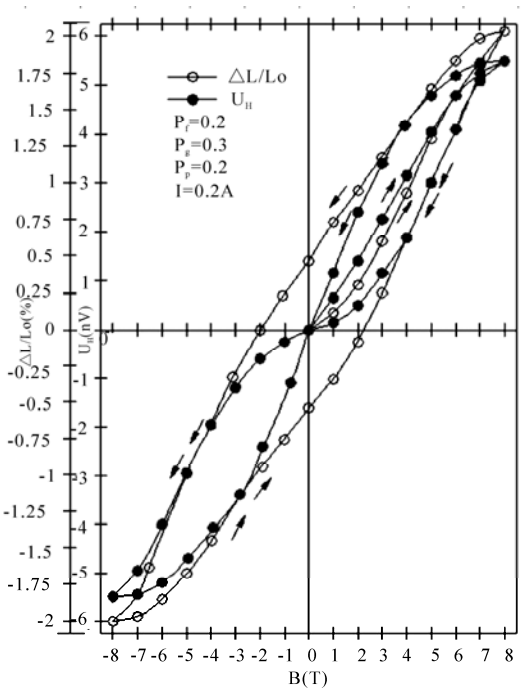

Figure 7. Dependences of longitudinal magnetostriction $\Delta l/l_0$ and the Hall voltage U_H on the magnetic induction B for sample with filling factor for ferromagnetic particles p_f = 0.2, filling factor with graphite particles p_g = 0.3, porosity factor p_p = 0.2. The intensity of supply current I = 0.2 A

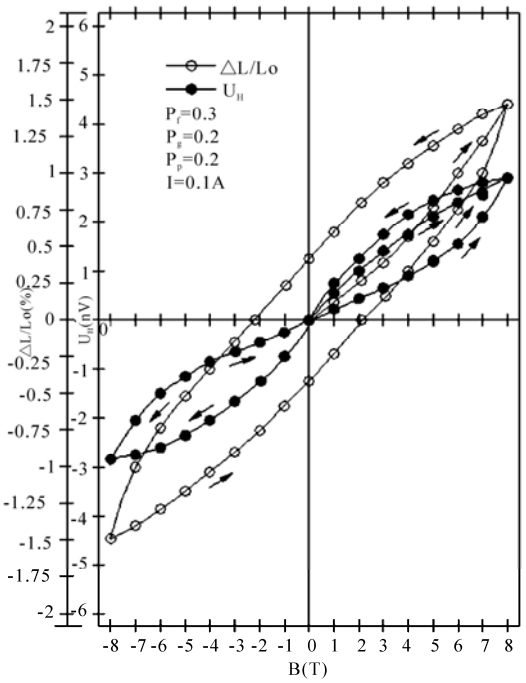

Figure 8. Dependences of longitudinal magnetostriction $\Delta l/l_0$ and the Hall voltage U_H on the magnetic induction B for sample with filling factor for ferromagnetic particles p_f = 0.3, filling factor with graphite particles p_g = 0.2, porosity factor p_p = 0.2. The intensity of supply current I = 0.1 A

$p_g = 0.3$, $p_p = 0.2$.

The extreme value of longitudinal magnetostriction $\Delta l/l_0$ amounting to 6.1% was found in the sample with the filling factors $p_f = 0.2$, $p_g = 0.3$, $p_p = 0.2$ with the magnetic field induction 8 T. The ascertained value of magnetostriction may be compared with a gigantic magnetostriction which is found in the alloys of rare earth elements such as dysprosium and terbium [1,2]. Yet, there is a real difference between these materials. The dysprosium and terbium alloys have a significantly more measures of the Young's modulus than the samples of the composite under investigation. For that reason, the potential energy of elasticity which has been accumulated in the deformed sample is far smaller than the energy of elasticity in the alloys of rare earth elements or nanocomposite materials [12,13]. The difference may prove to be important in the case of application of the investigated composite, e.g. in the construction of electromechanical transductions and sensors.

The dominant cause of a giant magnetostriction in the investigated composite is the deformation of porous silicone matrix after it has been placed in the magnetic field. In a model way, it was presented in Figure 9. Ferromagnetic particles undergo magnetization and tend to pitch in such a way that the directions of their easy magnetization follow the magnetic field lines. As a result of this, the magnetized particles act at the matrix causing its elongation. The porosity of the matrix is the factor which helps its elongation, as the fine walls of the matrix are apt to yield to bending and tension easier [14]. Some contribution to the sample magnetostriction is also made by the magnetostriction of the particles and the matrix themselves. Yet, this contribution is insignificant.

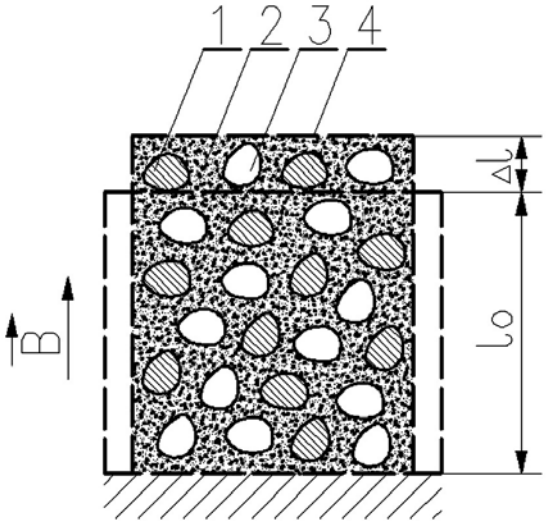

Figure 9. Structure of elastic, ferromagnetic porous composite after elongation presented in cross section: l_0—initial length, Δl—elongation, B—value of the magnetic field induction decisive significance for creation of magnetostriction in investigated composites the remaining symbols have the same significance as in caption under Figure 1

The maximal values of the Hall voltage UH and longitudinal magnetostriction Δl/l0 depend on the composition of the composite sample. When analyzing Figure 4-6, it is evident that a decrease in the content of the che- mically pure iron particles, measured by coefficient p_f from 0.3 to 0.1 has caused a reduction of the maximal value of the Hall voltage from 5.5 nV to 3 nV and reduction of the maximal value of magnetostriction from 1.27 % to 1.03 %. In turn, an increase in the content of graphite particles measured by the increasing factor pf from 0.2 to 0.3 caused an increase in the maximal Hall voltage from 3 nV to 5.5 nV (see Figure 6 and 7).

The increasing maximal value of magnetostriction with the increase in ferromagnetic particles content can be explained by the fact that the samples with greater ferromagnetic particles content interact with the magnetic field more strongly. These samples undergo greater deformation in the same magnetic field, which signifies greater magnetostriction. Subsequently, an increase in the maximal Hall voltage value together with the growth of both ferromagnetic particles content and graphite particles content can be easily explained by the increase in the electrical conductivity of the samples [14].

Both the Hall voltage U_H and longitudinal magnetostriction $\Delta l/l_0$ show hysteresis, manifested in the decelerations of changes of their quantities in ratio to changes of the magnetic field induction. The hysteresis loop of magnetostriction shows a form which resembles an ellipse, however hysteresis loop of the Hall voltage has a form of an inclined number eight.

5. Conclusions

The conducted investigations of the porous magnetorheological composite enable to formulate the following conclusions:

1) The measured longitudinal magnetostriction $\Delta l/l_0$ and the Hall voltage U_H show a non-linear dependence on the induction of the applied magnetic field B. This non-linearity is characteristic of inhomogeneous media such as composites and mixtures, for example [15,16].

2) The maximal achieved values of the longitudinal magnetostriction $\Delta l/l_0$ and the Hall voltage U_H are dependent on the filling factor of the composite by ferromagnetic particles, graphite particles and its porosity factor. Influences of these factors are competitive.

3) Both the longitudinal magnetostriction $\Delta l/l_0$ and the Hall voltage U_H show hysteresis lopes. The main difference between these lopes lies in the zero value of the Hall voltage U_H for the zero value induction of the magnetic field B and the non-zero value of the longitudinal magnetostriction $\Delta l/l_0$ for this B value. One possible case of this hysteresis appears to be the interaction at interfaces between particles and the matrix and the interrup-

tion of their connection [14,17].

4) The magnetic interaction of iron particles with the magnetic field and the elastic susceptibility of silicone matrix are of decisive significance for creation of the magnetostriction in the investigated composites [18].

5) The detected values of the longitudinal magnetostriction $\Delta l/l_0$ in the investigated composite are comparable with values of the giant magnetostriction in the alloys of rare earth elements and nanocomposite materials [12,13], but this composite shows a significantly smaller Young modulus and accumulation of a smaller elastic energy during deformation.

6. Acknowledgements

The investigations described in this article were carried out in the International Laboratory of High Magnetic Fields and Low Temperatures in Wroclaw. The author would like to express his gratitude to Professor Tomasz Palewski, the Director of this Laboratory for Research, for giving me a possibility of using the Bitter's magnet in this Laboratory in these investigations.

REFERENCES

[1] J. B. Restoroff, "Magnetosrtictive materials and devices," In G. L. Trigg, Edition, Encyclopedia of Applied Physics, VCH Publisher Inc., Berlin, New York, Tokyo, Vol. 9, pp. 229–244, 1994.

[2] M. R. Ibarra Garcia, "Magnetoelasticity," In F. Bassani, G. L. Liedl, P. Wyder, Edition, Encyclopedia of Condensed Matter Physics, Elsevier-Academic Press, Amsterdam, Vol. 3, pp. 245–248, 2005.

[3] O. P. Hansen, "Electronic transport in solids," In G. L. Trigg, Edition, Encyclopedia of Applied Physics. VCH Publisher Inc., Berlin, New York, Tokyo, Vol. 6, pp. 121–136, 1993.

[4] J. Bass, "Conductivity: Electrical," In F. Bassani, G. L. Liedl, P. Wyder, Edition, Encyclopedia of Condensed Matter Physics., Elsevier-Academic Press, Amsterdam, Vol. 1, pp. 219–234, 2005.

[5] S. Bednarek, "Composite magnetic materials and production method of thereof," PL. Patent 184,856, January 23rd, 2003.

[6] L. M. Malkinski, "A comparison between two magneto-mechanical methods," Journal of Magnetism and Magnetic Materials, Vol. 140–144, pp. 2169-2170, 1995.

[7] H. Ibach and H. Lüth, "Solid-state physics: An introduction to principles of materials science," Springer-Verlag, Berlin, Heidelberg, 1995.

[8] F. Kohlrausch, "Praktische physik, Verraten über Herman Ebert und Edward Justi," Band II, Verlagesellschaft, Stuttgart, 1956.

[9] G. L. Squires, "Practical physics," Cambridge University Press, Cambridge, 1985.

[10] J. M. Gindr, "Rheology controled by magnetic fields," In Trigg, G. L. Edition, Encyclopedia of Applied Physics, VCH Publisher Inc., Berlin, New York, Tokyo, Vol. 16, p. 487–503, 1996.

[11] M. Le Floc'h, J. L. Mettei, P. Laurent, O. Minot, and A. M. Konn, "A physical model for heterogeneous magnetic materials," Journal of Magnetism and Magnetic Materials, Vol. 140–144, pp. 2191–2192, 1995.

[12] R. Fischer, T. Sherfl, H. Kronmüller, and J. Fiedler, "Phase distribution and computed magnetic properties of high-remanent composite magnets," Journal of Magnetism and Magnetic Materials, Vol. 150, pp. 329–338, 1995.

[13] M. Jurczyk and J. Jakubowicz, "Nanocomposite $Nd_2(Fe, Co, Cr)_{14}B/\alpha$-Fe materials," Journal of Magnetism and Magnetic Materials, Vol. 185, pp. 65–78, 1998.

[14] E. Pippel and J. Woltersdorf, "Interfaces in composite materials," Acta Physica Polonica, Vol. 89, pp. 209–218, 1996.

[15] C. Xu and Z. Li, "The effective dielectric response of nonlinear coated granularcomposites," Physics Letters A, Vol. 252, pp. 233–238, 1999.

[16] E. Laurila, "On the magnetic permeability of mixtures containing ferromagnetic particles and porous ferromagnetic materials," Suomealaisen Tiedeakademian Toimituksie, Sarja A, Physica VI, Helsinki, 1961.

[17] S. Bednarek, "Substitute material constants of ternary composite with continuous matrix," Bulletin de la Société des Sciences et des Lettres de Lodz, LVII, Série: Recherches sur les Déformations, LIII, pp. 95–103, 2007.

[18] S. Bednarek, "Investigation of the giant linear magnetostriction and its hysteresis in elastic ferromagnetic composites within a porous matrix," Bulletin de la Société des Sciences et des Lettres de Lodz, LV, Série: Recherches sur les Déformations, XLVII, pp. 107–117, 2005.

J. Electromagnetic Analysis & Applications, 2010, 2: 7-17
doi:10.4236/jemaa.2010.21002 Published Online January 2010 (http://www.SciRP.org/journal/jemaa)

Voltage and Current Mode Vector Analyses of Correction Procedure Application to Clarke's Matrix—Symmetrical Three-Phase Cases

Afonso José do PRADO[1], Sérgio KUROKAWA[1], José Pissolato FILHO[2], Luiz Fernando BOVOLATO[1]

[1]Department of Electrical Engineering, Faculty of Engineering of Ilha Solteira, The São Paulo State University, São Paulo, Brazil;
[2]Department of Electrical Engineering, The State University of Campinas, Campinas, Brazil.
Email: afonsojp@uol.com.br, kurokawa@dee.feis.unesp.br, pisso@dsce.fee.unicamp.br

Received September 4th, 2009; revised October 6th, 2009; accepted October 15th, 2009.

ABSTRACT

Clarke's matrix has been applied as a phase-mode transformation matrix to three-phase transmission lines substituting the eigenvector matrices. Considering symmetrical untransposed three-phase lines, an actual symmetrical three-phase line on untransposed conditions is associated with Clarke's matrix for error and frequency scan analyses in this paper. Error analyses are calculated for the eigenvalue diagonal elements obtained from Clarke's matrix. The eigenvalue off-diagonal elements from the Clarke's matrix application are compared to the correspondent exact eigenvalues. Based on the characteristic impedance and propagation function values, the frequency scan analyses show that there are great differences between the Clarke's matrix results and the exact ones, considering frequency values from 10 *kHz to* 1 *MHz. A correction procedure is applied obtaining two new transformation matrices. These matrices lead to good approximated results when compared to the exact ones. With the correction procedure applied to Clarke's matrix, the relative values of the eigenvalue matrix off-diagonal element obtained from Clarke's matrix are decreased while the frequency scan results are improved. The steps of correction procedure application are detailed, investigating the influence of each step on the obtained two new phase-mode transformation matrices.*

Keywords**:** *Clarke's Matrix, Eigenvector, Eigenvalue, Phase-Mode Transformation, Error Analysis, Non-Symmetrical Lines, Frequency Dependent Parameters*

1. Introduction

Modal transformations are applied to transmission line analyses because, in mode domain, it is easier to represent the frequency influence on the line parameters. Using phase-mode transformation matrices, all electrical parameters and all line representative matrices are obtained in mode domain [1–4]. The line representative matrices become diagonal and the frequency influence can independently be introduced for every mode because the mutual phase couplings are independently included at every mode. Applying frequency dependent line parameters also leads to frequency dependent phase-mode transformation matrices. Because of this, to obtain voltages and currents in phase domain after signal mode propagation, it is necessary to use a convolution procedure [5–10].

An alternative is to change the exact transformation matrices into single real ones. With these single real transformation matrices, any values can be determined in phase or mode domain using only a matricial multiplication [3,11]. The single real transformation matrices can obtain exact modes and diagonal line representative matrices for ideally transposed lines [12–14]. For untransposed lines, the results are not exact. The errors related to the eigenvalues (λ) can be considered negligible for some untransposed three-phase line analyses when Clarke's matrix is applied as the transformation matrix. The data obtained with Clarke's matrix are called quasi-modes. Increasing the asymmetrical geometrical line characteristics, even though the errors of quasi-mode matrix diagonal elements are negligible, the relative values of the quasi-mode matrix off-diagonal elements can be significant when compared to the correspondent eigenvalues (λ).

Based on these hypotheses, Clarke's matrix application is analyzed considering a symmetrical three-phase line and a frequency range from 10 Hz to 1 MHz. The quasi-mode errors related to the eigenvalues (λ) are studied as well as the off-diagonal elements of the λ

quasi-mode matrix. Improving the analyses, frequency scans are also made using the characteristic impedance (Z_C) and the propagation function (γ) calculated from the exact mode values and the quasi-mode ones. Searching for the off-diagonal element relative value minimization, a perturbation approach corrector matrix is applied to Clarke's matrix. The errors and frequency scan analyses are carried out again and the new results are compared to the previous error values. So, with a first-order approximation procedure, the λ quasi-mode off-diagonal element relative values are highly decreased and the frequency spectrum of the processed signals is closer to that of the exact transformation. Neglecting the imaginary part of the new transformation matrix, frequency scan results similar to those from the first order matrix correction are obtained.

From the comparisons carried out using the 10 kHz frequency value, mode voltage and mode current vectors, it is suggested to extend the analyses shown in this paper considering one of the both modes that is not the homopolar reference of the system as the correction procedure application base. Another suggestion is to apply twice the correction procedure where the both modes related to the modal coupling for symmetrical three-phase transmission lines are subsequently used.

2. Mathematical Bases

Searching for more simplicity for phase-mode transformation applied to transposed three-phase lines, single real transformation can be used. One sample of these matrices is Clarke's matrix [3,11]. The exact differential equations that relate the transversal voltages and the longitudinal currents are described below. In this case, the phase-mode transformations (T_V and T_I), the per unit length longitudinal impedance (Z) and the per unit length transversal admittance (Y) matrices are included [1, 5, 7, 10, 12–14].

$$-\frac{d(T_V^{-1}\cdot u_{MD})}{dx} = Z\cdot T_I^{-1}\cdot i_{MD} \quad \textit{and} \quad -\frac{d(T_I^{-1}\cdot i_{MD})}{dx} = Y\cdot T_V^{-1}\cdot u_{MD} \tag{1}$$

u_{MD} and i_{MD} are the voltages and the currents in mode domain, respectively. For transposed three-phase lines, the T_V and T_I matrices are changed into Clarke's matrix represented by T_{CL}. So, the u_{MD} and i_{MD} values are:

$$u_{MD} = T_{CL}\cdot u_F \quad \textit{and} \quad i_{MD} = T_{CL}\cdot i_F \tag{2}$$

For exact eigenvectors (T_V and T_I), the phase-mode relations of Equation (2) are described by:

$$u_{MD} = T_V\cdot u_F \quad \textit{and} \quad i_{MD} = T_I\cdot i_{MD} \tag{3}$$

Using Equations (2) and (3) for transposed three-phase lines, the following relations are obtained:

$$T_V = T_I = T_{CL} \tag{4}$$

The inverse Clarke's matrix is equal to its transposed one and the initial differential equations are changed into:

$$-\frac{d(T_{CL}^T\cdot u_{MD})}{dx} = Z\cdot T_{CL}^T\cdot i_{MD} \quad \textit{and} \quad -\frac{d(T_{CL}^T\cdot i_{MD})}{dx} = Y\cdot T_{CL}^T\cdot u_{MD} \tag{5}$$

The Z and Y matrices in mode domain are:

$$Z_{CL} = T_{CL}\cdot Z\cdot T_{CL}^T \quad \textit{and} \quad Y_{CL} = T_{CL}\cdot Y\cdot T_{CL}^T \tag{6}$$

The Clarke's matrix structure is [3, 11]:

$$T_{CL} = \begin{bmatrix} -1/\sqrt{6} & 2/\sqrt{6} & -1/\sqrt{6} \\ 1/\sqrt{2} & 0 & -1/\sqrt{2} \\ 1/\sqrt{3} & 1/\sqrt{3} & 1/\sqrt{3} \end{bmatrix} \tag{7}$$

Based on Equations (4–7), the eigenvalues of a transposed three-phase line are determined by:

$$l_{CL} = Z_{CL}\cdot Y_{CL} = Y_{CL}\cdot Z_{CL} = \begin{bmatrix} l_a & 0 & 0 \\ 0 & l_b & 0 \\ 0 & 0 & l_0 \end{bmatrix} \tag{8}$$

In this case, the modes are called α, β and 0 (homopolar). The λ_{CL} is described by:

$$l_{CL} = T_{CL}\cdot Z\cdot Y\cdot T_{CL}^T = T_{CL}\cdot Y\cdot Z\cdot T_{CL}^T \tag{9}$$

The impedance characteristic (Z_C) is described by:

$$Z_{C-CL} = \sqrt{Z_{CL}\cdot Y_{CL}^{-1}} = \sqrt{T_{CL}\cdot Z\cdot Y^{-1}\cdot T_{CL}^T} \tag{10}$$

The propagation function is described by:

$$g_{CL} = \sqrt{Z_{CL}\cdot Y_{CL}} = \sqrt{l_{CL}} \quad \textit{or} \quad g_{CL}^2 = l_{CL} \tag{11}$$

Considering a symmetrical untransposed three-phase line, λ_{CL} is not diagonal. The results are called quasi-modes. There is a modal coupling between α and 0 modes and the λ_{CL} matrix becomes the following [3]:

$$l_{NCL} = \begin{bmatrix} l_{Na} & 0 & l_{Na0} \\ 0 & l_{Nb} & 0 \\ l_{Na0} & 0 & l_{N0} \end{bmatrix} \tag{12}$$

For the exact λ matrix, the exact eigenvectors (T_V and

T_I) are applied, obtaining the following:

$$l = T_V \cdot Z \cdot Y \cdot T_V^{-1} = T_I \cdot Y \cdot Z \cdot T_I^{-1} \quad (13)$$

The exact Z and Y matrices in mode domain are:

$$Z_{MD} = T_V \cdot Z \cdot T_I^{-1} \quad and \quad Y_{MD} = T_I \cdot Y \cdot T_V^{-1} \quad (14)$$

The exact modal Z_C matrix is:

$$Z_{C-MD} = \sqrt{Z_{MD} \cdot Y_{MD}^{-1}} \quad (15)$$

The exact modal γ matrix is:

$$g_{MD} = \sqrt{Z_{MD} \cdot Y_{MD}} = \sqrt{l} \quad or \quad g_{MD}^2 = l \quad (16)$$

Applying Clarke's matrix to an actual symmetrical untransposed three-phase line, the quasi-mode results are compared to the exact values through the following equations:

$$error(\%) = \frac{x_{QUASI-MODE} - x_{EXACT}}{x_{EXACT}} \cdot 100 \quad (17)$$

The relative values of the λ_{CL} off-diagonal elements are obtained with the following:

$$l_{KJ-RELATIVE}(\%) = \frac{l_{CL(KJ)}}{l_K \ or \ l_J} \cdot 100 \quad (18)$$

Regarding the frequency scan, the modal couplings among the quasi-modes are neglected. Every mode or quasi-mode is analyzed as in Figure 1 [7].

The propagation wave in Figure 1 is solved by the following system of equations where d is the line length [7].

$$\begin{cases} E_A = E_B \cdot \cosh(g \cdot d) - I_B \cdot Z_C \cdot \sinh(g \cdot d) \\ I_A = -I_B \cdot \cosh(g \cdot d) + \dfrac{E_B}{Z_C} \cdot \sinh(g \cdot d) \end{cases} \quad (19)$$

The system of Equations (19) is applied for every mode considering three situations in the line receiving terminal (the B terminal): opened line, short-circuit and infinite line. The infinite line is calculated using an impedance with the Z_C value connected to the line receiving terminal. For the frequency scan, the line sending terminal is connected to a unitary step voltage source, considering the frequency domain. This voltage source is described by the next equation. The unitary step voltage

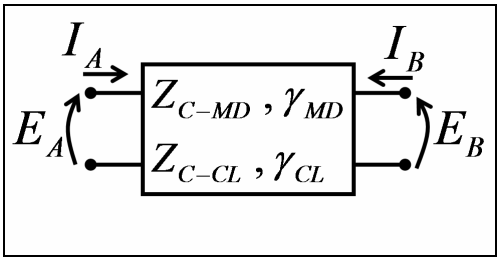

Figure 1. Frequency scan analyses

is chosen because it includes all frequency values. In the case of this paper, the frequency scan analyses are performed with a frequency range from 10 Hz to 1 MHz.

$$E(f) = -j\frac{1}{w} = -\frac{1}{2 \cdot p \cdot f} \quad (20)$$

3. The Actual Symmetrical Three-Phase Line

The interactions between any transposed three-phase line and Clarke's matrix produce exact mode results and the modal representative matrices are diagonal. In case of untransposed three-phase lines, the T_{CL} results are not exact. These results are compared to the correspondent exact values using Equations (17) and (18) as well as the frequency scan.

The actual three-phase line analyzed in this paper has a vertical symmetry and shown in Figure 2.

The central phase conductor height is 27.67 m on the tower. The height of adjacent phase conductors is 24.07 m. Every phase is composed of four conductors distributed in a square shape with 0.4 m side length. Every conductor is an ACSR type one (ACSR-26/7-636 MCM). The phase conductor resistivity is 0.089899 Ω/m and the sag at the midspan is 13.43 m. The earth resistivity is considered constant (1000 Ω.m). The ground wires are EHS 3/8 with the resistivity of 4.188042 Ω/m. The height of these cables on the tower is 36.00 m. The sag of the ground wires at the midspan is 6.40 m.

4. The Error Analyses of the Clarke's Matrix Application

From the Equations (8), (9), (12) and (13), the λ_{NCL} quasi-modes are compared to the eigenvalues using Equation (17). In this case, firstly, the eigenvectors are calculated applying the iterative Newton-Raphson's method. The initial values for this method are frequency of 10 Hz and the Clarke's matrix elements. For this first frequency

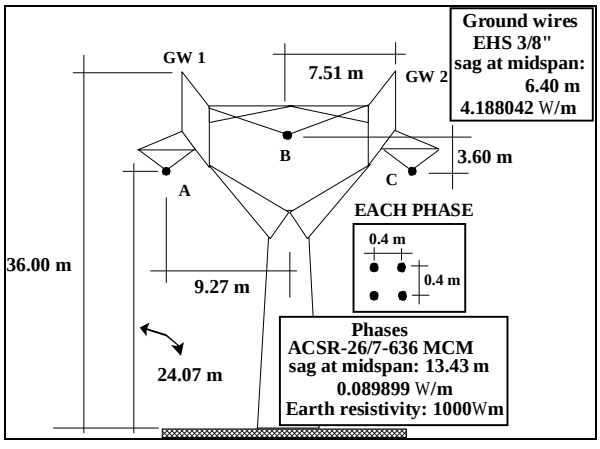

Figure 2. The actual symmetrical three-phase line of Brazil's utilities

value, the iterative processing is started considering the eigenvectors equal to the Clarke's elements. When the iterative processing converges to the exact values, it is restarted with the next frequency value and uses the exact values of the previous frequency value for the reinitialization of the new eigenvectors. After the determination of eigenvectors, the eigenvalues and the comparisons to the quasi-modes are performed for every frequency value [4].

The results of the comparisons between quasi-modes and the eigenvalues are shown in Figure 3. The β quasi-mode presents null errors because this is an exact mode. Also confirming the results of Equation (12), α and 0 quasi-modes are not exact. The α quasi-mode presents the highest error peak among the three shown curves and this peak is about 10 kHz. The range of errors is from -0.3% to 0.2 %. There are inverse signals between the α and 0 quasi-mode error curves. The errors between the quasi-modes and eigenvalues can be considered negligible. These errors are determined using the modulus of the related values. Because of this, it is important to analyze the off-diagonal quasi-mode elements.

It is shown in Equation (12) that there is a modal coupling between the α and 0 quasi-modes. Because the line representative matrices are symmetrical independently of whether the line is symmetrical, or not, the off-diagonal element in the intersection between the matrix first line and the matrix third row is equal to the off-diagonal in the third line and the first row intersection. In Figure 4, this off-diagonal element is compared to the correspondent eigenvalues (the α and 0 modes). If the Clarke's matrix application does not obtain diagonal matrices, the modal coupling can interfere in the signal processing. It depends on the signal spectrum.

In Figure 4, the $\lambda_{N\alpha 0}$ off-diagonal element is compared to the correspondent eigenvalues from Equation (13). When it is compared to the λ_{α} eigenvalue, the $\lambda_{N\alpha 0}$ relative curve gets higher values than the curve obtained from the λ_0 eigenvalue. The highest peak of the curve related to the λ_{α} eigenvalue is close to 18 % and it is associated to the initial frequency values of the considered-frequency range. The curve related to the λ_0 eigenvalue has softer variations than the other curve. Considering both curves presented in Figure 4, the $\lambda_{N\alpha 0}$ relative values decrease when the frequency increases. For low frequency values, the $\lambda_{N\alpha 0}$ modal coupling is more significant then for high frequency values. Based on these results, signal phase-mode transformation comparisons are carried out for analyzed frequency range using Clarke's matrix and the eigenvectors (T_V and T_I). From phase vectors and with the Clarke's matrix application, it is obtained mode vectors where only one mode has non-null value. It is shown in the following Equation:

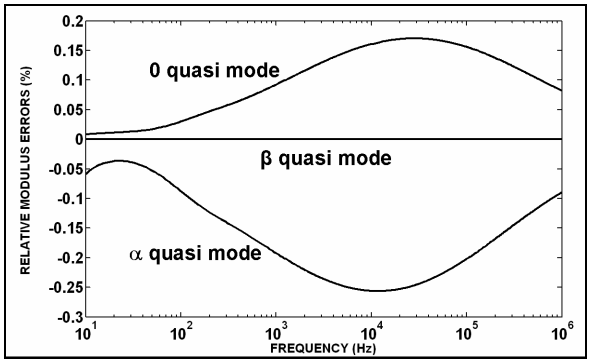

Figure 3. The λ error curves for an actual symmetrical three-phase line

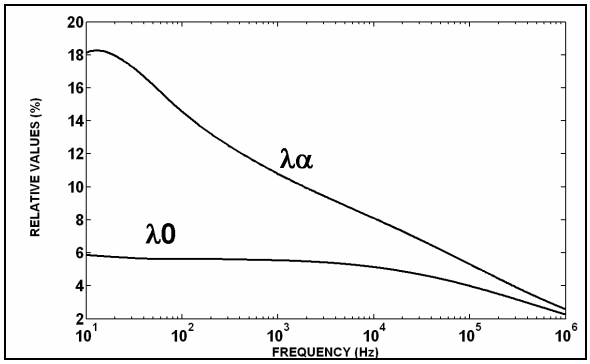

Figure 4. The quasi-mode off-diagonal element for the actual symmetrical three-phase line

$$\begin{bmatrix} V_a \\ V_b \\ V_0 \end{bmatrix}_{CL\,a} = T_{CL} \cdot \begin{bmatrix} -1/\sqrt{6} \\ 2/\sqrt{6} \\ -1/\sqrt{6} \end{bmatrix} = \begin{bmatrix} I_a \\ I_b \\ I_0 \end{bmatrix}_{CL\,a} = \begin{bmatrix} 1 \\ 0 \\ 0 \end{bmatrix}$$

$$\begin{bmatrix} V_a \\ V_b \\ V_0 \end{bmatrix}_{CL\,b} = T_{CL} \cdot \begin{bmatrix} 1/\sqrt{2} \\ 0 \\ -1/\sqrt{2} \end{bmatrix} = \begin{bmatrix} I_a \\ I_b \\ I_0 \end{bmatrix}_{CL\,b} = \begin{bmatrix} 0 \\ 1 \\ 0 \end{bmatrix} \quad (21)$$

$$\begin{bmatrix} V_a \\ V_b \\ V_0 \end{bmatrix}_{CL\,0} = T_{CL} \cdot \begin{bmatrix} 1/\sqrt{3} \\ 1/\sqrt{3} \\ 1/\sqrt{3} \end{bmatrix} = \begin{bmatrix} I_a \\ I_b \\ I_0 \end{bmatrix}_{CL\,0} = \begin{bmatrix} 0 \\ 0 \\ 1 \end{bmatrix}$$

The non-null values are compared to the results obtained from the application of the eigenvectors:

$$\begin{bmatrix} V_a \\ V_b \\ V_0 \end{bmatrix}_a = T_V \cdot \begin{bmatrix} -1/\sqrt{6} \\ 2/\sqrt{6} \\ -1/\sqrt{6} \end{bmatrix} \quad and \quad \begin{bmatrix} I_a \\ I_b \\ I_0 \end{bmatrix}_a = T_I \cdot \begin{bmatrix} -1/\sqrt{6} \\ 2/\sqrt{6} \\ -1/\sqrt{6} \end{bmatrix}$$

$$\begin{bmatrix} V_a \\ V_b \\ V_0 \end{bmatrix}_b = T_V \cdot \begin{bmatrix} 1/\sqrt{2} \\ 0 \\ -1/\sqrt{2} \end{bmatrix} \quad and \quad \begin{bmatrix} I_a \\ I_b \\ I_0 \end{bmatrix}_b = T_I \cdot \begin{bmatrix} 1/\sqrt{2} \\ 0 \\ -1/\sqrt{2} \end{bmatrix} \quad (22)$$

$$\begin{bmatrix} V_a \\ V_b \\ V_0 \end{bmatrix}_0 = T_V \cdot \begin{bmatrix} 1/\sqrt{3} \\ 1/\sqrt{3} \\ 1/\sqrt{3} \end{bmatrix} \quad and \quad \begin{bmatrix} I_a \\ I_b \\ I_0 \end{bmatrix}_0 = T_I \cdot \begin{bmatrix} 1/\sqrt{3} \\ 1/\sqrt{3} \\ 1/\sqrt{3} \end{bmatrix}$$

The results of comparisons between the non-null voltage values of Equation (21) and its correspondent values of Equation (22) are shown in Figure 5. The non-null current values of Equation (21) are compared to their correspondent eigenvector values in Figure 6. In these cases, the non-null values of the Clarke's matrix application are compared to the results of the eigenvector application. The shown results are comparisons among modulus values. In Figure 7, it is shown the deviation angles related to the modal transformations using Clarke's matrix and the T_V eigenvector matrix. These are voltage vector transformations detailed in Equations (21) and (22). In case of Figure 8, the transformations are related to the current comparisons and also based on Equations (21) and (22).

For modal transformations of Z and Y matrices as well as for obtaining of eigenvalues, a transformation matrix and an inverse transformation one are used. Applying the modal transformations to the voltage and current vectors, only one transformation matrix, or its inverse matrix, is necessary. In this case, the transformation could increase the errors related to the quasi-modes. On the other hand, based on mentioned results, the use of quasi mode Z and Y matrices for determining other variables in mode domain could increase the errors observed in Figure 3. Investigating this supposition, the impedance characteristic and the propagation function are calculated from Z_{CL} and Y_{CL} matrices and compared to the correspondent values obtained from Z_{MD} and Y_{MD} matrices. The comparisons are made through Equation (17).

Figure 9 is associated to the Z_C modulus. The Z_C angle is null because this variable is real. Figures 10 and 11 are

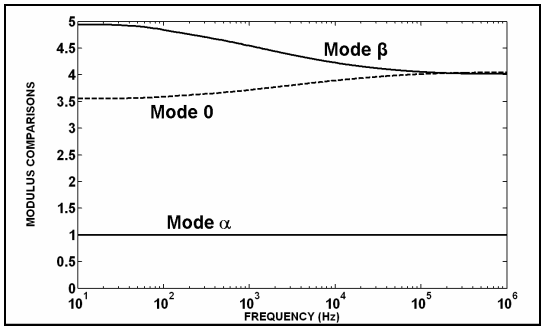

Figure 5. Non-null modulus comparisons among mode voltages (V_{CL}/V) for the T_{CL} matrix application

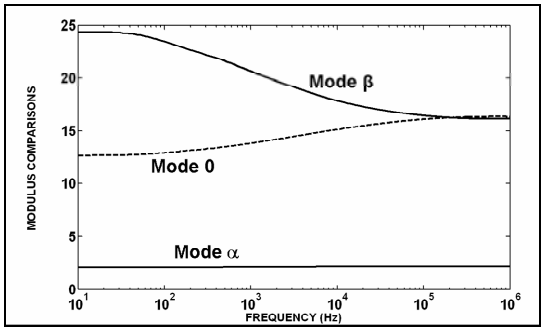

Figure 6. Non-null modulus comparisons among mode currents (I_{CL}/I) for the T_{CL} matrix application

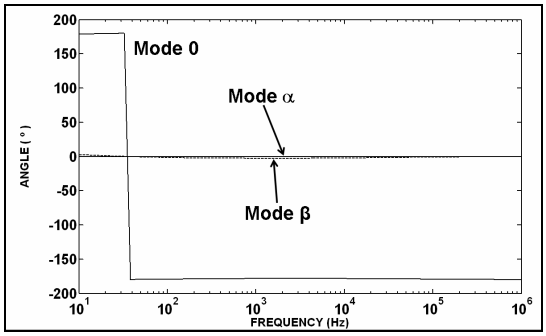

Figure 7. Non-null angle comparisons among mode voltages (V_{CL}/V) for the T_{CL} matrix application

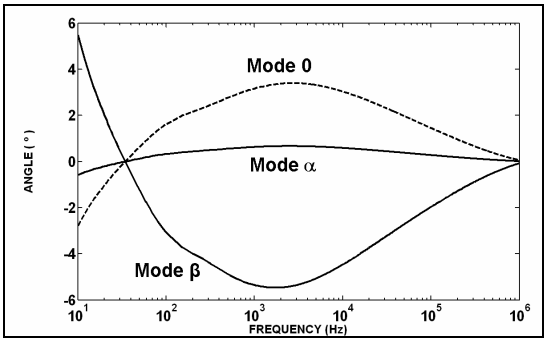

Figure 8. Non-null angle comparisons among mode currents (I_{CL}/I) for the T_{CL} matrix application

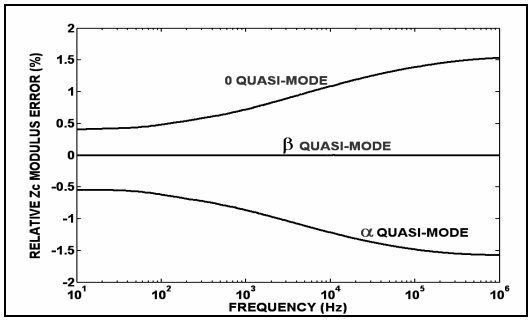

Figure 9. The Z_C modulus errors for the actual symmetrical line

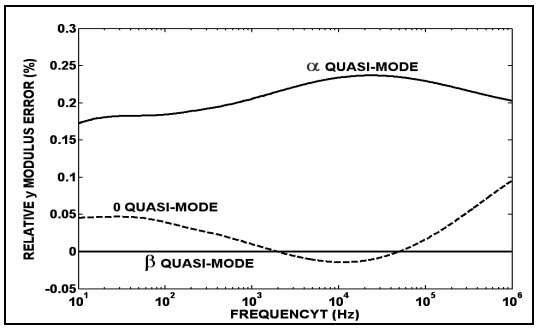

Figure 10. The γ modulus errors for the actual symmetrical line

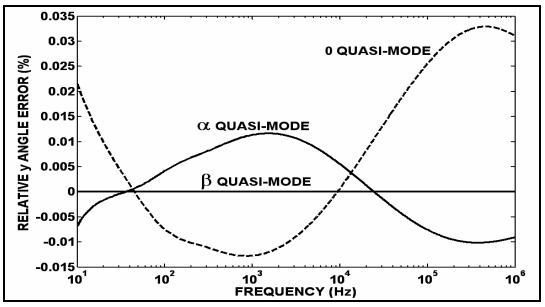

Figure 11. The γ angle errors for the actual symmetrical line

associated to the γ modulus and the γ angle errors, respectively.

Considering the Z_C modulus and the γ angle errors, there are curves with inverse signals (the α and 0 quasi-modes). This characteristic can also be observed in Figure 3.

The range error for the Z_C modulus (from -2 % to 2 %) is about 10 times higher than the γ modulus error range (from -0.05 % to 0.25 %) and it is about 100 times higher than the γ angle error range (from -0.015 % to 0.03 %). So, the Z_C modulus is more sensitive to the errors introduced by Clarke's matrix. The relative values of the off-diagonal element (the Nα0 modal coupling) for Z_C modulus are shown in Figure 12. Based on these results, the $Z_{C\text{-}N\alpha0}$ off-diagonal element influence is significant on the correspondent Z_C quasi-modes.

In Figure 13 as much as in Figure 12, the curves have a crescent tendency from 10 kHz. In Figure 13, the relative values are in a much lower range than that of Figure 12. In Figure 14, the $\gamma_{N\alpha0}$ angle relative values are in a similar range to the $\gamma_{N\alpha0}$ modulus relative values. In this case, the values do not tend to be crescent ones.

5. Frequency Scan Analyses

Frequency scan analyses are based on Figure 1 and Equations (19) and (20) are used [7]. The E_A voltage is described by Equation (20). Three situations of the line receiving terminal (the B terminal) are checked: open line (I_B=0), short-circuit (E_B=0) and infinite line. The infinite line is obtained with an impedance equal to the Z_C value connected in the B terminal of Figure 1. For all these three situations, considering both line terminals, the modulus values of the voltages and the currents obtained

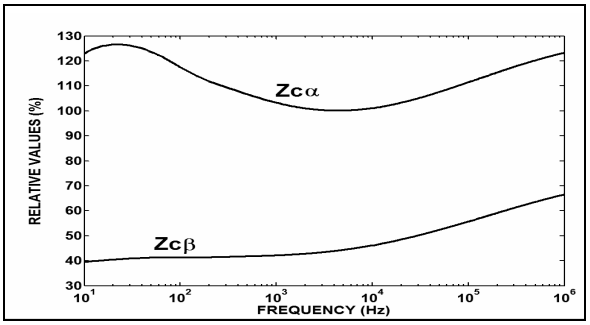

Figure 12. The $Z_{C\text{-}N\alpha0}$ modulus off-diagonal element relative values

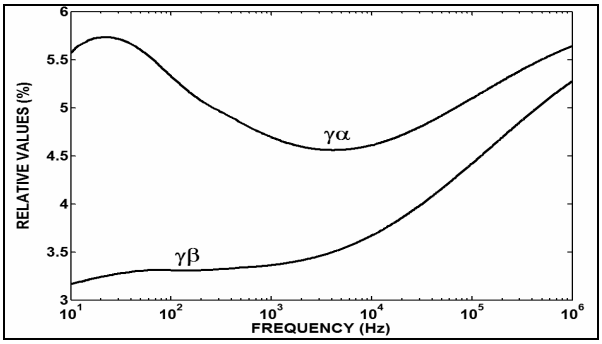

Figure 13. The $g_{N\alpha0}$ modulus off-diagonal element relative values

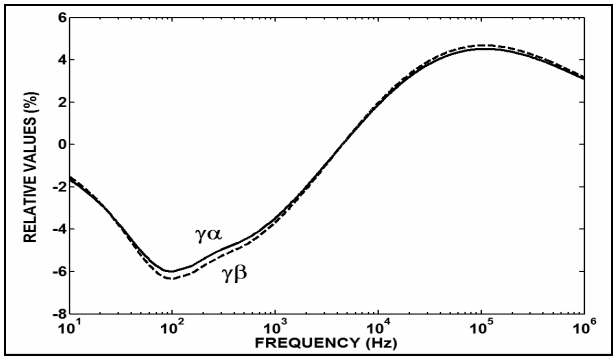

Figure 14. The $g_{N\alpha0}$ angle off-diagonal element relative values

from quasi-modes are equal or very close to the exact values obtained from eigenvectors. The main differences are related to the angle values and the α mode. Showing the results related to the modulus values, Figure 15 presents the B terminal currents for the α mode when this terminal is open. Similar values are presented in Figure 16 considering the 0 mode and the infinite line.

Considering the short-circuit analyses in Figure 17, it is shown that the α quasi-mode and exact angle values are superimposed for frequency values up to 10 kHz. From 10 kHz to 1 MHz, there are great differences between quasi-mode and exact angle values. In this case, the differences are great because the curves present inverse signals related to the horizontal axis.

When the infinite line is analyzed (Figure 18), the obtained results are similar to those present in Figure 17. The quasi-mode and the exact angle values are superimposed for frequency values up to 10 kHz. Above 10 kHz, the differences are great and for some parts of the range, the curves are opposite and present inverse signals. Figure 18 shows results from 10 kHz to 1 MHz.

Based on frequency scan analyses, Clarke's matrix could be applied to transient simulations considering symmetrical untransposed three-phase lines and phenomena with a frequency spectrum concentrated below 10 kHz. For general phenomena, there are classical solutions for this problem based on eigenvector applications. An alternative is to apply a perturbation approach corrector matrix, improving the results of the Clarke's matrix application above 10 kHz. This alternative is described in the next item and based on the homopolar mode.

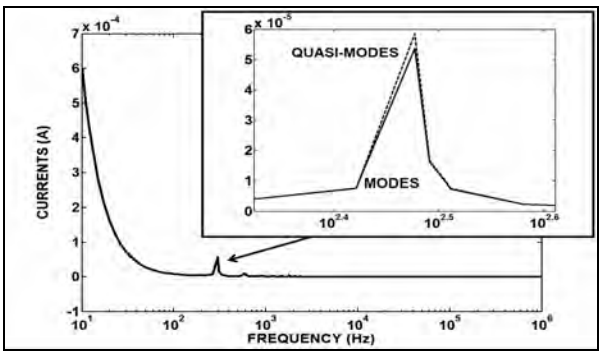

Figure 15. The B terminal currents for the a **mode and the opened line**

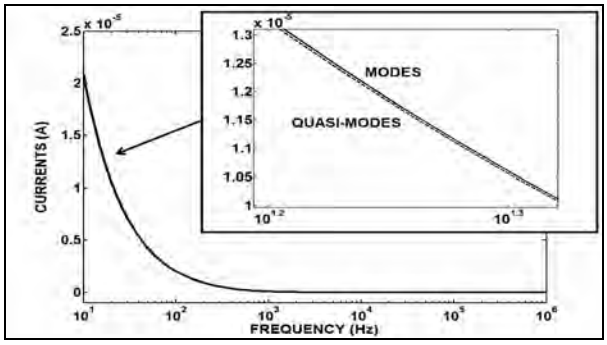

Figure 16. The B terminal currents for the 0 mode and the infinite line

6. The Perturbation Approach Corrector Matrix

The procedure shown in this section is based on a first-order perturbation theory approach [3]. This procedure is used to improve the quasi-mode results and obtain a better approximation to the exact values. Initializing this development, a normalization matrix is defined as:

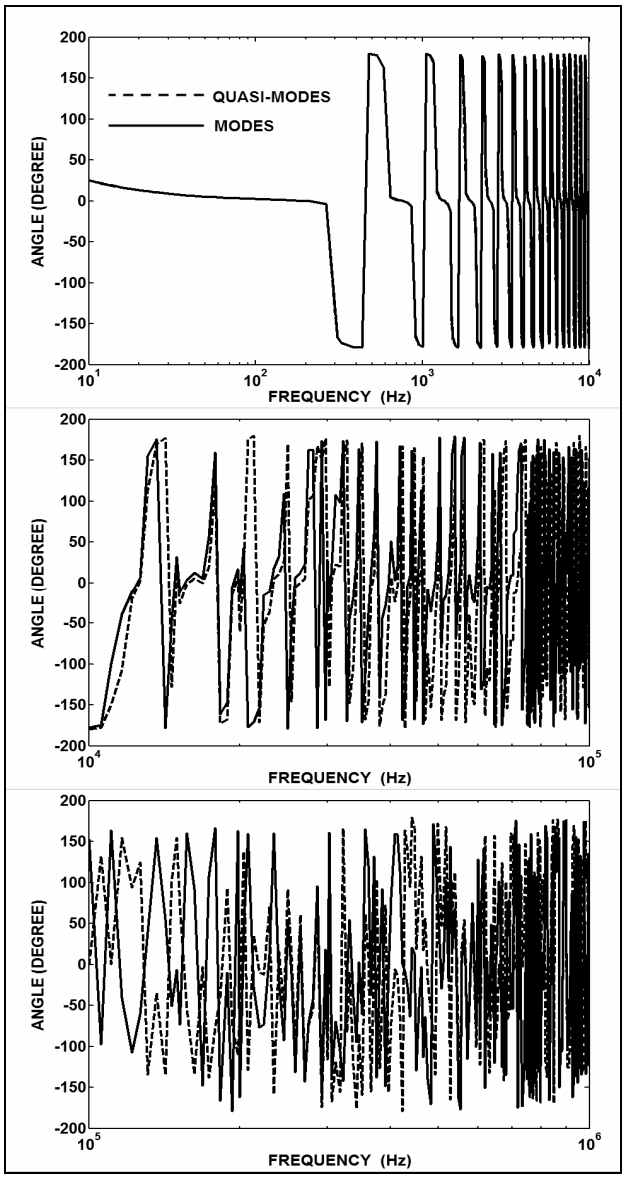

Figure 17. The current angle values for the B terminal with short-circuit (the a **mode)**

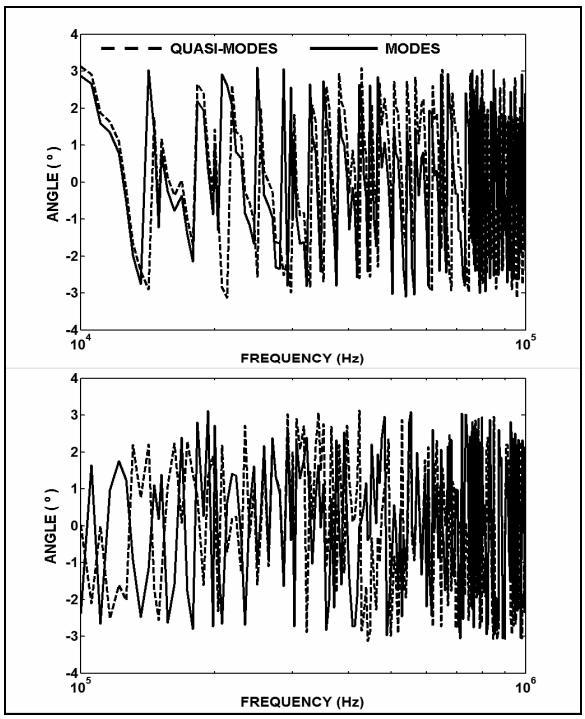

Figure 18. The current angle values for the B terminal with infinite line (the a **mode)**

$$N = \begin{bmatrix} N_{22} & 0 \\ 0 & 1 \end{bmatrix} \tag{36}$$

The N_{22} matrix is defined as:

$$N_{22} = \begin{bmatrix} 1 & n_{12} \\ n_{21} & 1 \end{bmatrix} \tag{37}$$

The normalization matrix is applied to the λ_{NCL} matrix:

$$A = A_V = N^{-1} \cdot T_{CL} \cdot Z \cdot Y \cdot T_{CL}^T \cdot N = \begin{bmatrix} a_a & 0 & a_{a0} \\ 0 & a_b & a_{b0} \\ a_{0a} & a_{0b} & a_0 \end{bmatrix} \tag{38}$$

The described procedure is applied to the T_V and the T_I matrices. For the T_I matrix, the procedure is similar to the T_V one with a change in the position of the Z and Y matrices in Equation (38):

$$A = A_I = N^{-1} \cdot T_{CL} \cdot Y \cdot Z \cdot T_{CL}^T \cdot N = \begin{bmatrix} a_a & 0 & a_{a0} \\ 0 & a_b & a_{b0} \\ a_{0a} & a_{0b} & a_0 \end{bmatrix} \tag{39}$$

The structure of the A matrix is determined from:

$$l = A + (l_{CL} \cdot Q - Q \cdot l_{CL}) \tag{40}$$

The last Equation leads to:

$$\begin{cases} l_K = a_{KK} \\ 0 = a_{JK} + (l_{CL-J} - l_{CL-K}) \cdot q_{JK}, \quad J \neq K \end{cases} \tag{41}$$

The $\lambda_{CL\text{-}\alpha}$ element is equal to the $\lambda_{CL\text{-}\beta}$. Because of this, the a_{12}, a_{21}, q_{12} and q_{21} elements are null. Dividing the λ_{NCL} matrix into blocks, the portioned structure can be described by:

$$l_P = \begin{bmatrix} & & l_{Pa0} \\ & l_{P22} & \\ & & l_{Pb0} \\ l_{P0a} & l_{P0b} & l_{P0} \end{bmatrix} \tag{42}$$

The λ_{P22} is:

$$l_{P22} = \begin{bmatrix} l_{Pa} & l_{Pab} \\ l_{Pba} & l_{Pb} \end{bmatrix} \tag{43}$$

In this case, despite the symmetry of the line representative matrices, small numeric differences are considered between symmetrical elements of the λ_P matrix. The small numeric values of the $\lambda_{P\alpha\beta}$ and $\lambda_{P\beta\alpha}$ are also considered. Using Equations (42) and (43), the a_α and a_β elements are determined by:

$$\begin{cases} a_a = \dfrac{tr(l_{P22}) + \sqrt{tr^2(l_{P22}) - 4 \cdot \det(l_{P22})}}{2} \\ a_b = \dfrac{tr(l_{P22}) - \sqrt{tr^2(l_{P22}) - 4 \cdot \det(l_{P22})}}{2} \end{cases} \tag{44}$$

The N_{22} matrix elements are determined by:

$$n_{21} = \frac{a_a - l_{Pa}}{l_{Pab}} \quad and \quad n_{12} = \frac{a_b - l_{Pb}}{l_{Pba}} \tag{45}$$

In this case, only the Q matrix elements of the third line and the third row can not be null. These elements correspond to the 0 mode and are calculated by:

$$q_{0K} = \frac{a_{0K}}{l_{CL-K} - l_{CL-0}} \quad and \quad q_{J0} = \frac{a_{J0}}{l_{CL-0} - l_{CL-J}} \tag{46}$$

The perturbation approach corrector matrix is described by:

$$W = N \cdot (I + Q) \quad and \quad W^{-1} = (I + Q^{-1}) \cdot N^{-1} \tag{47}$$

The corrected transformation matrix is described by:

$$T_{NV} = W^{-1} \cdot T_{CL-p} \quad and \quad T_{NV}^{-1} = T_{CL-p}^T \cdot W \tag{48}$$

7. Obtained Results

Checking the changes into the Clarke's matrix results carried out applying only the N matrix, it is used the flowchart shown in Figure 19.

The changes obtained from the N matrix application are mainly related to the mode coupling relative values. The peak value is decreased from 18 % to 2 %. It is about a 10 time reduction. The off-diagonal relative obtained after applying the N matrix are shown in Figure 20. On the other hand, there are no expressive changes for the λ relative errors. These values are shown in Figure 21.

Completing the analysis of the influence of N matrix, the results of Figures 22–25 show that the application of this matrix balances equally the phase-mode transformation results obtained from Equation (26) where the T_{CL} matrix is changed into the A_V and A_I matrices.

Another analysis about the correction procedure application to Clarke's matrix is about the Q matrix application. In this case, Figure 26 shows the flowchart related to this matrix application. Figure 27 shows the off-diagonal relative values after the Q matrix application and Figure 28 shows the λ errors for the same case.

In Figures 27 and 28, the shown values decrease when compared to the values presented in Figures 20 and 21. The peak value shown in Figure 27 is about 150 times lower than the correspondent values shown in Figure 4. Comparing Figures 27 and 20, the reduction is about 15 times for the peak values.

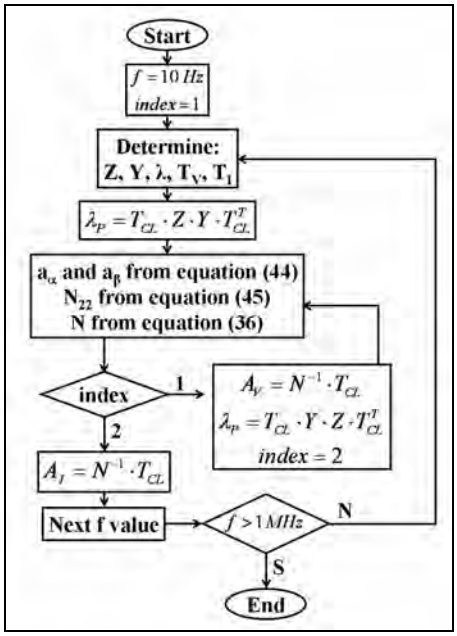

Figure 19. Flowchart for checking of A_N and A_I applications

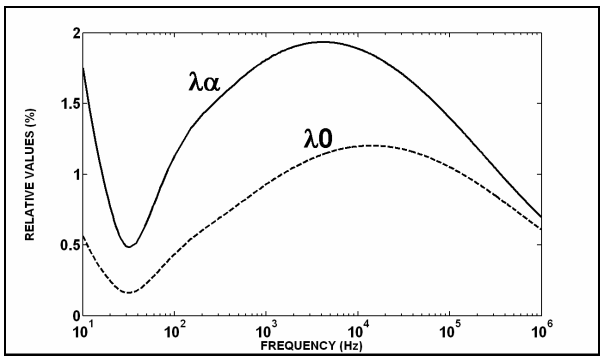

Figure 20. The quasi-mode off-diagonal relative values after the N matrix application

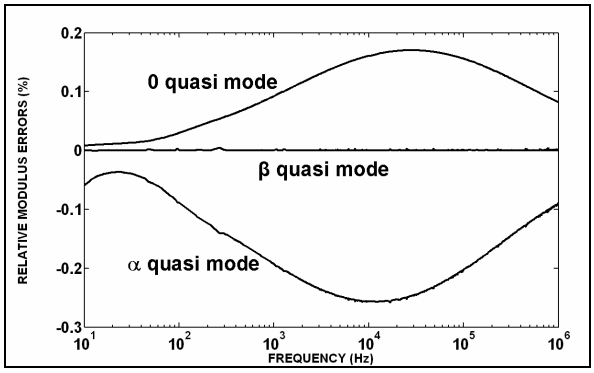

Figure 21. The λ error curves after the N matrix application

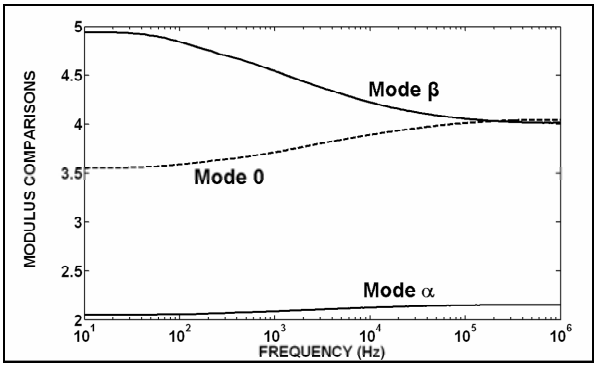

Figure 22. Non-null modulus comparisons among mode voltages (V_{CL}/V) for the N matrix application

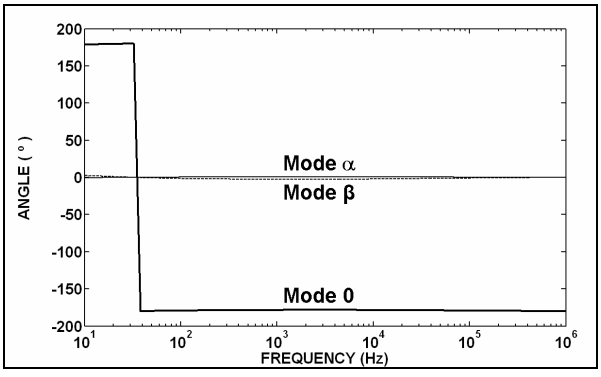

Figure 23. Non-null angle comparisons among mode voltages (V_{CL}/V) for the N matrix application

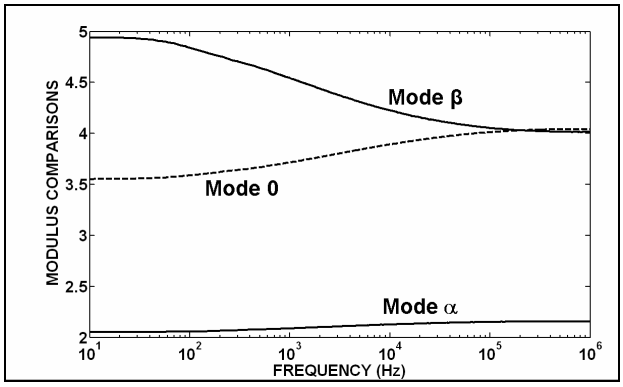

Figure 24. Non-null modulus comparisons among mode currents (I_{CL}/I) for the N matrix application

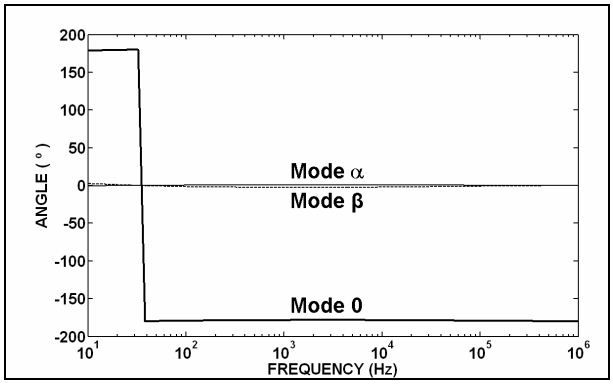

Figure 25. Non-null angle comparisons among mode currents (I_{CL}/I) for the N matrix application

For the λ errors, comparing Figures 3, 21 and 28, the reduction is about 150 times considering the negative peak values shown in these cases.

Applying the Q matrix, the off-relative and the λ errors become negligible. Analyzing the results of both matrices applications, N and Q, it can be concluded that the N matrix mainly acts on the off-diagonal relative values, decreasing them. On the other hand, the Q matrix acts on the λ error and the off-diagonal relative value decreasing.

Analyzing the results shown in Figures 27 and 28, these values can be considered negligible because they are in a very low range of relative values. The peak values reach 0.12 % and -0.002 % in mentioned figures. The shown curves also present some oscillations which, probably, are introduced by the used numeric method. Based, on the results of Figure 29, where it is shown the B terminal α mode current angles for with the short-circuit in the line end, the influence of these numeric oscillations on the propagation wave results is not significant. On the other hand, for future development, if it is possible, these oscillations could be minimized, avoiding the numeric oscillation influence on the determination of Z_C, γ and other electrical variables.

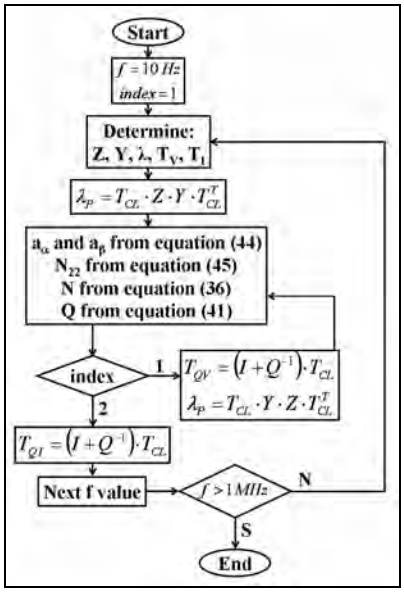

Figure 26. Flowchart for checking of Q matrix applications

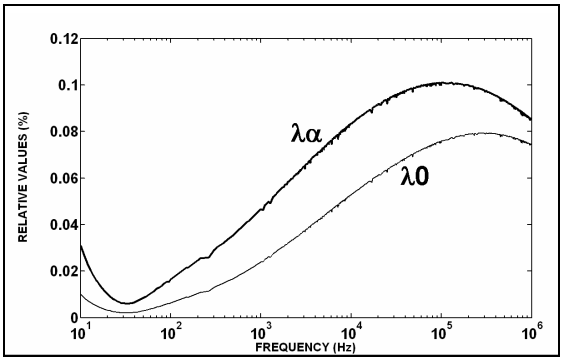

Figure 27. The quasi-mode off-diagonal relative values after the Q matrix application

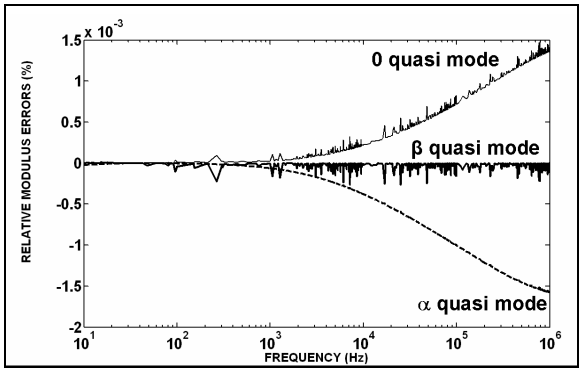

Figure 28. The λ error curves after the Q matrix application

8. Conclusions

Changing eigenvector matrices into Clarke's matrix for untransposed symmetrical three-phase lines leads to small errors related to the exact modulus eigenvalues.

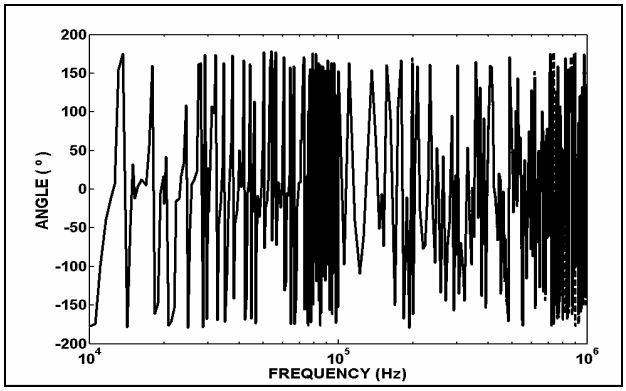

Figure 29. The current angle values for the B terminal with short-circuit (the a **mode), considering the T_{NV} and T_{NI} transformation matrices**

The off-diagonal element of the matrix obtained from the Clarke's matrix application, the quasi-mode eigenvalue matrix, has high relative values when compared to the correspondent exact eigenvalues. Based on these element results, the frequency scan analyses are carried out, showing that there are great differences between the quasi-mode current angles and the exact ones for frequency values above 10 kHz. In this casse, three situations of the line receiving terminal are checked: open line, short-circuit and infinite line.

A correction procedure is applied and new phase-mode transformation matrices are determined: one matrix for voltages and another one for currents.

It is detailed the steps of the correction procedure application, describing the influence of each step on the decreasing of the off-diagonal quasi-mode relative value elements and the quasi-mode matrix ones. One of these steps is the normalization matrix application that carries out balanced voltage and current vectors, obtaining a 150 time reduction of the off-diagonal quasi-mode eigenvalue matrix relative values when compared to the Clarke's matrix application. After this step, the final one reduces about 150 times the λ errors when compared to the Clarke's matrix results. Using the new phase-mode transformation matrices, obtained from the applied correction procedure, the off-diagonal element relative values and the λ errors are highly decreased and could be considered negligible.

REFERENCES

[1] H. W. Dommel, "Electromagnetic transients program—rule book," Oregon, 1984.

[2] Microtran Power System Analysis Corporation, Transients Analysis Program Reference Manual, Vancouver, Canada, 1992.

[3] J. A. Brandão Faria and J. Briceño Mendez, "Modal analysis of untransposed bilateral three-phase lines—a perturbation approach," IEEE Transactions on Power Delivery, Vol. 12, No. 1, January 1997.

[4] T. T. Nguyen and H. Y. Chan, "Evaluation of modal transformation matrices for overhead transmission lines and underground cables by optimization method," IEEE Transactions on Power Delivery, Vol. 17, No. 1, January 2002.

[5] A. Morched, B. Gustavsen, and M. Tartibi, "A universal model for accurate calculation of electromagnetic transients on overhead lines and underground cables," IEEE Transaction on Power Delivery, Vol. 14, No. 3, pp. 1032–1038, July 1999.

[6] D. M. Nobre, W. C. Boaventura, and W. L. A. Neves, "Phase-domain network equivalents for electromagnetic transient studies," The 2005 IEEE Power Engineering Society General Meeting, CD-ROM, San Francisco, USA, June 12th-16th, 2005.

[7] A. Budner, "Introduction of frequency dependent transmission line parameters into an electromagnetic transients program," IEEE Transaction on Power Apparatus and Systems, Vol. PAS-89, pp. 88–97, January 1970.

[8] S. Carneiro Jr., J. R. Martí, H. W. Domme1, and H. M. Barros, "An efficient procedure for the implementation of corona models in electromagnetic transients programs," IEEE Transactions on Power Delivery, Vol. 9, No. 2, April 1994.

[9] T. F. R. D. Martins, A. C. S. Lima, and S. Carneiro Jr., "Effect of impedance approximate formulae on frequency dependence realization," The 2005 IEEE Power Engineering Society General Meeting, CD-ROM, San Francisco, USA, June 12th-16th, 2005.

[10] J. R. Marti, "Accurate modelling of frequency-dependent transmission lines in electromagnetic transients simulations," IEEE Transaction on PAS, Vol. 101, pp. 147–155, January 1982.

[11] E. Clarke, "Circuit analysis of AC power systems," Vol. I, Wiley, New York, 1950.

[12] L. M. Wedepohl, "Application of matrix methods to the solution of travelling-wave phenomena in polyphase systems", Proceedings IEE, Vol. 110, pp. 2200–2212, December 1963.

[13] L. M. Wedepohl and D. J. Wilcox, "Transient analysis of underground power-transmission system—system model and wave propagation characteristics," Proceedings of IEE, Vol. 120, No. 2, pp. 253–260, 1973.

[14] L. M. Wedepohl, H. V. Nguyen, and G. D. Irwin, "Frequency dependent transformation matrices for untransposed transmission lines using Newton-Raphson method", IEEE Transaction on Power Systems, Vol. 11, No. 3, pp. 1538–1546, August 1996

J. Electromagnetic Analysis & Applications, 2010, 2: 18-24
doi:10.4236/jemaa.2010.21003 Published Online January 2010 (http://www.SciRP.org/journal/jemaa)

A Probabilistic Analysis on the Harmonic Cancellation Characteristics of the Scott Transformer

Hooman Erfanian MAZIN, Joey GALLANT

Department of Electrical and Computer Engineering, University of Alberta, Edmonton, Canada.
Email: herfania@ece.ualberta.ca, jggallan@ualberta.ca

Received August 14th, 2009; revised September 22nd, 2009; accepted September 28th, 2009.

ABSTRACT

The Scott transformer is widely used in electric railway systems when there are two unbalanced single-phase loads as this transformer can reduce unbalance currents. This paper investigates whether or not the Scott transformer can also reduce harmonic current. Our study shows that it can reduce the harmonic current when single-phase loads have identical harmonic characteristics. This harmonic reduction occurs through the cancellation of harmonic currents of single-phase loads in the transformer windings. Our studies also show that there is some degree of cancelation even when the loads do not have identical harmonic characteristics. The cancellation depends on load balance factor and harmonic order.

Keywords*: *Terms-Harmonics, Harmonic Cancellation, Scott Transformer, Probabilistic, Power Quality

1. Introduction

Supplying electrical traction loads presents some power quality challenges to power system. Electric trains are fed by a single-phase AC catenary line (Figure 1), presenting an unbalanced load to the three-phase power system. In an electric train, the single-phase AC power is rectified into DC power. This leads to the generation of harmonic currents. As a result, an electric railway load is a large unbalanced and harmonic-generating load.

Dividing the catenary line to the in-coming and outgoing sides makes it possible to present each side as a separate single-phase load. The Scott transformer is a widely used transformer that converts the three-phase supply into two single-phase power supplies. Scott transformers have been used in many electric railway systems, (for instance in the Tokaido-Shinkansen electric railway [1]), to reduce the aforementioned unbalance problem. If two loads are equal, the Scott transformer presents them as one balanced three-phase load to the three-phase supply system. This solves the imbalance problem. In reality, however, these two single-phase loads are rarely equal and the transformer still draws unbalanced power from the system. In this case, the degree of unbalance is, at least, reduced in comparison with the case in which loads are directly connected the system. References [2–4] investigated the degree of load unbalance seen from the three-phase system when two single-phase loads have different sizes.

A recent study by the author [5] showed that Scott transformer can also reduce the harmonic current when single-phase loads have identical harmonic characteristics. The results showed that the Scott transformer reduces the injected harmonic currents into the system by cancelling out the harmonic currents generated by single-phase harmonic loads.

Intuitively, this leads to the question of whether the Scott transformer is also able to reduce the generated harmonics by two single-phase loads when loads are not identical. The purpose of this paper is to study the amount of this harmonic cancellation when single-phase loads do not have identical harmonic characteristics.

This paper is organized as follows. Section 2 presents the problem definition and study model. Section 3 inves-

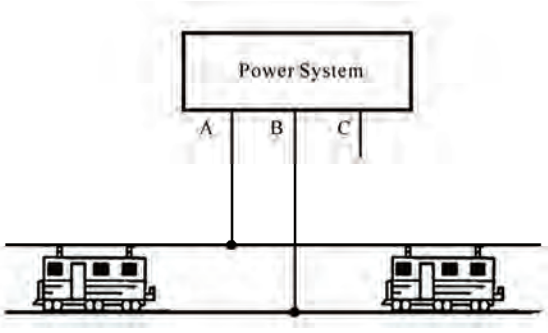

Figure 1. Single-phase AC catenary line supplies the electric train

tigates the harmonic reduction when single-phase loads have the same size. Section 4 presents the results when the single-phase loads do not have the same size, and Section 5 summarizes the findings.

2. Problem Description and Study Model

The model under investigation is illustrated by (Figure 2) and can be described as follows: Two single-phase non-linear loads are supplied using a Scott transformer. The non-linear loads inject harmonic currents into the secondary side of the transformer. The aim is to find out the amount of these injected harmonic currents observed form the primary side of the transformer. These values are compared with the injected harmonic currents when two single-phase loads are directly connected to the utility side. In the direct connection case, the two non-linear loads are connected between phase *A* and *B* of the utility side.

Our study investigates the impact of Scott transformers on the reduction of harmonic currents observed from the utility side. To study this characteristic, we need to develop a study model for the non-linear loads, Scott transformer and power system. In our study, the power system is simply modeled by ideal sinusoidal voltage sources. Also, for this work, the power system impedance and voltage background harmonics in the power system are neglected.

2.1 Traction Load Model

The harmonic current source model is the most commonly used model to represent power-electronic based loads [4]. In this paper, this model is utilized to model traction loads. A traction load is modeled by a harmonic current source in each harmonic order (Figure 2). Since this paper is investigating the harmonic cancellation effects of Scott transformers, not the performance of the traction load, this model is sufficient. In this study, accurate inclusion of the phase angle information (θ_{ha} and θ_{hb}) is essential to estimate harmonic cancellation effects. To study the cases where single-phase loads have identical harmonic characteristics, these phase angles are calculated as shown in Equations (1) and (2). For the Scott transformer case,

$$\theta_{hb} = \frac{\pi}{2}h + \theta_{ha} \quad (1)$$

where h is the harmonic order. For direct connection case,

$$\theta_{hb} = \theta_{ha} \quad (2).$$

In both cases, θ_{ha} is assumed as the reference angle and set to zero. To study cases where single-phase loads do not have identical harmonic characteristics, a random variable with uniform distribution is added to the phase angles [6]. Phase angles are then calculated as shown in Equations (3) and (4). For the Scott transformer case,

$$\theta_{hb} = \frac{\pi}{2}h + \theta_{ha} + \theta_{rand} \quad (3)$$

For the direct connection case,

$$\theta_{hb} = \theta_{ha} + \theta_{rand} \quad (4)$$

where θ_{rand} is a random variable.

2.2 Transformer Modeling

A diagram illustrating the connection of windings for the Scott transformer is shown in Figure 3. A Scott transformer consists of one two-winding transformer (T_1) and one three-winding transformer (T_2). Neglecting the magnetization current, we get the following equation from the MMF Equations

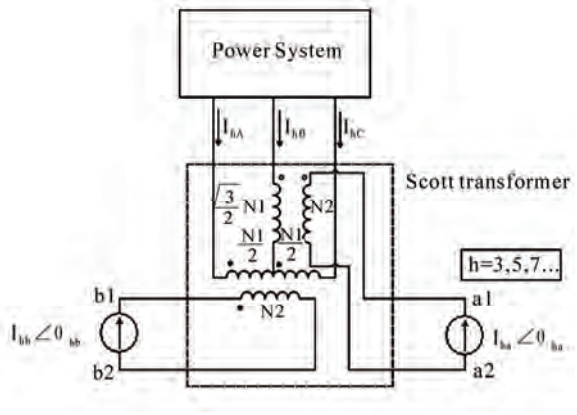

Figure 2. Supplying two single-phase harmonic-generating loads by Scott transformer

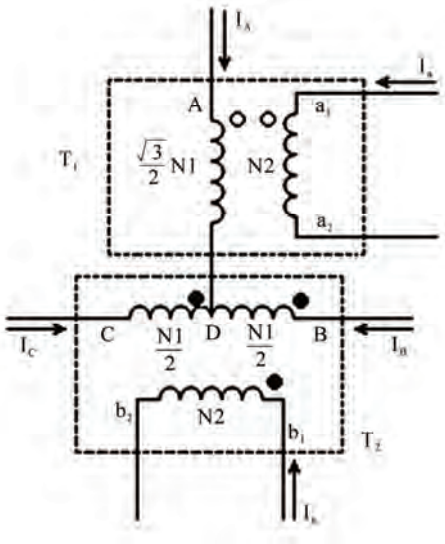

Figure 3. A diagram showing the connection of windings for the Scott transformer

$$\begin{cases} \frac{\sqrt{3}}{2} N_1 I_A + N_2 I_a = 0 \\ \frac{1}{2} N_1 I_B - \frac{1}{2} N_1 I_C + N_2 I_b = 0 \end{cases} \quad (5)$$

From Kirchhoff's current law, we know that,

$$I_A + I_B + I_C = 0 \quad (6)$$

Finally using Equations (5) and (6), the following equation is derived that relates the secondary-side currents to the primary-side currents.

$$\begin{bmatrix} I_A \\ I_B \\ I_C \end{bmatrix} = \frac{N_2}{N_1} \begin{bmatrix} -2/\sqrt{3} & 0 \\ 1/\sqrt{3} & -1 \\ 1/\sqrt{3} & 1 \end{bmatrix} \begin{bmatrix} I_a \\ I_b \end{bmatrix} \quad (7)$$

Similarly for the direct connection of the load to the system (See Figure 4), we get

$$\begin{bmatrix} I_A \\ I_B \\ I_C \end{bmatrix} = \frac{N_2}{N_1} \begin{bmatrix} -1 & -1 \\ 1 & 1 \\ 0 & 0 \end{bmatrix} \begin{bmatrix} I_a \\ I_b \end{bmatrix} \quad (8)$$

In our study, we set $N_1 = N_2$

3. Study Case 1: Equal Single-Phase Loads

In this case, both I_{ha} and I_{hb} have the same magnitude. Two scenarios are studied; 1) when single-phase loads have identical harmonic characteristics, and 2) when single-phase loads do not have identical harmonic characteristics.

3.1 Identical Harmonic Characteristic

When two single-phase loads are identical, the Scott transformer presents these loads as a balanced three-phase load to the power system. In this study case, we investigate the impact of the Scott transformer on the harmonic current measured in the power system. For each harmonic order, we set $|I_{ha}|=|I_{hb}|=0.5pu$. The harmonic currents observed in the primary side are calculated using Equations (5) and (6) and are shown in Table 1.

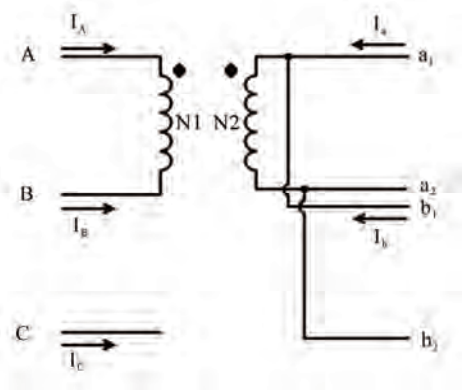

Figure 4. Connection diagram of windings for the direct connection case

When loads are directly connected to the power system, there is no current in phase *C* and the harmonic current is uniformly distributed between Phase *A* and *B*. The Scott transformer distributes generated harmonics among three phases resulting in less harmonic currents in each phase. In this regard, the maximum magnitude current through the Scott transformer is reduced by 42.4% in comparison to the direct connection case.

Another analysis to be performed is the symmetrical component analysis of the results. Although the magnitude of harmonic currents in each phases with the Scott transformer connection are equal, triple-order harmonics are not necessarily zero sequence. Similarly, non-triple-order harmonics are not necessarily negative and positive sequences.

The analysis of the symmetrical components of harmonic currents permits the study of harmonic cancellation from another perspective. The three-phase primary-side harmonic currents are decomposed into symmetrical components, I_h^+, I_h^- and I_h^0 as shown in Table 2.

Table 1. The magnitude of harmonic currents (per-unit) in phases measured in the primary side for direct and scott connections

H-order	Direct			Scott		
	I_{hA}	I_{hB}	I_{hC}	I_{hA}	I_{hB}	I_{hC}
3	1	1	0	0.576	0.576	0.576
5	1	1	0	0.576	0.576	0.576
7	1	1	0	0.576	0.576	0.576
9	1	1	0	0.576	0.576	0.576
11	1	1	0	0.576	0.576	0.576
13	1	1	0	0.576	0.576	0.576

Table 2. The symmetrical components of harmonic currents (per-unit) measured from the primary side for direct and Scott connections

H-order	Direct connection			Scott connection		
	I_h^+	I_h^-	I_h^0	I_h^+	I_h^-	I_h^0
3	1	1	0	0	1	0
5	1	1	0	1	0	0
7	1	1	0	0	1	0
9	1	1	0	1	0	0
11	1	1	0	0	1	0
13	1	1	0	1	0	0

Both the direct connection and Scott transformer do not generate zero sequence harmonic current. The results also reveal that the Scott transformer cancels out the positive-sequence component of *(4k-1)* order harmonics completely (i.e. 3, 7, and 11), while it does not affect the negative-sequence component of these harmonic orders at all. The reverse phenomenon happens for the *(4k+1)* order harmonics (i.e. 5, 9, and 13). These results can be verified through Equation (1). For *(4k-1)* order harmonics, we have that, $\theta_{hb} = -\frac{\pi}{2} + \theta_{ha}$, and for *(4k+1)* order harmonics we have that, $\theta_{hb} = \frac{\pi}{2} + \theta_{ha}$.

3.2 Non-Identical Harmonic Characteristic

In this case, we set $|I_{ha}|=|I_{hb}|=0.5pu$. θ_{ha} is assumed to be the reference angle and set to zero. θ_{hb} is calculated by using Equations (3) and (4). Since θ_{hb} is a function of a random variable, I_{hA}, I_{hB}, and I_{hC} are not deterministic. In this regard, the cumulative density function (CDF) of the maximum harmonic current observed from the primary side can be evaluated as follows:

$$F(z) = \int \left(\left[\max\left\{ |I_A|, |I_B|, |I_C| \right\} < z \right] f_\theta(\theta_{rand}) d\theta_{rand}$$

where f_θ is the distribution function of the random variable.

Figure 5 shows CDF of the maximum harmonic current observed at the primary side for odd harmonic orders, when θ_{rand} has uniform distribution over [-10º,10º]. In this case, the amount of harmonic cancellation by the Scott transformer is reduced in comparison to the case where loads are not identical (see Table 1). However, the Scott transformer still has better performance when compared with the direct connection approach. Interestingly, this predominance is not continual, and increasing the range of the random variable (θ_{rand}) decreases this predominance. For example, Figure 6 shows the CDFs when θ_{rand} is uniformly distributed over [-90º,90º]. In the most severe case when the range is [-180º,180º] the cancellation performance is reduced dramatically (see Figure 7).

4. Study Case 2: Unequal Single-Phase Loads

In this study case, we study the harmonic reduction characteristics of the Scott transformer when single-phase loads do not have the same magnitude. To express the load balance of this distribution, we define the load balance factor as follows:

$$\text{Load balance factor} = k = \frac{|I_{ha}|}{|I_{ha}| + |I_{hb}|},$$

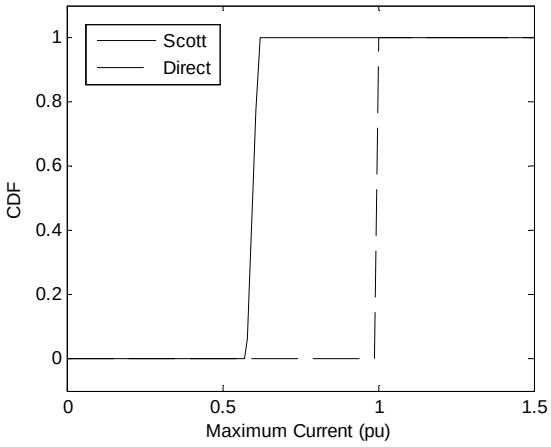

Figure 5. CDFs of maximum harmonic currents where θ_{rand} is uniformly distributed over [-10º,10º]

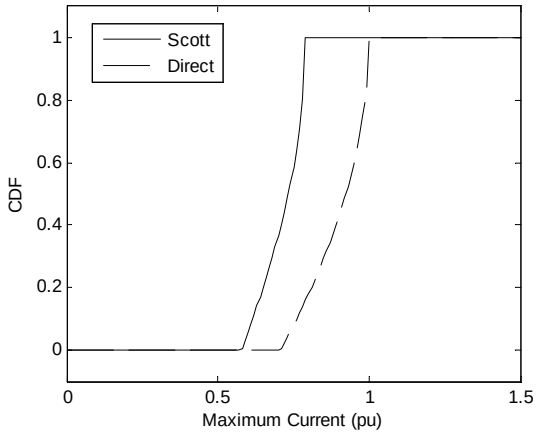

Figure 6. CDFs of maximum harmonic currents where θ_{rand} is uniformly distributed over [-90º,90º]

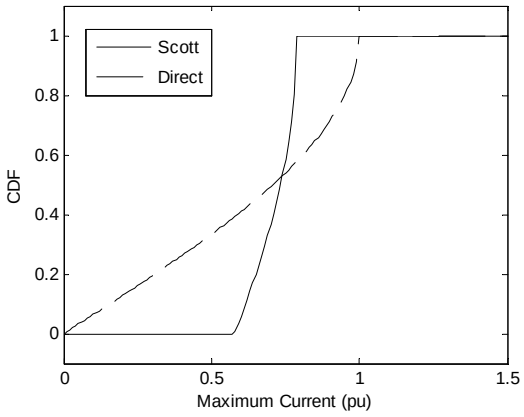

Figure 7. CDFs of maximum harmonic currents where θ_{rand} is uniformly distributed over [-180º,180º]

where k varies from 0 to 1. The summation of $|I_{ha}|$ and $|I_{hb}|$ is to be 1 per-unit, so we have

$$\begin{cases} |I_{ha}| = k \\ |I_{hb}| = 1-k \end{cases}$$

4.1 Identical Harmonic Characteristic

In this case, although loads do not necessarily have the same size, they have the same harmonic characteristics (i.e. identical locomotives). For instance when seven loads (trains) are fed by side *a* and three loads (trains) are fed by side *b*, the load balance factor is 0.7. In direct connection, both side *a* and *b* are supplied from the same place, so the variation of load balance factor does not affect the primary side harmonic currents. Magnitude of the third-order harmonic current in the primary-side of the Scott transformer versus load balance factor is shown in Figure 8.

When load balance equals zero (all loads are fed by side *b*), the magnitude of I_{hA} is zero and the magnitude of I_{hB} and I_{hC} are maximum. Increasing the load balance factor results in increase of harmonic currents in Phase *A* and decrease of harmonic currents in other phases. When load balance factor equals 0.5, the harmonic currents in all phases become equal.

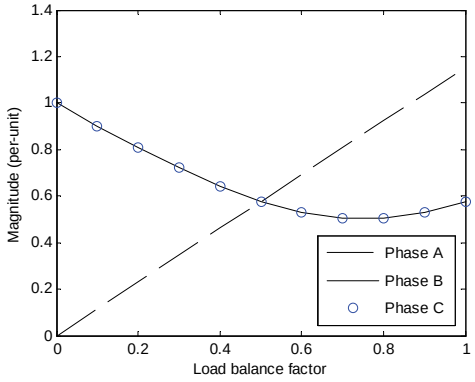

Figure 8. Magnitude of the third order harmonic current seen from the primary-side of the Scott transformer

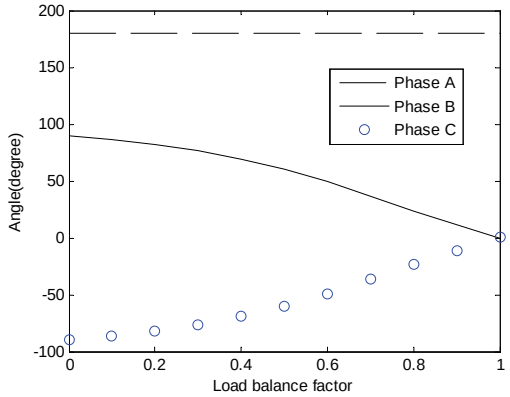

Figure 9. Angle of the third order harmonic current seen from the primary-side of the Scott transformer versus load balance factor

An examination of the effect of harmonic current angle is also relevant to this study. This is apparent when considering the angle of the third order harmonic current measured from the primary-side of the Scott transformer versus load balance factor as shown in Figure 9. Variation of the load balance factor does not affect the phase angle of the harmonic current in phase *A* and it is always 180 degrees. Conversely, the phase angles in phases *B* and *C* are sensitive to the variation of the load balance factor.

4.1.1 Maximum-Magnitude Index

Maximum magnitude among the utility side injected harmonic currents, $|I_{hA}|$, $|I_{hB}|$, and $|I_{hC}|$, is defined as the maximum-magnitude index. Our study shows that maximum-magnitude indices of the Scott transformer obey the same pattern for all of the studied harmonic orders (odd harmonic orders). The maximum-magnitude index for the Scott and direct connections versus load balance factor are shown in Figure 10.

While the direct connection's maximum-magnitude index does not depend on the load balance factor, the Scott transformer connection's index does. For load balance factors less than 0.82, the Scott transformer cancels out the injected harmonic currents resulting in less harmonic currents in the primary side. The maximum cancellation occurs when $|I_{ha}|$ and $|I_{hb}|$ are equal, yielding a reduction of 42.3%. For highly unbalanced single-phase loads (when the load balance factor is greater than 0.82) the Scott transformer amplifies the injected harmonic. The maximum amplification (roughly 15%) occurs when $|I_{ha}|$ is supplying the entire load.

4.1.2 Symmetrical Components of the Harmonic

In this part, the impact of the Scott transformer on the reduction of symmetrical components of harmonic currents is investigated. The Scott transformer cancels the negative sequence of the *(4k+1)* order harmonics depending on the load balance factor as seen in Figure 11. Maximum cancellation occurs when the load balance factor is equal to 0.5. The Scott transformer does not affect the negative sequence of these harmonic orders. The reverse situation happens for the *(4k-1)* harmonic orders as shown in Figure 12.

4.2 Non-Identical Harmonic Characteristic

The harmonic cancellation performance of the Scott transformer when loads are not identical is studied in this section. In this case, a similar study to that which was performed in Subsection 3.2 can also be performed for each load balance factor. Figure 13 shows the contour plot for CDF of the maximum harmonic current observed at the primary side of the Scott transformer versus each load balance factor when θ_{rand} is a random variable uniformly

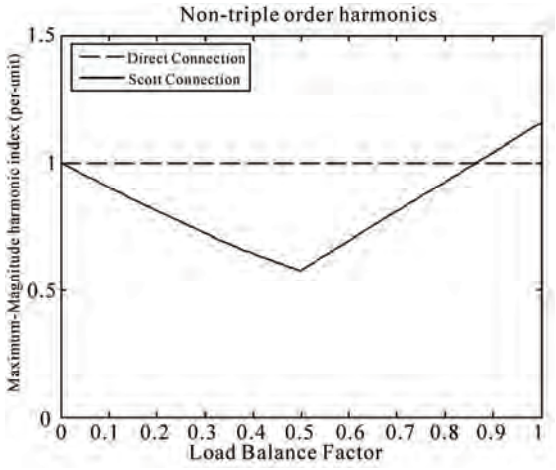

Figure 10. The maximum-magnitude harmonic index for the Scott and Direct connections versus load balance factor

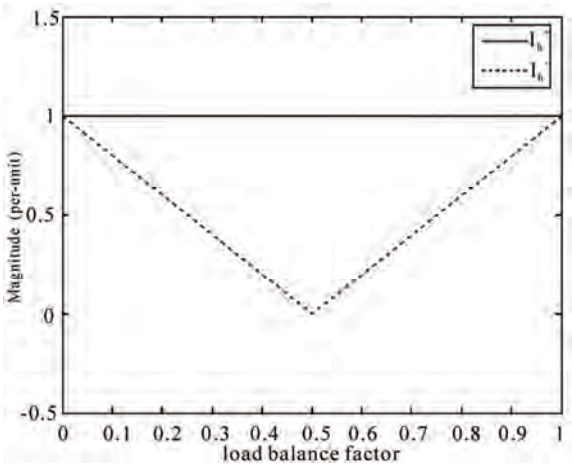

Figure 11. The symmetrical components of the *(4k+1)* order harmonic currents as seen from the primary side of the Scott transformer

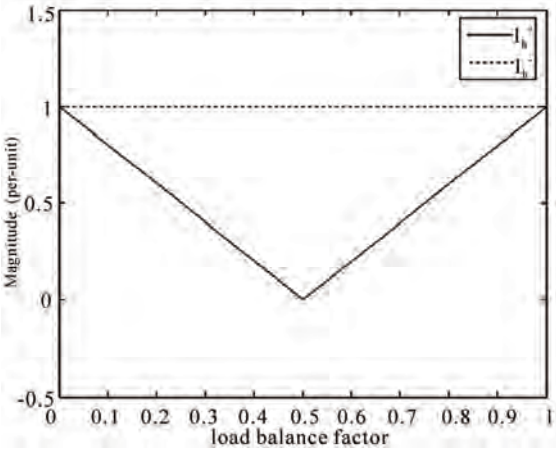

Figure 12. The symmetrical components of the *(4k-1)* order harmonic currents as seen from the primary side of the Scott transformer

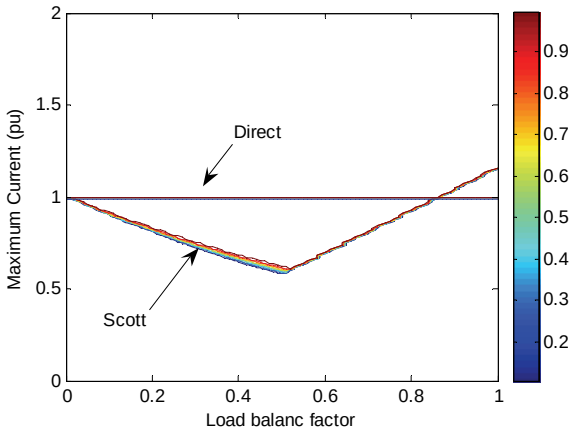

Figure 13. Contour plot for CDF of the maximum harmonic current for Scott transformer where θ_{rand} is uniformly distributed over [-10°,10°]

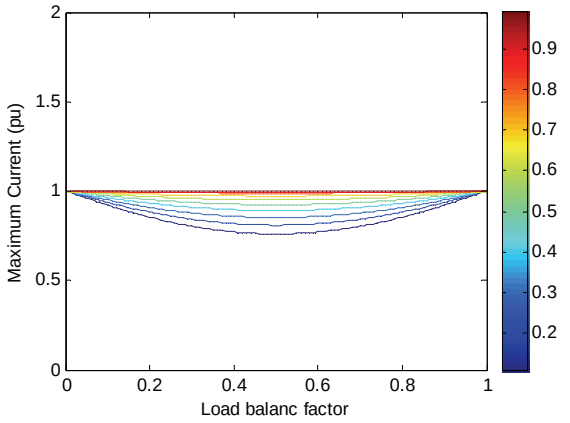

Figure 14. Contour plot for CDF of the maximum harmonic current for direct connection where θ_{rand} is uniformly distributed over [-90°,90°]

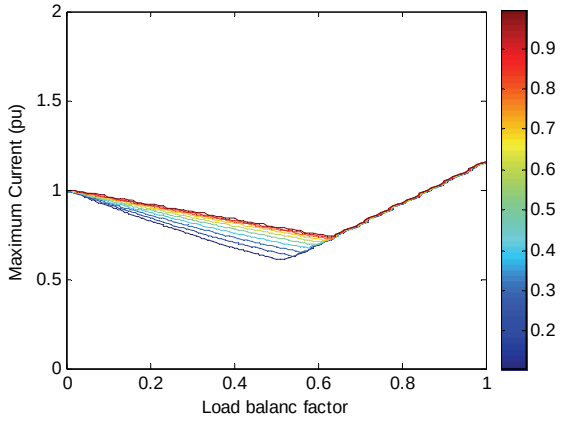

Figure 15. Contour plot for CDF of the maximum harmonic current for Scott transformer where θ_{rand} is uniformly distributed over [-90°,90°]

distributed over [-10º,10º]. Compared with Figure 6, the harmonic cancellation performance is very similar to the case where the load has identical harmonic characteristics. It should be noted however, that changing the range of variation of θ_{rand} causes more change in this performance. Figure 15 shows the contour plot for CDF of the maximum harmonic current for the Scott transformer when θ_{rand} is [-90º,90º]. Observing the contour plot for the direct connection case (Figure 14), one can see that the predominance of the Scott transformer in harmonic cancellation is highly reduced in this range.

5. Conclusions

The paper has investigated the harmonic cancellation characteristics of the Scott transformer. The main findings are summarized as follows:

1) When single-phase loads have identical harmonic characteristics the Scott transformer reduces the maximum harmonic current observed at the primary side for load balance factors less than 0.82.

2) The Scott transformer completely cancels out the positive sequence components of the *(4k-1)* harmonic orders. The same happens to the negative sequence components of the *(4k+1)* harmonic orders.

3) When single-phase loads do not have identical harmonic characteristics, there is still some degree of cancellation. The level of cancellation varies from 42.3% to 0% depending on the degree of harmonic characteristics difference.

REFERENCES

[1] Y. Mochinaga, Y. Akatsuka, K. Arai, and M. Ono, " Development of three-winding transformer for shinkansen auto-transformer feeding system receiving extra high voltage," The Institute of Electrical Engineers of Japan, Vol. 111-d, No. 3, pp. 237–244, 1991.

[2] B. K. Chen and B. S. Guo, "Three phase models of specially connected transformers," IEEE Transactions on Power Delivery, Vol. 11, No. 1, pp 323–330, January 1996.

[3] T. H. Chen and H. Y. Kuo, "Network modeling of traction substation transformers for studying unbalance effects," IEE Proceedings Generation, Transmission and Distribution, Vol. 142, No. 2, pp. 103–108, March 1995.

[4] S. Chen, R. Li, and P. His, "Traction system unbalance problem - Analysis methodologies," IEEE Transactions on Power Delivery, Vol. 19, No. 4, pp. 1877–1883, October 2004.

[5] H. Erfanian and W. Xu, "An investigation on the effectiveness of Scott transformer on harmonic reduction, power and energy society general meeting - Conversion and delivery of electrical energy in the 21st century," 2008 IEEE, pp. 1–4, 20–24, July 2008.

[6] A. Cavallini and G. C. Montanari, "A deterministic/ stochastic framework for power system harmonics modeling," IEEE Transactions on Power Systems, Vol. 12, No. 1, pp. 407–415, February 1997.

J. Electromagnetic Analysis & Applications, 2010, 2: 25-30
doi:10.4236/jemaa.2010.21004 Published Online January 2010 (http://www.SciRP.org/journal/jemaa)

Research on Torque-Angle Characteristic of Large Gap Magnetic Drive System

Yan XU, Jianping TAN, Yunlong LIU, Zhongyan ZHU

College of Mechanical and Electrical Engineering, Central South University, Changsha, China.
Email: x_y616@163.com

Received August 18th, 2009; revised September 20th, 2009; accepted September 28th, 2009.

ABSTRACT

The principle and design method of the large gap magnetic drive system is studied in this work. The calculation model of the torque-angle characteristic in the large gap magnetic drive system driven by traveling wave magnetic field is established. The calculation model is computed by using MATLAB software, and the pattern of the system's torque-angle characteristic is obtained by analyzing study results. These results indicate that: torque-angle characteristic and the driving torque of the system can be adjusted by changing the electric current of coil, the magnetization of permanent magnetic gear, the inner diameter of permanent magnetic gear, the coupling distance between electromagnet and permanent magnetic gear, the outer diameter of permanent magnetic gear, and the axial length of permanent magnetic gear.

***Keywords*: *Magnetic Drive, Large Gap, Torque-Angle Characteristic, Permanent Magnetic Gear* (*Permanent Magnet*)**

1. Introduction

Magnetic drive technology is used to realize a non-contact transmission of forces and moments by using magnetic force produced by permanent magnetic material or electro-magnetic mechanism. It has become a study hotspot in the field of mechanical drive [1].

Pan Zheng and Yousef Haik [2] presented two models of a magnetically driven screw pumps that were developed for blood pump designing. The magnetic characteristics for the coupling force and torque were investigated. The power was transmitted to the pump from an outside motor through magnetic coupling without physical connection.

Karel F [3] used the rotary field to drive fluid in the square vessel, and established the magnetic force computation model of system.

ZHAO Han [4] established and simulated the physics mathematical model and the dynamic property model of the rare earth permanent magnetic gear drive system. The torque calculation formula of system was derived.

Michael Schreiner [5] made a permanent magnet be levitated. A mathematical model for the described effect was presented.

On the characteristic of the non-bearing magnetic resistance motor, MASATSUGU TAKEMOTO [6] established the torque computation equation of the rotor.

Kwang Suk Jung and Yoon Su Baek [7] made a mover be levitated by magnetic force between iron-core electromagnets attached under the upper-side of a stator and ferromagnetic plates belonging to the mover.

Nowadays, in the application of magnetic drive technology, the gap between the system magnetic poles is small. But when the gap between active and passive magnetic pole increases, the driving force cannot ensure the system reliability. Currently, literatures about application of magnetic drive technology on the axial flow type blood pump driving are few. In order to enhance the reliability of magnetic drive system with a large gap, a certain magnetic drive system driven by traveling wave magnetic field whose air gap reaches 60mm is studied [8]. In this paper, the torque-angle characteristic of the system is studied, and a theoretical basis for the design of the large gap magnetic drive system can be deduced from the study result.

2. Structure of the Large Gap Magnetic Drive System

2.1 Principle of the Passive Permanent Magnet's Rotation

The principle of rotation of the passive permanent magnet is shown in Figure 1. Working state of the system depends on the magnetic force which is produced by

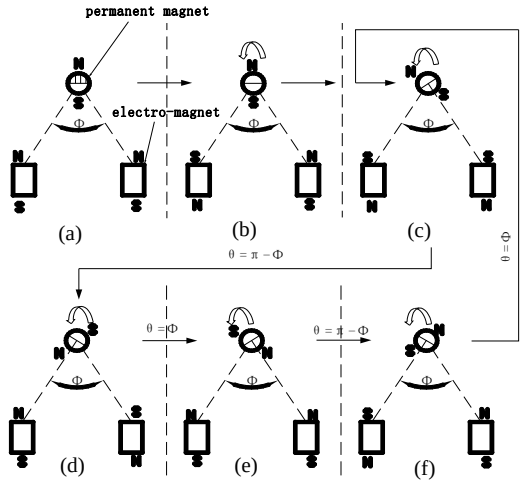

Figure 1. Principle of rotation of the passive permanent magnet

permanent magnet and the electromagnet. In Figure 1(a), the electromagnet produces N pole on both sides of the permanent magnet called the state NN. It also adjusts the top pole of the permanent magnet to N, the bottom pole to S. In Figure 1(b), the electromagnet produces the state SN and makes the permanent magnet to rotate anti-clockwise. In Figure 1(c) to Figure 1(f), when the permanent magnet rotates for one cycle, the electromagnet completes the state variation of SS→NS→NN→SN. We can adjust the permanent magnet's speed by modifying the electromagnet's magnetic poles state switching frequency; furthermore by modifying the timing of the electromagnet's magnetic poles state switching we can obtain a clockwise rotation of the permanent magnet.

Therefore, the designing of a large gap magnetic drive system can be realized according to the transmission principle mentioned above.

2.2 Design of the Large Gap Magnetic Drive System

As shown in Figure 2, the iron core is circled by 4 groups of coils. These coils output pulse through the MCU as shown in Figure 3. P1.0 causes coil #1 to produce N pole on the left side of the permanent magnet, P1.1 causes coil #2 to produce S pole on the left side of the permanent magnet, P1.2 causes coil #3 to produce S pole on the right side of the permanent magnet, and P1.3 causes coil #4 to produce N pole on the right side of the permanent magnet. So all kinds of electromagnet magnetic poles state as shown in Figure 1 can be realized and the permanent magnet can be driven by the control software.

The large gap magnetic drive system can be used to drive axial flow type blood pump. The pump is composed of bearings, impeller and permanent magnet, as shown in Figure 4 and Figure 5.

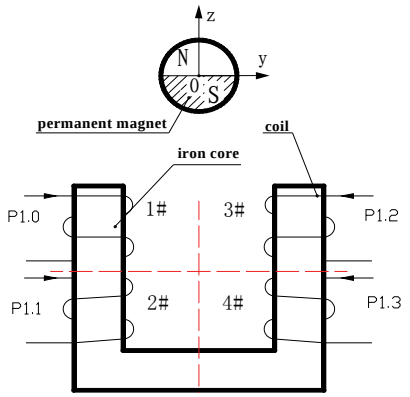

Figure 2. Structure of the large gap magnetic drive system

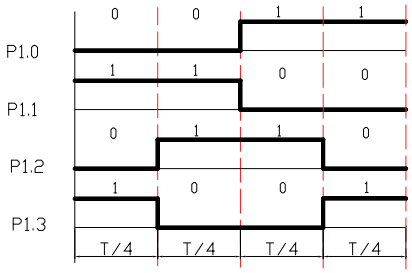

Figure 3. Output pulse succession of electromagnet's coils

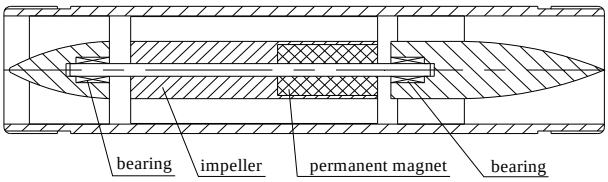

Figure 4. Schematic of an axial flow type blood pump

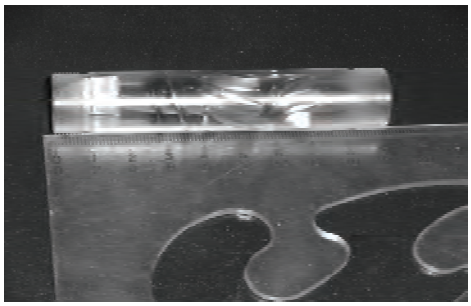

Figure 5. Prototype of an axial flow type blood pump

3. Establishment of Torque-Angle Characteristic's Calculation Model of the System

3.1 Research Foundation

The mathematical model of the system's spatial magnetic field can be obtained from [9]:

$$\begin{cases} B_x = \dfrac{3u}{4\pi} \cdot \dfrac{N \cdot I \cdot S \cdot x \cdot z}{(\sqrt{R^2 + x^2 + y^2 + z^2})^5} & (1) \\ B_y = \dfrac{3u}{4\pi} \cdot \dfrac{N \cdot I \cdot S \cdot y \cdot z}{(\sqrt{R^2 + x^2 + y^2 + z^2})^5} & (2) \\ B_z = \dfrac{u}{2\pi} \cdot \dfrac{N \cdot I \cdot S}{(\sqrt{R^2 + x^2 + y^2 + z^2})^3} \cdot (1 - \dfrac{3}{2} \cdot \dfrac{x^2 + y^2}{R^2 + x^2 + y^2 + z^2}) & (3) \end{cases}$$

In Formulas (1)-(3), B_x, B_y, B_z are the spatial magnetic field component in the x, y and z directions respectively. The coordinate system is shown in Figure 2. N is the number of windings of coil, R is the radius of coil. I is the electric current of coil, S is the area of coil, and u is the magnetic conductivity in the 4 electromagnet magnetic poles states (NS, SS, SN and NN).

The mathematical model of the system's driving torque can be obtained from [10]:

$$\therefore T = \frac{2}{\cos\theta} \cdot \int_{-\frac{l}{2}}^{\frac{l}{2}} dx \int_{r_2 \cos\theta}^{r_1 \cos\theta} (y \cdot M \cdot B_y + y \cdot M \cdot B_z \tan\theta) dy \quad (4)$$

In Formula (4), r_1, r_2, l, θ and $\boldsymbol{M}$ are the outer radius, the inner radius, the axial length, the corner, the magnetization of the permanent magnet respectively. Establishment of torque-angle characteristic's calculation model of the system for example, the system's electromagnet is Electromagnet C57 (In the coordinate system of Figure 2, the electromagnet is named by the iron core-size in the y direction. If the size along the y direction is 57mm, it is called Electromagnet C57). The distance in the z direction between electromagnet and the permanent magnet is 60mm.

According to Formula (4) and the principle of the passive permanent magnet's rotation shown in Figure 3, the rotation process of the permanent magnet in one cycle can be divided into 4 stages. So the Formula (4) can be decomposed into 4 piecewise functions:

In the vicinity of the state NS of the system's electromagnet magnetic poles, the permanent magnet's corner range is $\theta \in (0° - 18°) \cup (342° - 360°)$. In the vicinity of the state SS of the system's electromagnet magnetic poles, the permanent magnet's corner range is $\theta \in (18° - 162°)$. In the vicinity of the state SN of the system's electromagnet magnetic poles, the permanent magnet's corner range is $\theta \in (162° - 198°)$. In the vicinity of the state NN of the system's electromagnet magnetic poles, the permanent magnet's corner range is $\theta \in (198° - 342°)$.

So the calculation model of the system's torque-angle characteristic can be established as follows:

$$\begin{cases} T_1 = \dfrac{2}{\cos\theta} \times \int_{-\frac{l}{2}}^{\frac{l}{2}} dx \int_{r_2 \cos\vartheta}^{r_1 \cos\theta} (y \bullet M \bullet B_{y1} + y \bullet M \bullet B_{z1} \tan\theta) dy, \\ \theta \in (0° - 18°) \cup (342° - 360°) & (5) \\ T_2 = \dfrac{2}{\cos\theta} \times \int_{-\frac{l}{2}}^{\frac{l}{2}} dx \int_{r_2 \cos\vartheta}^{r_1 \cos\theta} (y \bullet M \bullet B_{y2} + y \bullet M \bullet B_{z2} \tan\theta) dy, \\ \theta \in (18° - 162°) & (6) \\ T_3 = \dfrac{2}{\cos\theta} \times \int_{-\frac{l}{2}}^{\frac{l}{2}} dx \int_{r_2 \cos\vartheta}^{r_1 \cos\theta} (y \bullet M \bullet B_{y3} + y \bullet M \bullet B_{z3} \tan\theta) dy, \\ \theta \in (162° - 198°) & (7) \\ T_4 = \dfrac{2}{\cos\theta} \times \int_{-\frac{l}{2}}^{\frac{l}{2}} dx \int_{r_2 \cos\vartheta}^{r_1 \cos\theta} (y \bullet M \bullet B_{y4} + y \bullet M \bullet B_{z4} \tan\theta) dy, \\ \theta \in (198° - 342°) & (8) \end{cases}$$

In Formulas (5)-(8), T_1 is the system's driving torque when electromagnet's magnetic poles are in the state NS. T_2 is the system's driving torque when electromagnet's magnetic poles are in the state SS. T_3 is the system's driving torque when electromagnet's magnetic poles are in the state SN. T_4 is the system's driving torque when electromagnet's magnetic poles are in the state NN. B_{y1}, B_{z1} are the magnet field component in the y and z directions respectively when the electromagnet's magnetic poles are in the state NS and can be obtained by Formulas (2) and (3). B_{y2}, B_{z2} are the magnet field component in the y and z directions respectively when the electromagnet's magnetic poles are in the state SS and can be obtained by Formulas (2) and (3). B_{y3}, B_{z3} are the magnet field component in the y and z directions respectively when the electromagnet's magnetic poles are in the state SN and can be obtained by Formulas (2) and (3). B_{y4}, B_{z4} are the magnet field component in the y and z directions respectively when the electromagnet's magnetic poles are in the state NN and can be obtained by Formulas (2) and (3).

4. Computation of Torque-Angle Characteristic's Calculation Model of the System

In view of the Formulas (5)-(8), the system's driving torque under each kind of permanent magnet's corner can be obtained using MATLAB software. So the calculation model of the system's torque-angle characteristic was computed.

4.1 Basic Parameter Conditions of the System

Electromagnet C57; the number of windings of 4 coils is 400; the electric current of the coil is 1A; the outer diameter of the permanent magnet is 12mm; the inner diameter of the permanent magnet is 2mm; the magnetization of the permanent magnet is 900KA/m; the area of the coil is 33mm^2; the axial length of the permanent magnet is 15mm; the distance in the z direction between the electromagnet and the permanent magnet is 60mm.

4.2 The Result of Computation

In Figures 6-11, the x-axis is the permanents corner (radian). The y-axis is the system's driving torque (Nmm).

1) The electric current of the coil is changed to 0.9A, 1.2A, and 1.7A respectively. Other parameters of the basic conditions keep constant. The influence of the coil's electric current on the system's torque-angle characteristic is studied and shown in Figure 6.

2) The distance along the z direction between electromagnet and the permanent magnet is changed to 40mm, 50mm, 60mm and 65mm respectively. Other parameters of the basic conditions keep constant. The influence of the couple distance on the system's torque-angle characteristic is studied and shown in Figure 7.

3) The magnetization of the permanent magnet is changed to 800 KA/m, 900 KA/m and 955 KA/m respectively. Other parameters of the basic conditions keep constant. The influence of the permanent magnet's magnetization on the system's torque-angle characteristic is studied and shown in Figure 8.

4) The inner diameter of the permanent magnet is changed to 2mm and 3mm respectively. Other parameters of the basic conditions keep constant. The influence of the inner diameter of the permanent magnet on the system's torque-angle characteristic is studied and shown in Figure 9.

5) The outer diameter of the permanent magnet is changed to 12mm, 15mm and 8.2mm respectively. Other parameters of the basic conditions keep constant. The influence of the outer diameter of the permanent magnet on the system's torque-angle characteristic is studied and shown in Figure 10.

6) The axial length of the permanent magnet is changed to 15mm, 25mm and 20mm respectively. Other parameters of the basic conditions keep constant. The influence of the axial length of the permanent magnet on

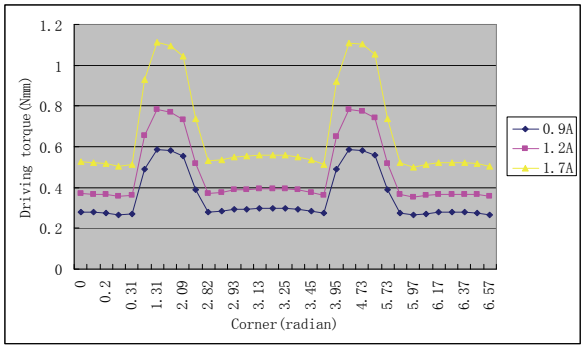

Figure 6. The influence of the coil's electric current on the system's torque-angle characteristic

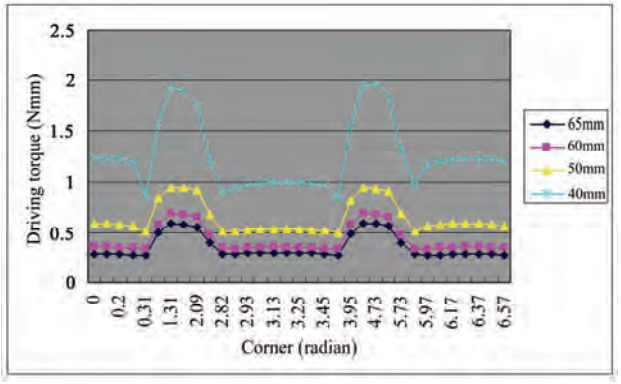

Figure 7. The influence of the couple distance on the system's torque-angle characteristic

the system's torque-angle characteristic is studied and shown in Figure 11.

4.3 Analysis

1) In the permanent magnet's rotation cycle, the magnetic poles state of the electromagnet pass through NS→SS→SN→NN, so the system's torque-angle characteristic is periodic. When the permanent magnet's corner is located in $\theta \in (0° - 18°) \cup (342° - 360°)$, the corresponding magnetic poles of the electromagnet are in the state NS. When the permanent magnet's corner is located in $\theta \in (18° - 162°)$, the corresponding magnetic poles of the electromagnet are in the state SS. When the permanent magnet's corner is located in $\theta \in (162° - 198°)$, the corresponding magnetic poles of the electromagnet are in the state SN. When the permanent magnet's corner is located in $\theta \in (198° - 342°)$, the corresponding magnetic poles of the electromagnet are in the state NN.

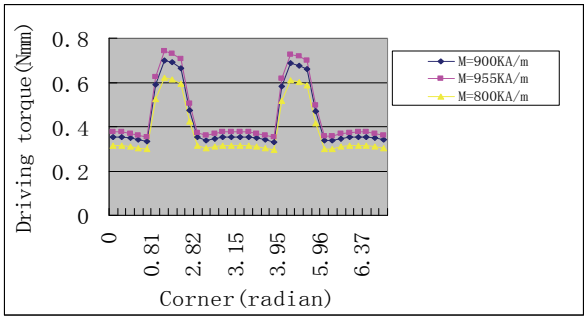

Figure 8. The influence of the permanent magnet's magnetization on the system's torque-angle characteristic

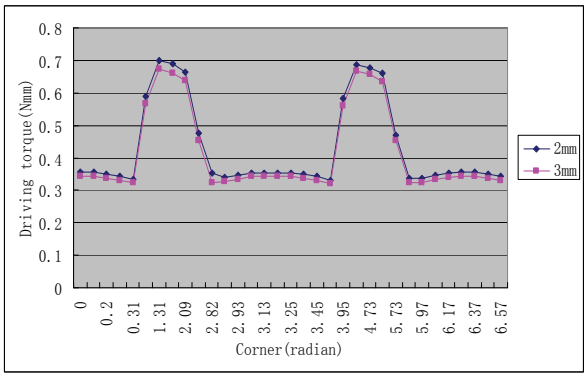

Figure 9. The influence of the inner diameter of the permanent magnet on the system's torque-angle characteristic

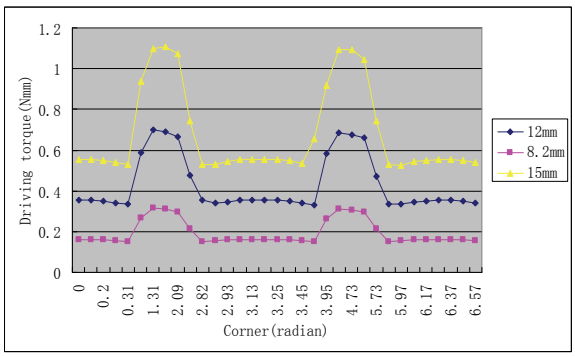

Figure 10. The influence of the outer diameter of the permanent magnet on the system's torque-angle characteristic

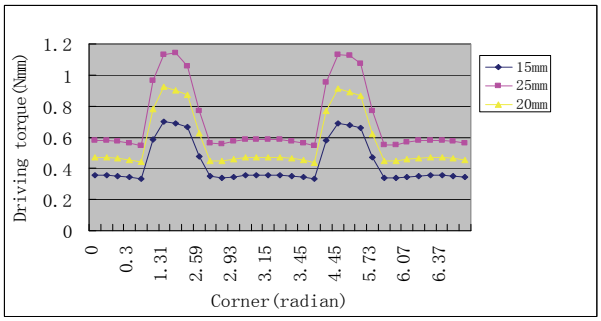

Figure 11. The influence of the axial length of the permanent magnet on the system's torque-angle characteristic

2) In the vicinity of the 4 states of the electromagnet, because of the interaction between the permanent magnet and the electromagnet, the system's driving torque present a maximum value. This maximum value's position is determined by the relative spatial position between the permanent magnet and the electromagnet's coil.

In the vicinity of the state NS, the system's driving torque is symmetric about $\theta = 0°(360°)$. It decreases in the interval $\theta \in (0° - 18°)$ and increases in the interval $\theta \in (342° - 360°)$. The maximum value of the system's driving torque appears about $\theta = 0°(360°)$ because the size and direction of the driving torque, which is acted on the permanent magnet by the electromagnet's 2 magnetic poles, are the same.

In the vicinity of the state SS, the system's driving torque is symmetric about $\theta = 90°$. It decreases in the interval $\theta \in (18° - 90°)$ and increases in the interval $\theta \in (90° - 162°)$. The maximum value of the system's driving torque appears about $\theta = 90°$ because the size and direction of the driving torque, which is acted on the permanent magnet by the electromagnet's 2 magnetic poles, are the same.

In the vicinity of the state SN, the system's driving torque is symmetric about $\theta = 180°$. It decreases in the interval $\theta \in (162° - 180°)$ and increases in the interval $\theta \in (180° - 198°)$. The maximum value of the system's driving torque appears about $\theta = 180°$ because the size and direction of the driving torque, which is acted on the permanent magnet by the electromagnet's 2 magnetic poles, are the same.

In the vicinity of the state NN, the system's driving

torque is symmetric about $\theta = 270°$. It decreases in the interval $\theta \in (198° - 270°)$ and increases in the interval $\theta \in (270° - 342°)$. The maximum value of the system's driving torque appears about $\theta = 270°$ because the size and direction of the driving torque, which is acted on the permanent magnet by the electromagnet's 2 magnetic poles, are the same.

3) The magnetic pole state NN of the electromagnet is produced by coils #1 and #4, and SS is produced by #2 and #3 coil. In states NN and SS, the spatial magnetic field's intensity is the same, directions are opposite, and the system's driving torque is equal.

4) The magnetic pole state NS of the electromagnet is produced by coils #1 and #3, and SN is produced by coils #2 and #4. In states NS and SN, the spatial magnetic field's directions are opposite. Because the distance from coils #2 and #4 to permanent magnet is bigger than the distance from coils #1 and #3 to permanent magnet, the spatial magnetic field's intensity and the system's driving torque are greater in the state NS than in the state SN.

5) Because the magnetic pole's distance between the permanent magnet and the electromagnet are bigger in states NS and SN than in states SS and NN, the spatial magnetic field's intensity and the system's driving torque are lower in states NS and SN than in states SS and NN.

6) The system's driving torque can be improved by increasing the electric current of the coil and the magnetization of permanent magnetic gear, decreasing the inner diameter of permanent magnetic gear and the coupling distance between the system's magnet poles, and increasing the outer diameter of permanent magnetic gear and the axial length of permanent magnetic gear.

5. Conclusions

Through this paper, principle of the passive permanent magnet's rotation is analyzed, and the design method of the large gap magnetic drive system is ascertained. Based on the spatial magnetic field and the driving torque's mathematical model in the large gap magnetic drive system, the calculation model of the system's torque-angle characteristic is established.

Using MATLAB software, the calculation model of the system's torque-angle characteristic is computed and by analyzing the study results, the change pattern of the system's torque-angle characteristic is obtained.

By this, we can know that the system's driving torque can be adjusted by changing the electric current of the coil, the magnetization of permanent magnetic gear, the inner diameter of permanent magnetic gear, the coupling distance between system magnet pole, the outer diameter of permanent magnetic gear, and the axial length of permanent magnetic gear.

These study results provide a theoretical basis for designing the large gap magnetic drive system with stronger driving ability.

6. Acknowledgment

This work is supported by National High Technology Research and Development Program of China (No. 2006AA02Z4E8); the National Natural Science Foundation of China (No.50775223; No.50875266); the Research Fund for the Doctoral Program of Higher Education of China (No.20070533125); as well as the Research Fund of Changsha University (No.CDJJ-09010208).

REFERENCES

[1] X. D. Xu, Z. L. Gong, J. P. Tan, "Blood pump driven system based on extracorporeal magnetic filed couple," Journal of Central South University (Science and Technology), Vol. 38, No. 8, pp. 711–714, 2007.

[2] P. Zheng and Y. Haik. "Force and torque characteristics for magnetically driven blood pump," Journal of Magnetism and Magnetic Materials, Vol. 241, pp. 292–302, 2002.

[3] F. Karel, "A numerical study of flows driven by a rotating magnetic field in a square container," European Journal of Mechanics B/Fluids, No. 10, pp. 1–10, 2007.

[4] H. Zhao, Y. Wang, J. TIan, "Review of study on magnet machine and mechanism," Chinese Journal of Mechanical Engineering, Vol. 39, No. 12, pp. 311–36, 2003.

[5] M. Schreiner, "The driving torque of a rotating levitated cylindrical permanent magnet above a superconductor," Applied Mathematical Modelling, Vol. 31, No. 2, pp. 854–865, 2007.

[6] M. Takemoto, A. Chiba, H. Akagi, and T. Fukao, "Torque and suspension force in a bearingless switched reluctance motor," Electrical Engineering, No. 2, pp. 72–82, 2006.

[7] K. S. Jung and Y. S. Baek, "Precision stage using a non-contact planar actuator based on magnetic suspension technology," Mechatronics, Vol. 13, No. 4, pp. 981–999, 2003.

[8] J. P. Tan, Y. Xu, T. X. Li, and Y. L. Liu, "The scheme design and application of large gap magnetic drive system which is driven by traveling wave magnetic field," IEEE International Conference on Measuring Technology and Mechatronics Automation (ICMTMA'09), Zhangjiajie, China, April 2009.

[9] L. P. Ren, J. S. Zhao "The distribution pattern of magnetic dipole's spatial magnetic field," Hydrographic Surveying and Charting, Vol. 22, No. 2, pp. 18–21, 2002.

[10] Y. Xu and J. P. Tan, "Calculation method of driving torque of the large gap magnetic drives system," Journal of Hunan University (Natural Sciences), Vol. 36, No. 7, pp. 30–35, 2005.

J. Electromagnetic Analysis & Applications, 2010, 2: 31-38
doi:10.4236/jemaa.2010.21005 Published Online January 2010 (http://www.SciRP.org/journal/jemaa)

Extracting Power Transformer Vibration Features by a Time-Scale-Frequency Analysis Method

Shuyou WU[1], Weiguo HUANG[1], Fanrang KONG[1], Qiang WU[1], Fangming ZHOU[1], Ruifan ZHANG[1], Ziyu WANG[1]

[1]Department of Precision Machinery and Precision Instrumentation, University of Science and Technology of China, Hefei, China. Email: wsy1982@mail.ustc.edu.cn

Received September 6th, 2009; revised October 8th, 2009; accepted October 15th, 2009.

ABSTRACT

In order to take advantage of the merits of WPT and HHT in feature extraction from vibration signals of power transformer, a time-scale-frequency analysis method is developed based on the combination of these two techniques. This method consists of two steps. First, the desirable wavelet packet nodes corresponding to characteristic frequency bands of power transformer are selected through a Correlation Degree Threshold Screening (CDTS) technique for reconstructing a time-domain signal that contains useful information of power transformer. Second, the HHT is then conducted on the reconstructed signal to track the instantaneous frequencies corresponding to natural characteristics of power transformer. Experimental results are provided by analyzing a real power transformer vibration signal. Compared with the features extracted by directly using HHT, the features obtained by the proposed method reveal clearer condition pattern of the transformer, which shows the potential of this method in condition monitoring of power transformer.

Keywords: *Power Transformer, Wavelet Packet Transform, Hilbert-Huang Transform, Mother Wavelet Selection, Frequency Bands Screening*

1. Introduction

Power transformer is one of the most significant equipments in power system. Failures of power transformer, especially those caused by core and winding vibration, can lead to worse defects or even severe accident, which will disturb regular production and cause huge economic losses [1]. Therefore, it is necessary to carry out preventive tests and online monitoring.

Moreover, core and winding vibration resulting from core magnetostriction and electrodynamic forces will induce body vibration of transformer. As a result, vibration signals from transformer tank have been widely used to analyze and extract the features which are very important in condition monitoring and health diagnosis of power transformer [2–4]. Early research on vibration analysis methods focused on building power transformer model, and developing the relations between vibration parameters and load current, temperature, etc, while neglecting the rich information hidden in vibration signature. Until the early of this century, research focus has been established that the conditions of winding and core are diagnosed by monitoring and analyzing the vibration signals obtained from the surface of power transformer tank.

Advanced signal processing methods, including Wavelet Transform (WT) and Hilbert Huang Transformation (HHT), have been presented to extract vibration features in recent years [5–9]. WT, which can realize separation of feature information from noises, represents the vibration signals of power transformer in terms of wavelet functions at different scales in the time domain, and then calculates the energy percentages of each signal components in different scale domain and tracks their changes to diagnose if there is any fault. However it should be noted that WT can't provide frequency representation since it is a time-scale analysis technique. Meanwhile the changes of instantaneous frequency and corresponding frequency bands are able to reflect the abnormality of transformer structure [3], such as winding deformation, degeneration of compression and loosening of foundation bolt, etc. Compared to WT, HHT [11] can trace the changes of instantaneous frequency so that it provides unique advantage in analyzing and processing transformer vibration signals. Meanwhile, due to the intrinsic shortcomings [12] in Empirical Mode Decomposition

(EMD) process, the fundamental part of the HHT, the results from HHT will lead to misinterpretation, such as mode mixing and meaningless Intrinsic Mode Functions (IMFs) generation, etc.

The objective of this paper is intended to combine Wavelet Packet Transform (WPT) with HHT to fully use the advantages of both techniques in features extraction from vibration signals and compensate for these specific limitations, consequently a time-scale-frequency analysis method based on WPT and HHT is developed. The paper is arranged as follows. Section 2 will present the theoretical frame, including the brief concepts of WPT and HHT, the selection and optimization of mother wavelet, the screening of desirable frequency bands as well as the flow chart of time-scale-frequency analysis methods. Verification and discussion based on practical experiments will be addressed in Section 3, which shows the potential of this method in condition monitoring of power transformer. A summary will be presented in the final section.

2. Principle

Using the advantages of WPT and HHT techniques in features extraction from vibration signals, a time- scale-frequency analysis method is developed. In this method, effective extraction of vibration features is realized by selecting the energy distribution in each scale domain as feature parameters and tracking the changes of instantaneous frequency and corresponding frequency bands. The procedure of the proposed method is shown in Figure 1, and several specific steps are described as follows.

2.1 Wavelet Packet Transform

WT is an important signal processing method to extract signal features because of its ability in multi resolution analysis. Moreover, the versatility and effectiveness of WT is significantly extended by WPT, the generalized form of WT. Figure 2 shows the decomposition tree of WPT. It is inferred that WPT can be applied to cope with both the approximation and detail coefficients, while WT can only decompose the approximation portion.

Wavelet packet $m_n\left(n=0,1,2,\mathbf{K}\right)$ is defined as

$$\begin{cases} u_{2l}\left(t\right)=\sqrt{2}\sum_{k\in Z}h\left(k\right)u_l\left(2t-k\right) \\ u_{2l+1}\left(t\right)=\sqrt{2}\sum_{k\in Z}g\left(k\right)u_l\left(2t-k\right) \end{cases} \quad l=0,1,2,\mathbf{K} \qquad (1)$$

where $u_0\left(t\right)$ is the orthogonal scaling function, $h\left(k\right)$ and $g\left(k\right)$ are two-scale sequences.

Because WPT is a time-scale domain technique, the energy distributions and variations in each subspace are often selected as signal features. However, it can not provide signal frequency characteristics. Theoretically, increasing decomposition levels can solve this problem, but it is obviously unacceptable due to time cost. Therefore, it is necessary to apply an appropriate time-frequency analysis method to extract frequency information.

2.2 Mother Wavelet Selection

WPT is a process that projects the signal into orthogonal subspaces constructed by the basis functions, which are determined by the selection of mother wavelet. Therefore, the selection of mother wavelet can determine the performance of WPT, for instance, representing the local signal in time-scale domains with the most similarity comparing to the original signal as well as separating the low-energy features from noises. In the researches on features extraction and compression processing for different signals [13–14], such as Electromyography (EMG)

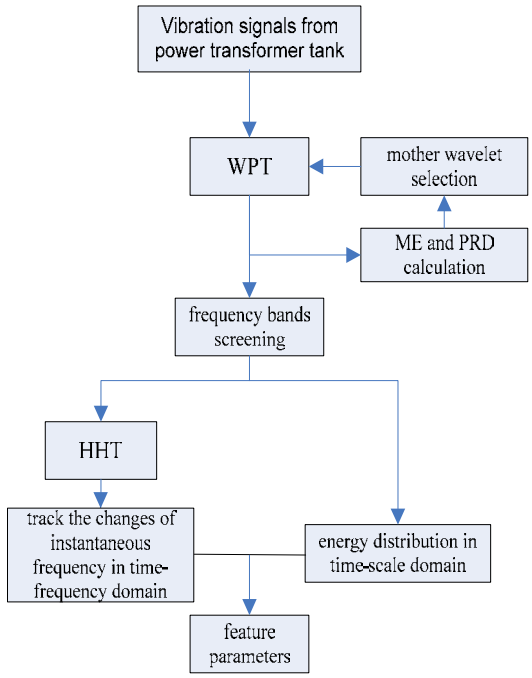

Figure 1. Flow chart of features extraction from vibration signals from power transformer tank based on the time-scale-frequency analysis method proposed in this paper

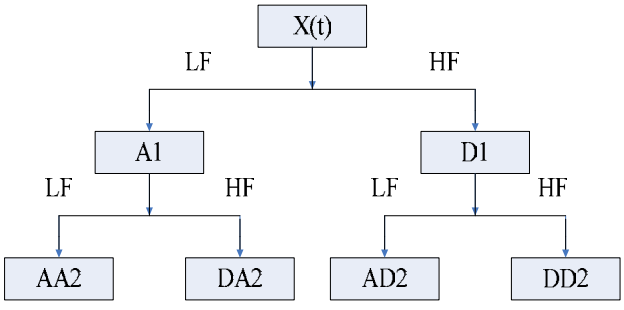

Figure 2. A 2-level WPT decomposition tree

signals, Electrocardiography (ECG) signals, speech signals and images, there are mature research theories for the selection of mother wavelet.

The vibration from the surface of power transformer tank is generated by the vibration of core, winding and cooling devices. Because there is rich vibration information reflecting the conditions of core and winding and huge amounts of noises resulted from electromagnetic interference, selection of mother wavelet function becomes important in features extraction from this kind of vibration signals. However related researches results about how to choose the most appropriate mother wavelet for vibration signals of power transformer tank have not been reported yet.

In this paper 6 kinds of mother wavelets are given, including db20, bior3.7, coif5, rbio5.5, sym10 and dmey, and WPT with these 6 mother wavelets is applied to the signals. From results, the primary frequency features can be acquired by frequency spectrum analysis, and this information can be used to realize wavelet packet reconstruction with the original mother wavelet as the basis function. In order to remove the influence of electromagnetic noises the mean error (ME) and the percent residual difference (PRD) between original signals and reconstructed ones are calculated. Meanwhile ME and PRD have been selected as the criterion to measure the performance of different mother wavelets, that is, smaller ME and PRD values indicate more similar statistical characteristics between the corresponding mother wavelet and analyzed signals. Consequently the optimal mother wavelet is established for vibration signals of power transformer tank, which reduces the blindness of wavelet basis selection and the uncertainty of subsequent features extraction.

2.3 Correlation Degree Threshold Screening

Since each narrow-band signal decomposed by WPT is the orthogonal projection of the inspected signal, the relevant narrow-band signals which contain valuable vibration features should show strong correlation with the original signal, while the meaningless components are expected to indicate weak correlation. According to the above analysis, correlation factor c between each decomposed narrow-band signal and the original signal is obtained and taken as the criterion for screening the meaningful signals. For each correlation factor c_i (where $i = 1, \mathbf{K}\, n$; n is the number of nodes by WPT), the Correlation Degree Threshold (CDT) T is defined as

$$T = \frac{K}{n}\sum_{i=1}^{n} c_i \tag{2}$$

where K is the correction factor and determines the strict degree of screening standard, that is, the bigger K is, the stronger correlation degree between screened frequency bands and original signal there is. In this study, K is set to 1.0.

The frequency bands those corresponding correlation factors are more than or equal to CDT will be retained, and other frequency bands will be discarded.

The screen processing can reduce the noise disturbance and reserve some low-energy but relevant components. Consequently, the efficiency of HHT is further improved and the convincing result will be validated in Section 3.

2.4 Hilbert Huang Transform

HHT, which consists of the EMD and the Hilbert Transform (HT), is firstly proposed by Norden E. Huang in [11]. It has proven to be quite versatile in a broad range of applications to extract useful information from signals generated in noisy nonlinear and non-stationary processes, just like the vibration of power transformer's core and winding, disturbed by electromagnetic field and discharged current.

In the results from HHT, the amplitude a(t) and instantaneous frequency f(t) are also the single-valued function of the time t, so the time-frequency distribution of the amplitude can be extracted. Compared with WT, HHT has its own advantages:

1) HHT can obtain more accurate spectrum structure for higher resolution; 2) HHT is able to extract the frequency distribution properties of vibration signals from power transformer tank; 3) Because the abnormality of transformer structure will be reflected by the changes of modal parameters like natural frequency and corresponding bands, HHT can find those changes to detect the presence of incipient faults.

3. Results and Discussion

3.1 Experiment Principle [2]

Vibrations in a transformer are generated by different forces appearing in the core and winding during the operation.

Winding vibrations are due to electromagnetic forces that are generated by the interaction of the current in a winding with leakage flux. These forces are proportional to the square of the load current

$$F_{winding} \propto i^2 \tag{3}$$

where $F_{winding}$ is electromagnetic forces and i is load current (50 Hz in China).

Meanwhile it is known that the electromagnetic forces are proportional to the windings vibration acceleration

$$F_{winding} \propto a_{winding} \tag{4}$$

So we can conclude that

$$a_{winding} \propto i^2 \tag{5}$$

Then the fundamental frequency of winding vibration acceleration is, 100 Hz, twice the current.

Core vibration is caused by magnetostriction forces. Referring to the conclusion in [10], the core vibration acceleration a_{core} caused by magnetostriction is

$$a_{core} = -\frac{2e_s LU_0^2}{(N_1 AB_s)^2}\cos 2(2p\ f)\ t \qquad (6)$$

where

e_s coefficient of saturation magnetostriction of the silicon steel sheet;

L length of the silicon steel sheet;

U_0 magnitude of voltage-driving source;

f frequency of voltage-driving source (50Hz in China);

N_1 number of drive turns;

A cross sectional area of arm of the core;

B_s saturated magnetic flux density.

Equation (6) indicates that the magnitude of core vibration acceleration is proportional to the square of driving voltage amplitude while the fundamental frequency is 100 Hz (in China), with harmonics being an even multiple of 50 Hz. Higher frequency harmonics are due to the nonlinear character of magnetostriction phenomenon.

Core and winding vibrations caused by the forces transmit through transformer oil and the supporting elements to the tank. When the vibration acceleration signals are obtained from the transformer tank, the fundamental frequency component consists of vibration signals of the windings and that of the core.

When pre-compression is loose or winding deformation occurs, the winding vibration acceleration will enlarge. On the other hand, once the core's compression decreases, temperature varies or insulating layer gets scathing, the core vibration signal will change. Therefore monitoring vibration of the transformer tank is able to acquire essential information about compression and other conditions for both windings and core.

3.2 Testing

Experiments were carried out on a 3-phase power transformer under normal working condition, which related parameters are listed in Table 1. Since the vibration signals obtained from power transformer tank belong to electrical and mechanical vibration ones, it is known that the frequency bandwidth of the inspected signals is about 10-2000 Hz. As a result, piezoelectric accelerometers are prior choice and ICP 601A01, which scope is ±50g and has a sensitivity of 100 mv/g as well as the frequency response within 0.27~10 kHz, is adopted. The AD data acquisition card with USB ports ART USB2000A is selected to convert the analog signals to digital ones with the resolution of 16 bits and 100 kHz maximum sampling frequency. The laptop is used for signals processing and storage center.

Three ICP 601A01 type vibration acceleration sensors are placed on the surface of phase A, B and C in high voltage side of power transformer tank via the magnetic pedestal, and another three vibration acceleration sensors are attached in low voltage side. It should be noted that all the sensors are tightly fixed on the surface of the tank and at the same horizontal level. The sampling frequency is set to be 10 kHz. Thus desirable digital signals are collected and to be analyzed.

The time-domain vibration wave of phase A in high voltage is shown in Figure 3(a). As shown in FFT spectrum in Figure 3(b), the spectrum of the signal indicates the fundamental frequency is 100 Hz with multiple harmonics in tank vibration signals of power transformer. Above 1000 Hz, frequency components are near zero.

Table 1. Power transformer parameters

Type:	S7—800/10	Rated Voltage:	(10000±5%)/400
Rated Power:	800kVA	Frequency:	50Hz /3 phase

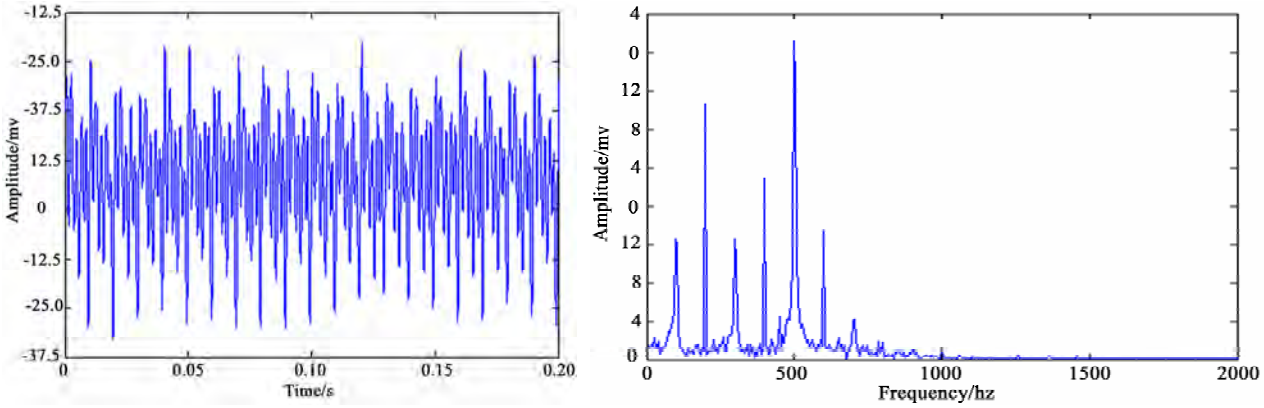

(a) (b)

Figure 3. The time-domain wave of power transformer tank and corresponding FFT spectrum

3.3 WPT Processing

First 6 kinds of mother wavelets are given, including db20, bior3.7, coif5, rbio5.5, sym10 and dmey, and 6-level WPT with these 6 mother wavelets is performed to 20 groups of vibration signals obtained from phase A in high voltage side of power transformer tank. Then based on the rough frequency characteristics inferred from the FFT spectrum of the vibration signal of power transformer tank in Figure 3, low-frequency parts (lower than 1200 Hz) are selected for wavelet packet reconstruction using the original mother wavelet as the basis function. Finally the mean error (ME) and the percent residual difference (PRD) between original signals and reconstructed ones are calculated and quantified, which are described in Figure 4 and Figure 5.

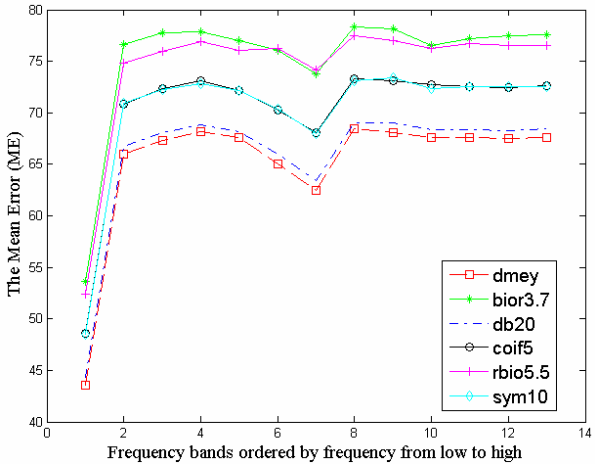

Figure 4. The mean error (ME) between original signals and reconstructed ones using 6 mother wavelets

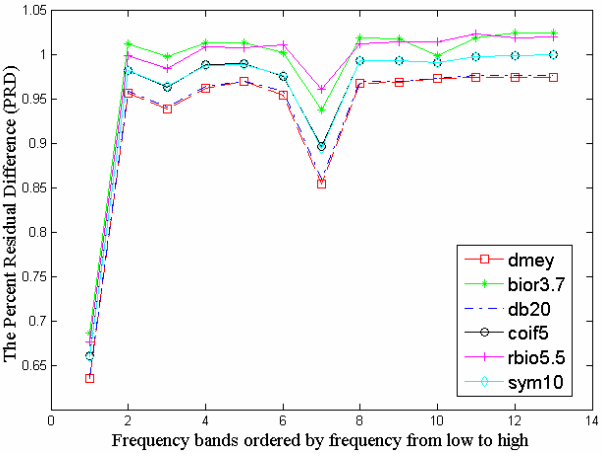

Figure 5. The percent residual difference (PRD) between original signals and reconstructed ones using 6 mother wavelets

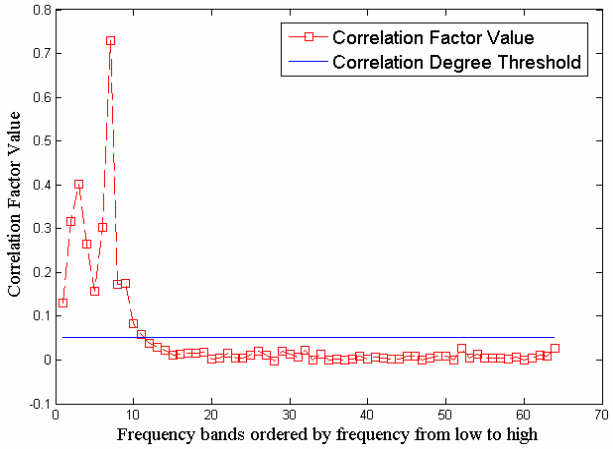

Figure 6. The Correlation Degree Threshold (CDT) and correlation factors that show the correlation degree between the reconstructed signals and original signal

It is inferred from Figure 4 and Figure 5 that mother wavelets dmey and db20 showed their potential for decomposing the signals from power transformer tank and guaranteed the minimum distortion, that is, there are more similar statistical characteristics between the corresponding mother wavelet and analyzed signals. However mother wavelets bior3.7 and rbio5.5 are not suitable for this kind of vibration signals and should not be used. Therefore the results can provide theoretical and practical basis if wavelet theory is adopted for monitoring and analyzing the conditions of power transformer.

According to the above experiment results, the Dmey mother wavelet has been chosen to apply 6-level wavelet packet decomposition with the original vibration signals. Wavelet packet reconstruction is carried out on the 64-group wavelet coefficients generated by wavelet packet decomposition and then the correlation factors that show the correlation degree between the reconstructed signals and original signal are calculated. Meanwhile the Correlation Degree Threshold (CDT) is given by Equation (2). The 64 correlation factors and the CDT are displayed in Figure 6, in which red square box and blue line have been used as markers respectively. Those frequency bands which correlation factors are over than CDT will be reserved and other bands discarded. Through the frequency bands screening process, 11 frequency bands are obtained. The energy distribution percentage is acquired by calculating and normalizing the energy of 11 reserved frequency bands. The above energy distribution in time-scale domain is selected as feature parameters (listed in Table 2) because it can reflect the conditions of power transformer [3].

3.4 HHT Processing

Wavelet packet reconstruction is implemented before EMD using the 11 frequency bands obtained by screen-

ing process. Through EMD the reconstructed signal is decomposed into 8 the supplement to WPT-energy monitoring method IMFs, shown in Figure 7(b). Subsequently HT is applied to every IMF to get the hilbert spectrum which presented in Figure 8(b). It is easily observed that the instantaneous frequency and its changes can be tracked and analyzed comparing with single WPT.

4. Discussion

1) From Figures 4 and 5, it is summarized that appropriate mother wavelet selection can reduce the decomposition and reconstruction error, improve the pertinence of feature extraction and avoid misleading identification results of the status of power transformer. Moreover, the CDTS technique can reserve the frequency bands that show stronger correlation with the analyzed signal and can eliminate the noises part.

2) Comparing the results in Figure 7(a) to those in Figure 7(b), it is exciting that more desirable and meaningful IMFs are acquired through performing EMD on the reconstructed signal by WPT and CDTS processing, which shows the importance of mother wavelet selection and CDTS.

3) According to the methods described in literature [8] and [9], the Hilbert spectrum obtained by directly applying HHT to the original signal is shown in Figure 8(a), which has big difference from the frequency characteristics laid in Figure 3(b). Some main differences are listed as follows: a) The illusive low-frequency portion (less than 100Hz) in Figure 8(a) would lead to misunderstanding about the frequency characteristics in comparison with the results shown in Figures 3(b) and 8(b) b) With HHT method, mode mixing phenomena in Figure 8(a) would make it difficult to identify the meaningful frequency bands, while results of developed method as shown in Figure 8(b) are consistent with the frequency characteristics of power transformer vibration described in Figure 3(b). Moreover, the changes of the instantaneous frequency and corresponding bands can be monitored and analyzed.

Table 2. The energy distribution percentage (%) of 11 reserved frequency bands ordered by scale from big to small

Frequency Bands Number	1	2	3	4	5	6	7	8	9	10	11
Energy Distribution Percentage	56.54	3.54	6.95	2.48	1.06	3.76	22.25	1.39	1.27	0.24	0.11

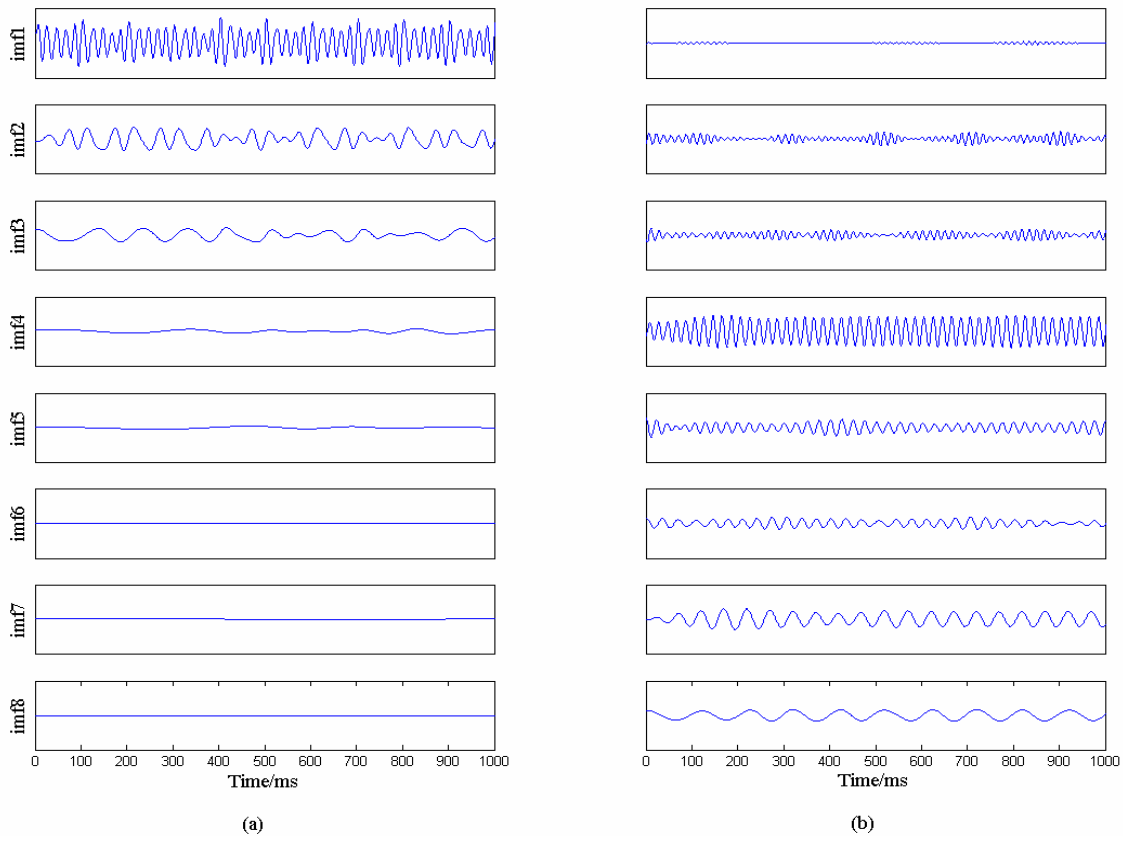

Figure 7. (a) IMFs obtained by EMD with the original vibration signal; (b) IMFs obtained by EMD with the reconstructed signal by WPT and correlation degree threshold screening

Table 3. The frequency characteristics obtained by the developed method in the paper

Frequency Bands Number	1	2	3	4	5	6	7	8
Center Frequency (Hz)	101	198	302	405	510	614	663	810
Frequency Bands Range (Hz)	92, 111	198, 209	247, 312	373, 414	509, 519	560, 620	610, 740	790, 826

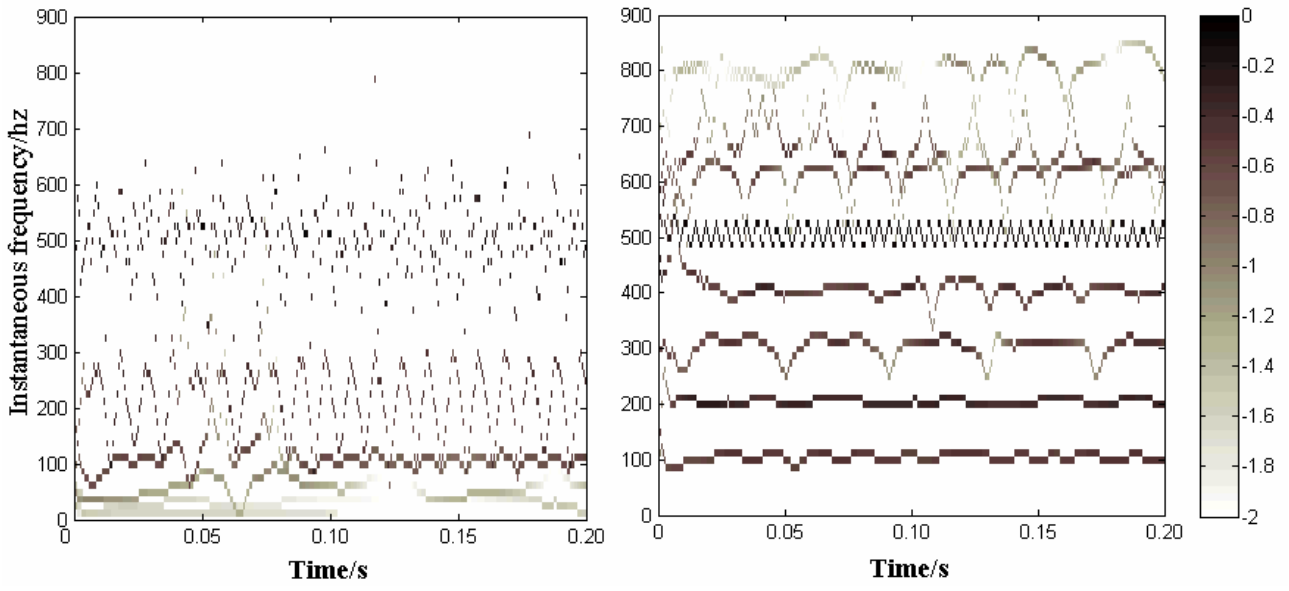

Figure 8. (a) The Hilbert spectrum by directly using HHT to the original signal; (b) The Hilbert spectrum by the time-scale-frequency method developed in this paper

4) From Table 2 it is observed that energy distribution percentages of many frequency bands are under 1% or even smaller, which will increase the requirement for resolution of condition monitoring. It would be very difficult to monitor and analyze the conditions of power transformer by using only WPT-energy method like references [5] and [7]. In order to avoid the limitation, the changes of the instantaneous frequency and corresponding frequency bands as listed in Table 3 can be used as the supplement to WPT-energy monitoring method.

5. Conclusions

In this paper, a time-scale-frequency analysis method based on the combination of WPT and HHT is proposed and applied to feature extraction from vibration signals of power transformer tank. Experiment results show the potential of this method in condition monitoring of power transformer. The following conclusions can be drawn:

1) According to the results based on this study, the mother wavelets that are suited to decompose vibration signals of power transformer tank are established;

2) Compared to the results by directly using HHT, the results obtained by the developed method can reveal better frequency characteristics of power transformer vibration to effectively trace and detect the abnormality of transformer structure.

REFERENCES

[1] C. Myers, "Transformers condition monitoring by oil analysis," Large or Small: Contentment or Catastrophe, Proceedings of the 1998 1st IEE/IMeChE International Conference on Power Station Maintenance-Profitability through Reliability, pp. 53–58, 1998.

[2] S. Ji, "The study of winding and core vibration characteristics and application in fault monitoring of transformer," PHD Thesis, Xi'an JiaoTong University, China, 2003.

[3] J. C. Lavalle, "Failure detection in transformers using vibration analysis," MS Thesis, MIT, Cambridge, MA, USA, 1986.

[4] Z. Berler, A. Golubev, V. Rusov, *et al*, "Vibro- acoustic method of transformer clamping pressure monitoring," Conference Record of the 2000 IEEE International Symposium on Electrical Insulation, Anaheim, CA USA, pp. 263–266, 2000.

[5] S. Ji, W. Liu, *et al*, "The application of the wavelet packet to monitor the core and winding condition of transformer based on the vibration analysis method," Proceedings of Chinese Society for Electrical Engneering, Vol. 21, No. 12, pp. 24–27, 2001.

[6] P. Kang and D. Birtwhistle, "Condition monitoring of power transformer on-load-tap-changers using wavelet analysis," IEEE Transactions on Power Delivery, Vol. 16, No. 3, pp. 394–400, 2001.

[7] Q. Yan, X. Liu, and J. Yin, "Features of Vibration Signal of Power Transformer Using the Wavelet Theory," High Voltage Engineering, Vol. 33, No. 1, pp. 165–168, 2007.

[8] W. Xiong and G. Zhao, "Analysis of transformer core vibration characteristics using hilbert-huang transformation," Transactions of China Electrotechnical Society, Vol. 21, No. 8, pp. 9–13, 2006.

[9] W. Xiong and R. Ji, "Nonlinear time series analysis of transformer's core vibration," The 6th World Congress on Intelligent Control and Automation. Dalian China, pp. 5493–5496, 2006.

[10] S. Ji, Y. Luo, and Y. Li, "Research on extraction technique of transformer core fundamental frequency vibration based on OLCM," IEEE Transactions on Power Delivery, Vol. 21, No. 4, pp. 1981–1988, 2006.

[11] N. E. Huang, Z. Shen, S. R. Long, *et al*, "The empirical mode decomposition and the hilbert spectrum for nonlinear and non-stationary time series analysis," Proceedings of Royal Society of London, Series A, pp. 903–994, 1998.

[12] Z. Peng, P. Tse, and F. Chu, "A comparison study of improved hilbert-huang transform and wavelet transform: Application to fault diagnosis for rolling bearing," Mechanical Systems and Signal Processing, Vol. 19, No. 5, pp. 974–988, 2005.

[13] L. Brechet, M. Lucas, C. Doncarli, and D. Farina, "Compression of biomedical signals with mother wavelet optimization and best-basis wavelet packet selection," IEEE Transactions on Bio-medical Engineering, Vol. 54, No. 12, pp. 2186–2192, 2007.

[14] B. S. Shajeemohan, V. K. Govindan, and B. Vijilin, "A scheme for image classification and adaptive mother wavelet selection," International Conference on Advanced Computing and Communications, pp. 308–313, 2006.

J. Electromagnetic Analysis & Applications, 2010, 2: 39-44
doi:10.4236/jemaa.2010.21006 Published Online January 2010 (http://www.SciRP.org/journal/jemaa)

Research on a New Control Strategy of Three Phase Inverter for Unbalanced Loads

Wenhua HU[1,2], Weiming Ma[3],Chunxi LIU[4]

[1]Huazhong University of Science and Technology, Wuhan, China; [2]East China Jiaotong University, Nanchang, China; [3]Naval University of Engineering, Wuhan, China; [4]Zhejiang University, Hangzhou, China.
Email: ecjtumotor@hotmail.com

Received July 24th, 2009; revised September 2nd, 2009; accepted September 7th, 2009.

ABSTRACT

One of the very important functions of three-phase inverter is to maintain the symmetric three-phase output voltage when the three-phase loads are unbalanced. Although the traditional symmetrical component decomposing and superimpose theory can keep the voltage balance through compensating the positive-, negative- and zero-sequence components of the output voltage of inverter, however, this method is time-consuming and not suitable for control. Aiming at high power medium frequency inverter source, a P+Resonant (Proportion and Resonant) controller which ensured a balanced three phase output voltage under unbalanced load is proposed in this paper. The regulator was proved to be applicable to both three-phase three-wire system and three-phase four-wire system and developed two methods of realization. The simulation results verified that this method can suppressed effectively the output voltage distorted caused by the unbalanced load and attained a high quality voltage waveforms.

Keywords: *Three-Phase Inverter, Unbalanced Load, the Three-Phase Output Voltage Symmetric, Medium Frequency, P+Resonant Controller*

1. Introduction

In recent decades, with the rapid development of power electronics technology and the improving requirements of electrics device performance in trades and industries, the inverter technology are increasing widespread used in multi-domain. Accordingly, there have more and more requirements for inverter power. Many electrics devices of industries are not use directly grid but inverters as their power source. Some important power-consuming departments and electrics devices, especially in high power medium frequency system, such as vessel and aircraft, require more high quality of the source, demand the voltage, frequency and waveform accurate, have a good dynamic state performance and no any disturbance from the source.

In three-phase system, however, unbalanced instances can occur in power systems for a variety of cases, such as, three imbalanced load, unsymmetrical parameters of three-phase filter, single-phase load, and so on. Unbalanced loading causes negative- and zero-sequence currents (in four-wire systems) to flow in the power system. For ideal sources this would not be a problem. However, inverter source systems, especially high power 400Hz inverter source systems, with finite output impedances, will experience voltage distortion in the form of phase voltage imbalance and phase shift due to unbalanced loading. At worst, unbalanced voltages can cause malfunction and even failure of power-consuming equipment. Thus, in inverter-fed power systems, it is the responsibility of the inverter to ensure that certain tolerances on phase voltage imbalance at the load terminals are met under specified loading conditions. Reference [1] proposed a method of extending controller bandwidth. By transforming abc to dqo, the negative- and zero-sequence components can be view as a disturbance of $2w$ and w respectively. By utilizing controllers with bandwidths greater than the frequency of the disturbances, some attenuation will be achieved and the output voltage balance may be ensured. While this may be possible in low power 50/60Hz inverters, it would be very difficult, and likely impossible, to accomplish in high power inverters due to the difficulties of improving the switching frequency. The impossibility of this option is amplified for inverters with high output fundamental frequencies, such as the inverter under study. Reference [2] put forward a method of load current feedforward control. By using load current feedforward, the output voltage balance can be

Project Supported by National Nature Science Foundation of China (50607020), (50737004ZD) and (50721063).

promised. In general, true feedforward assumes that the variables that are fed forward are known and independent of the controlled system. However, in the case of the load currents feedforward, the assumptions are false, because the load currents are closely coupled to the plant state variables. Thus, this feedforward control in fact forms a feedback loop. As a result, the system stability is affected and must be examined. Reference [3] proposed a double dq transform control method. Although this method can eliminate the negative-sequence component, it can do nothing for zero-sequence component. Moreover, this control strategy is time-consuming and not suitable for control.

Firstly, this paper analyzed the mathematical model of the three-phase inverter and the application of the symmetrical component decomposing in engineering. As for three-phase two H-bridge units cascaded topology, a resonant controller is proposed and simulations on a three-phase 30kVA medium frequency inverter under unbalanced load are carried out. The results verified that the resonant controller can be used to satisfy completely output voltage balance under any unbalanced loads.

2. Model of Three-Phase Inverter Source and Unbalance Analysis

The topology of three-phase inverter under study is shown in Figure 1. Only phase A is presented detailedly here for the sake of space limitation. Each phase consist of DC bus voltage U_d, two H-bridge inverter, two transformer T, filter inductor L, filter capacitor C and load R which can be balanced load, unbalanced load, single-phase load, and so on. r represent the integrative effect of ESR of filter inductor, dead time of the inverter, and so on. Unipolar modulation is adopted in the single H-Bridges whose outputs are in series at secondary of H-bridge and interleaving control is done between two two transformers. There are 90 phase degree difference between corresponding carrier waves of two H-Bridges and the modulating waves are the same, so the equivalent switching frequency of inverter is four times of the device switching frequency and the output voltage has five-level waveforms that means harmonics content in output voltage resulting from the switching is reduced.

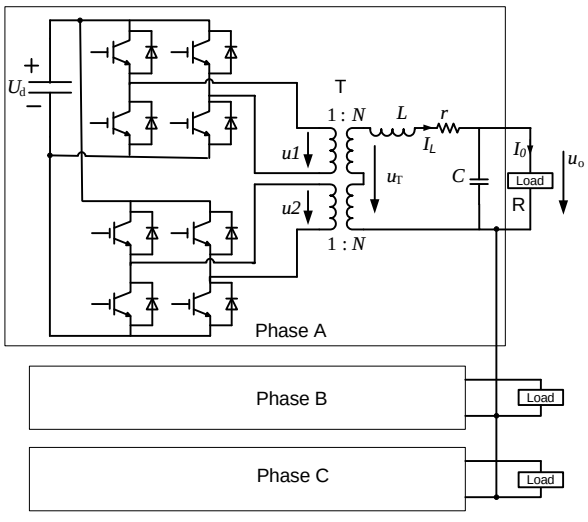

Figure 1. The two H-bridge units cascaded three-phase inverter topology

In Figure 1, u_{Ta}、u_{Tb}、u_{Tc} represent the output phase voltage of transformer, u_{0a}、u_{0b}、u_{0c} represent the three voltage of filter capacitor, i_{1a}、i_{1b}、i_{1c}represent the three current of filter inductor and i_{0a}、i_{0b}、i_{0c} represent the three line current. According to KCL and KVL, Formula (1) can be written out:

$$p\begin{bmatrix} u_0 \\ i_1 \end{bmatrix} = \begin{bmatrix} 0 & \frac{1}{C}I_3 \\ -\frac{1}{L}I_3 & -\frac{r}{L}I_3 \end{bmatrix} \mathbf{g} \begin{bmatrix} u_0 \\ i_1 \end{bmatrix} + \begin{bmatrix} 0 & -\frac{1}{C}I_3 \\ \frac{1}{L}I_3 & 0 \end{bmatrix} \mathbf{g} \begin{bmatrix} u_T \\ i_0 \end{bmatrix} \tag{1}$$

where p denotes differential operator, $u_0 = [u_{0a} \ u_{0b} \ u_{0c}]^T$ denotes the output voltage vector of inverter, $i_1 = [i_{1a} \ i_{1b} \ i_{1c}]^T$ denotes current vector of filter inductor, $u_T = [u_{Ta} \ u_{Tb} \ u_{Tc}]^T$ denotes the output voltage vector of transformer, $i_0 = [i_{0a} \ i_{0b} \ i_{0c}]^T$ denotes the current vector of load and I_3 denotes a unit matrix of three by three.

If u_{0a}、u_{0b}、u_{0c} and i_{1a}、i_{1b}、i_{1c} were taken as state variables, then Formula (1) and (2) make up of the plant state equation of Figure 1.

$$y = [u_{0a} \ u_{0b} \ u_{0c}]^T \tag{2}$$

Unbalanced output phase voltages or currents phasor can be symmetrically decomposed into their positive-, negative- and zero-sequence components. Assume Va, Vb and Vc represent three phase voltage phasor, then:

$$\begin{bmatrix} V_a \\ V_b \\ V_c \end{bmatrix} = \begin{bmatrix} V_{a+} \\ V_{b+} \\ V_{c+} \end{bmatrix} + \begin{bmatrix} V_{a-} \\ V_{b-} \\ V_{c-} \end{bmatrix} + \begin{bmatrix} V_{a0} \\ V_{b0} \\ V_{c0} \end{bmatrix} \tag{3}$$

$$\begin{cases} [V_{a+} \ V_{b+} \ V_{c+}]^T = V_+ \mathbf{g} [1 \ a \ a^2]^T \\ [V_{a-} \ V_{b-} \ V_{c-}]^T = V_- \mathbf{g} [1 \ a^2 \ a]^T \\ [V_{a0} \ V_{b0} \ V_{c0}]^T = V_0 \mathbf{g} [1 \ 1 \ 1]^T \end{cases} \tag{4}$$

$$[V_+ \ V_- \ V_0]^T = \frac{1}{3} \mathbf{g} \begin{bmatrix} 1 & a^2 & a \\ 1 & a & a^2 \\ 1 & 1 & 1 \end{bmatrix} \mathbf{g} [V_a \ V_b \ V_c]^T \tag{5}$$

where $a = e^{-j120}$, subscript a, b, c represent three

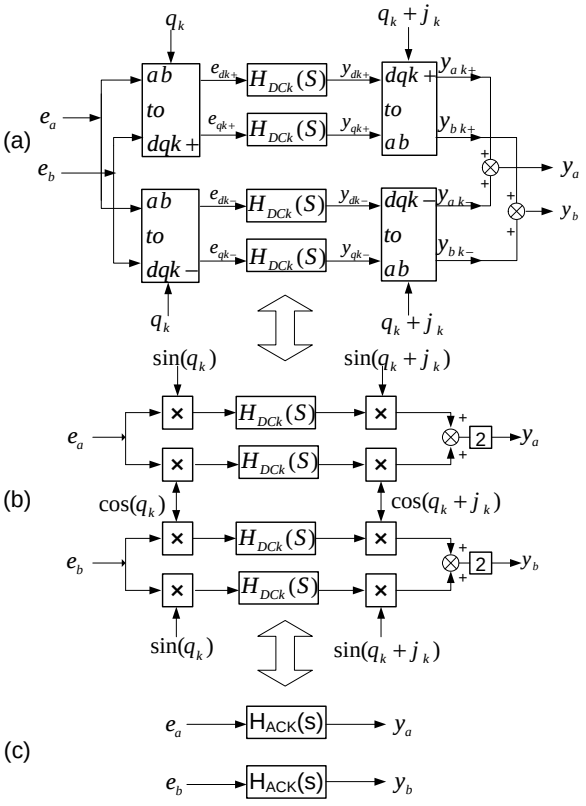

Figure 2. Resonant controller of three-phase system

phase electricity respectively, subscript +, -, 0 represent positive-, negative- and zero-sequence components respectively.

3. Resonant Regulator

It is known from analysis aforementioned that due to near zero impedance which ideal sources possess, the voltage dropping of impedance caused by negative- and zero-sequence current components due to unbalanced load is almost zero and unbalanced load has little influence on ideal sources. So if the output voltage of inverter is not suffer from the unbalanced load is expected, the output impedance of inverter source must be near zero too. It is known from control theory that if a near zero impedance of a system is expected, the open loop gain of the control system must be attain infinite at certain signal frequency.

3.1 Resonant Controller with abg as Input and Output Variable

Figure 2 is the resonant controller of three-phase system. By transforming abc to $\alpha\beta$, the output voltage errors of abc coordinate can be transfer to $\alpha\beta$ coordinates variable $\dot{e}_{ab}(\dot{e}_{ab} = e_a + je_b)$. Following the scheme of Figure 2(a), the output voltage errors $\dot{e}_{ab}(\dot{e}_{ab} = e_a + je_b)$ in ab coordinates are first converted into synchronous reference frame quantities $\dot{e}_{k+}(\dot{e}_{k+} = e_{dk+} + je_{qk+})$, $\dot{e}_{k-}(\dot{e}_{k-} = e_{dk-} + je_{qk-})$ using both positive- $(dqk+)$ and negative- $(dqk-)$ sequence transformations rotating at angular frequency $q_k = kwt$ (i.e., $\dot{e}_{k+} = e^{jq_k}\dot{e}_{ab}$, $\dot{e}_{k-} = e^{-jq_k}\dot{e}_{ab}$) where k is the order of the generic harmonic to be compensated and w is the fundamental angular frequency. All synchronous reference frame errors $(e_{dk+}, e_{dk-}, e_{qk+}, e_{qk-})$ are then compensated by regulators $H_{DCk}(S)$, which ensure zero steady-state errors for each positive- and negative-sequence harmonic component. Then, the output of each regulator $(y_{dk+}, y_{dk-}, y_{qk+}, y_{qk-})$ is converted back to the stationary reference frames and possibly adding a leading angle j_k which compensates for the delay of the remaining process. The structure is complicated which need compensate for each order harmonics including positive- and negative- sequence components. Moreover, coupling may be exist between the d and q axis variables.

There will exist zero-sequence component if the three-phase system is imbalanced. Of course, any possible zero-sequence component cannot be compensated in Figure 2. However, zero sequence component can be control by the resonant controller also. This will be discussed later.

Some simplifications of the theoretical scheme of Figure 2(a) are possible [4,5]. First, it is easy to verify that the compensation of both positive- and negative-sequence harmonic components for a generic harmonic k is equivalent to the synchronous demodulation of the ab components, shown in Figure 2(b), as long as all regulators $H_{DCk}(S)$ in Figure 2(a) and (b) have the same transfer function. Secondly, even the scheme of Figure 2(b) can be further simplified since it is equivalent to the scheme of Figure 2(c) with stationary-frame regulators $H_{ACk}(S)$. The proportion term can be put outside the transform due to the proportion is same in stationary reference frame and synchronous reference frame.

By deducing, the transform formula $H_{ACk}(S)$ is [4]:

$$\begin{aligned} H_{ACk}(s) = \cos j_k [H_{DCk}(s - \mathrm{j}kw) + H_{DCk}(s + \mathrm{j}kw)] \\ + \mathrm{j}\sin j_k [H_{DCk}(s - \mathrm{j}kw) - H_{DCk}(s + \mathrm{j}kw)] \end{aligned} \quad (6)$$

If

$$H_{DCk}(S) = \frac{K_{Ik}}{S} \quad (7)$$

Then

$$H_{ACk}(S) = 2K_{Ik}\left(\frac{S\cos j_k - kw\sin j_k}{S^2 + (kw)^2}\right) \quad (8)$$

If the delay compensating is not take into account in Formula (8), then

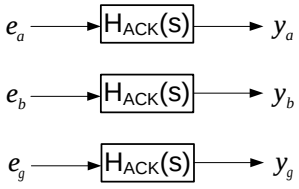

Figure 3. Control block of three-phase four-wire system

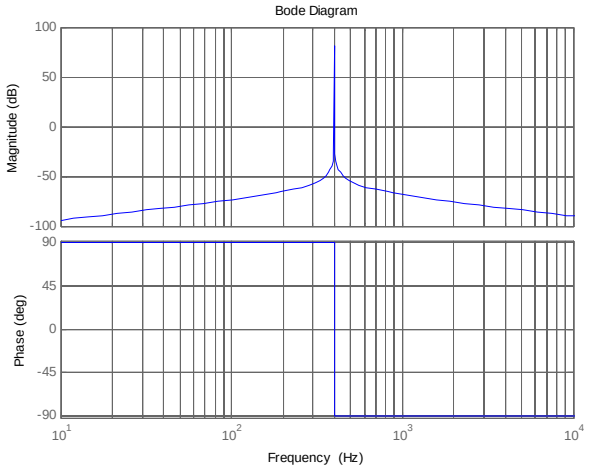

(a)

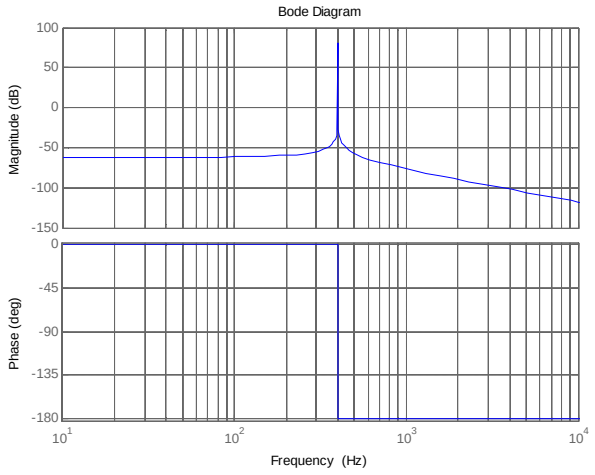

(b)

Figure 4. Bode plot of resonant regulator($K_{I1}=1$, $\omega=800\pi$). (a) Bode plot of (9) where k=1; (b) Bode plot of (11)

$$H_{ACk}(S)=\frac{2K_{Ik}S}{S^2+(kw)^2} \tag{9}$$

where ω denotes the fundamental frequency of reference signal, k denotes order of harmonics, K_I denotes the gain of integral term.

It is known from [6] that when the load is unbalanced load or nonlinear load and a balance of output voltage is expected, which means the zero sequence component need be compensated, a three-phase four-wire system must be adopted. In Figure 2, however, only $\alpha\beta$ axis are taken into account. If the system is a three-phase four-wire system, g axis also need be thought over. It is known from coordinate transform theory that αβ axis variable are positive- and negative-sequence component and g axis variable is zero-sequence component. The method shown in Figure 2(a) can be used to process the positive- and negative-sequence component of αβ axis and the method shown in Figure 2(b) can be adopted to deal with the zero-sequence component of g axis. i.e. resonant controller can be used to deal with all abg axis variable. The control block is shown in Figure 3.

The matrix form is shown in Formula (10)

$$\begin{bmatrix} Y_a(S) \\ Y_b(S) \\ Y_g(S) \end{bmatrix} = \begin{bmatrix} \frac{2K_iS}{S^2+w^2} & 0 & 0 \\ 0 & \frac{2K_iS}{S^2+w^2} & 0 \\ 0 & 0 & \frac{2K_iS}{S^2+w^2} \end{bmatrix} \begin{bmatrix} E_a(S) \\ E_b(S) \\ E_g(S) \end{bmatrix} \tag{10}$$

It is can be seen from (10) that the term of non-diagonal is zero which means there are no coupling among abg variable and can be decoupled as single-phase.

The bode diagram of Formula (9) where k is equal to one is shown in Figure 4(a). It can be seen from Figure 4(a) that the regulator has an infinite gain (it is a finite value in the bode diagram due to simulation step and truncation error) at certain frequency. Then the gain of open loop which including the resonant controller will achieve infinite(as for unit negative feedback system, the gain of open loop is equal to transfer function of controller multiply transfer function of object) and zero steady state error between output voltage and reference voltage can be promised.

It is also noted that the controller presented in (9) has a transfer function similar to that presented by Sato *et al.* [7], which has a resonant transfer function given by

$$H_{AC}(S)=\frac{2K_{I1}w}{S^2+(w)^2} \tag{11}$$

Sato's transfer function also has infinite gain at the resonant frequency and hence can be used to suppress the output voltage distorted caused by the unbalanced loads. However, it in particular introduces a phase shift of 180 into the system, compared to the 90 shift of the P+Resonant system, as illustrated in Figure 4(b). In closed loop operation this 180 phase shift results in a poorer phase margin and a poor transient performance for this regulator compared to the approach presented here.

3.2. Resonant Controller with ABC as Input and Output Variable

The resonant controllers which induced before are with

abg as input and output variable. However, practical three-phase systems are with abc as input and output variable. The deduction of the relations of controller with abc as input and output variable and controller with abg as input and output variable is shown as follows:

It can be know from stationary coordinate transformation theoretics,

$$T_{abc}^{abg} = \sqrt{\frac{2}{3}} \begin{bmatrix} 1 & -\frac{1}{2} & -\frac{1}{2} \\ 0 & \frac{\sqrt{3}}{2} & -\frac{\sqrt{3}}{2} \\ \frac{1}{\sqrt{2}} & \frac{1}{\sqrt{2}} & \frac{1}{\sqrt{2}} \end{bmatrix} \tag{12}$$

$$T_{abg}^{abc} = \sqrt{\frac{2}{3}} \begin{bmatrix} 1 & 0 & \frac{1}{\sqrt{2}} \\ -\frac{1}{2} & \frac{\sqrt{3}}{2} & \frac{1}{\sqrt{2}} \\ -\frac{1}{2} & -\frac{\sqrt{3}}{2} & \frac{1}{\sqrt{2}} \end{bmatrix} \tag{13}$$

So the relation of variable in abc coordinate and variable in abg coordinate is:

$$x_{abg} = T_{abc}^{abg} \mathrm{g} x_{abc} \quad \text{and} \quad x_{abc} = T_{abg}^{abc} \mathrm{g} x_{abg}$$

Then

$$\begin{aligned} Y_{abc}(S) &= T_{abg}^{abc} \mathrm{g} Y_{abg}(S) = T_{abg}^{abc} \mathrm{g} G_{abg}(S) E_{abg}(S) \\ &= T_{abg}^{abc} G_{abg}(S) T_{abc}^{abg} \mathrm{g} E_{abc}(S) \\ &= G_{abc}(S) \mathrm{g} E_{abc}(S) \end{aligned} \tag{14}$$

where $G_{abc}(S) = T_{abg}^{abc} \mathrm{g} G_{abg}(S) \mathrm{g} T_{abc}^{abg}$

If $G_{abg}(S)$ equal to Formula (10),

Then

$$G_{abc}(S) = \begin{bmatrix} \frac{2K_i S}{S^2 + w^2} & 0 & 0 \\ 0 & \frac{2K_i S}{S^2 + w^2} & 0 \\ 0 & 0 & \frac{2K_i S}{S^2 + w^2} \end{bmatrix} \tag{15}$$

It can be seen from (15) that the element of non-diagonal is zero, which means there are no coupling among abc variable and can be decoupled as single-phase.

It must be emphasis on that the system must be three-phase four-wire system when apply Formula (10) or (15). This is because zero-sequence component can only be compensated in three-phase four-wire system. As for three-phase three-wire system, Formula (10) or (15) can not be used directly. However, by weeding the zero-sequence component of feedback variable and ensuring the input variable of g axis equal to zero, Formula (10) or (15) can be used in three-phase three-wire system. Moreover, in general, line to line voltage can only be gotten in three-wire system and phase voltage which educed from line to line voltage satisfy automatically the condition that input variable of g axis equal to zero.

4. Simulation Investigations

In order to illustrate the resonant controller is effective on unbalanced load, the proposed control strategy has been investigated using MATLAB/Simulink simulations on both three-phase three-wire system and three-phase four-wire system. The load is Y or Yn connected and loads of phase A, B and C are 1.5Ω, 1.5Ω and 15Ω respectively. Table 1 defines the parameters used in simulations.

The output voltage waveforms of three-phase four-

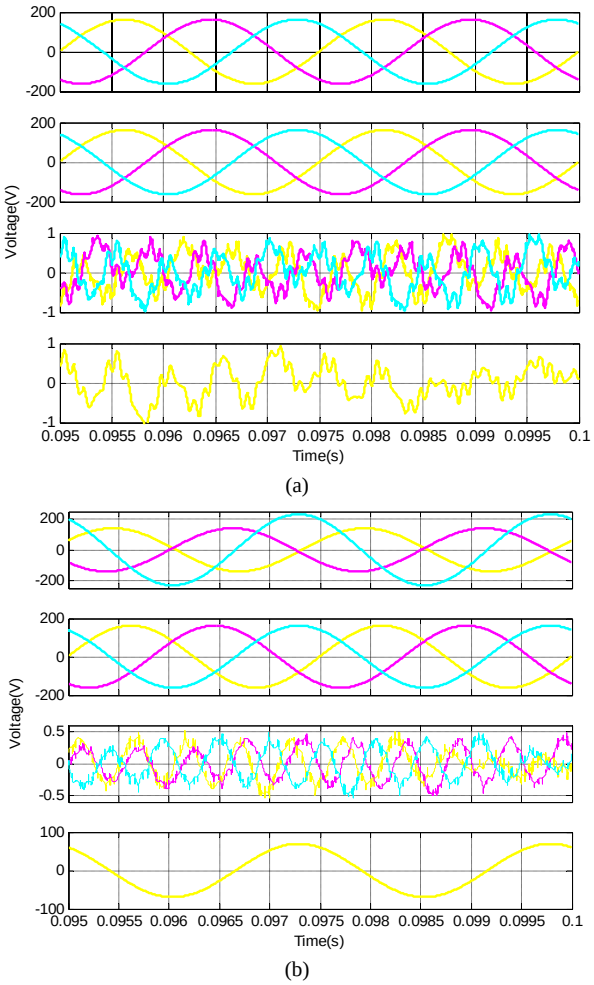

Figure 5. Output voltage waveforms under resonant controller(from up to down are in turn three-phase voltage, positive-, negative- and zero-sequence components of output voltage). (a) Three-phase four-wire system; (b) Three-phase three-wire system

Table 1. Simulation parameters of the system

parameter	value	parameter	value
S	30 kVA	N	0.2
f_s	2.8kHz	V_{ref_RMS}	115V
U_d	513V	f	400Hz
L	26uH	K_p	12
C	440uF	K_I	500
r	10mΩ		

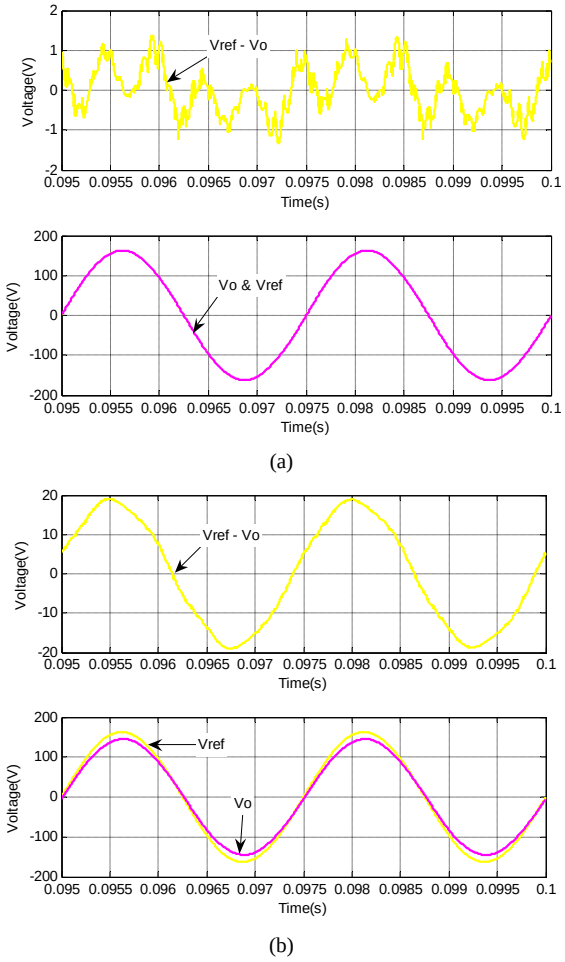

Figure 6. Error voltage and output voltage, reference voltage waveforms of three-phase four-wire system. (a) Resonant controller; (b) Proportion controller

wire and three-phase three-wire system under resonant controller are shown in Figure 5(a) and (b) respectively. It can be seen from Figure 5(a), that the negative- and zero-sequence component can be depressed by resonant controller in three-phase four-wire system. It can be seen from Figure 5(b) that only negative-sequence component can be depressed by resonant controller in three-phase three-wire system. There are still positive- and zero-sequence component in output voltage (positive-sequence component is system need, zero-sequence component is system didn't need but remaining due to the three-phase three-wire configuration).

The error voltage and output voltage V_o, the reference voltage V_{ref} waveforms of three-phase four-wire system under resonant controller are shown in Figure 6(a). It can be seen from (a) that the error is almost zero and the output voltage is superposition with reference voltage which proved the correct of analysis aforementioned. In order to compare, Figure 6(b) gave the waveforms under proportion regulator. It can be seen from (b) that there are obvious steady state amplitude and phase error between the reference voltage and the output voltage.

5. Conclusions

This paper analyzed the output voltages distortion mechanism under unbalanced load, a three-phase two H-bridge units cascaded topology is presented and the equivalent switching frequency of inverter is improved effectively. A P+Resonant controller which ensured a balanced three phase output voltage under unbalanced load is proposed for high power medium frequency inverter sources. The regulators proved to be applicable to both three-phase three-wire system and three-phase four-wire system and two methods of realization were developed. The simulation results verified that this method can suppressed effectively the output voltage distorted caused by the unbalanced load and attained a high quality voltage waveforms.

REFERENCES

[1] R. A. Gannett, "Control strategies for high power four-leg voltage source inverters," Virginia Tech, 2001.

[2] R. Zhang, "High performance power converter systems for nonlinear and unbalanced load/source," Virginia Tech, 1998.

[3] P. Hsu and M. Behnke, "A three-phase synchronous frame controller for unbalanced load," IEEE-PESC'98 Record, Fukuoka, Japan, Vol. 2, No. 5, pp. 1369–1374, 1998.

[4] P. Mattavelli, "Synchronous-frame harmonic control for high-performance AC power supplies," IEEE Transaction on Industry Applications, Vol. 37, No. 3, pp. 864–872, May/June 2001.

[5] D. N. Zmood and D. G. Holmes, "Stationary frame current regulation of PWM inverters with zero steady state error," Proceedings of PESC'99, SC, USA, pp. 1185–1190, 1999.

[6] C. Sun, W. M. Ma, and J. Y. Lu, "Analysis of the unsymmetrical output voltages distortion mechanism of three-phase inverter and its corrections," Proceedings of CSEE, Vol. 26, No. 21, pp. 57–64, November 2006.

[7] Y. Sato, T. Ishizuka, K. Nezu, and T. Kataoka, "A new control strategy for voltage-type PWM rectifiers to realize zero steady-state control error in input current," IEEE Transactions on Industry Applications. Vol. 34, No.3, pp. 480–486, May/June 1998.

J. Electromagnetic Analysis & Applications, 2010, 2: 45-50
doi:10.4236/jemaa.2010.21007 Published Online January 2010 (http://www.SciRP.org/journal/jemaa)

Electrical Impedance Tomography Image Reconstruction Using Iterative Lavrentiev and L-Curve-Based Regularization Algorithm

Wenqin WANG[1,2], Jingye CAI[1], Lian YANG[1]

[1]School of Communication and Information Engineering, University of Electronic Science and Technology of China, Chengdu, China; [2]Henan Key Laboratory of Coal Mine Methane and Fire Prevention, Henan University, Henan, China.
Email: wqwang@uestc.edu.cn

Received June 9th, 2009; revised August 17th, 2009; accepted August 25th, 2009.

ABSTRACT

Electrical impedance tomography (*EIT*) *is a technique for determining the electrical conductivity and permittivity distribution inside a medium from measurements made on its surface. The impedance distribution reconstruction in EIT is a nonlinear inverse problem that requires the use of a regularization method. The generalized Tikhonov regularization methods are often used in solving inverse problems. However, for EIT image reconstruction, the generalized Tikhonov regularization methods may lose the boundary information due to its smoothing operation. In this paper, we propose an iterative Lavrentiev regularization and L-curve-based algorithm to reconstruct EIT images. The regularization parameter should be carefully chosen, but it is often heuristically selected in the conventional regularization-based reconstruction algorithms. So, an L-curve-based optimization algorithm is used for selecting the Lavrentiev regularization parameter. Numerical analysis and simulation results are performed to illustrate EIT image reconstruction. It is shown that choosing the appropriate regularization parameter plays an important role in reconstructing EIT images.*

Keywords: *Electrical Impedance Tomography* (*EIT*), *Reconstruction Algorithm, Iterative Lavrentiev, Regularization Parameter, Inverse Problem.*

1. Introduction

Electrical impedance tomography (EIT) is an imaging technique which determines the electrical conductivity and permittivity distribution within a medium using electrical measurement from a series of electrodes on its surface [1—3]. Electrodes are brought into contact with the surface of the object being imaged. A set of voltage (or current) are applied and the corresponding currents (or voltage) are measured [4]. These voltages and currents are then used to estimate the electrical properties of the object using an image reconstruction algorithm [5]. The relatively poor spatial resolution of the reconstructed images in EIT is often quoted as its major disadvantages, compared with already established scanners with good resolution. In this respect, it must be clarified that the motivation of EIT is somewhat different from that of the conventional imaging techniques. Despite its limited resolution, its task is to provide a reliable, real-time, portable and cost efficient imaging tool. Depending on the particular application and the resolution specifications, EIT can sometimes provide an optimum cost-effective imaging solution. Example application areas include geophysical inversion [6], industrial process monitoring [7], and medical diagnosis [8].

However, the process of property estimation in EIT is a highly nonlinear, ill-conditioned, and ill-posed problem. The sensitivity matrix, which relates interior admittivity perturbations to perturbations in the boundary data, is heavily ill-conditioned with respect to inversion. So, it requires special treatment in the form of regularization or a truncation of a singular value expansion [9]. When approaching an ill-posed problem, instead of attempting to solve the original problem one often opts to solve a similar one which is less demanding. Therefore, effective EIT image reconstruction algorithms are required.

Some papers on image reconstruction algorithms have been published [10–14], but little work on EIT image reconstruction is published. The first proposed EIT re-

This work was supported in part by the Open Fund of the Henan Key Laboratory of Coal Mine Methane and Fire Prevention, Henan University under the contract number of *HKLGF*200803.

construction algorithm is the equipotential back-projection [15]. This technique reconstructs images by projecting the change in measurements at each electrode pair across the equipotential region for that current injection pattern, multiplied by an image filter. However, unlike the X-ray used in CAT scanning or general inverse scattering problems [16]. Currents in EIT do not move in a line, but cover the region from the current source to drain. A bias is thus introduced into the image since the equipotential region is an approximation to the region producing the measurement change at each electrode. A finite element-based reconstruction algorithm was proposed in [7], but limited scalar/vectors can be reconstructed with this algorithm. A reconstruction algorithm for breast tumor imaging based on linearization approach was proposed in [8], but the number of independent conductivity regions that can be calculated is too small. In [17] it was assumed that the resistivity distribution could be well approximated as a linear combination of some preselected basis functions. Prior information on the structures and conductivities were used for the construction of these basis functions. The disadvantage of this method is that one may obtain misleading results when prior information is incompatible.

In this paper, we propose an iterative Lavrentiev regularization-based algorithm to reconstruct EIT images using knowledge of the noise variance of the measurements and the covariance of the conductivity distribution. As the regularization parameter should be carefully chosen, an L-curve-based optimization algorithm is applied. Numerical analysis and simulation results are provided. The remaining sections are organized as follows. Section 2 forms the problem of EIT image reconstruction and outlines the motivations of this paper. Section 3 details the iterative Lavrentiev regularization-based EIT reconstruction algorithm, followed by the simulation examples in Section 4. Finally, Section 5 concludes the whole paper.

2. Electrical Impedance Tomography (EIT)

Taking EIT imaging in medical applications as an example [18,19], different tissues of the body are shown to have different electrical characteristics. Most tissues can be considered isotropic with the exception of muscles and brain tissue which are anisotropic. It is usually assumed to be homogenous and isotropic, where the constitute parameters such as the conductivity and permittivity are independent of position and direction. Therefore, the underlying relationships that govern the interaction between EIT electricity and magnetism are the Maxwell's equations. The medium (Ω) is modeled as a closed and bounded subset of three-dimensional space with smooth boundary ($\partial\Omega$) and uniform conductivity (s). The electric field (E) enclosed in Ω is expressed in terms of the scalar potential f

$$E = -\nabla f , \tag{1}$$

where

$$\nabla = i\frac{\partial}{\partial x} + j\frac{\partial}{\partial y} + k\frac{\partial}{\partial z} \tag{2}$$

is the vector differential operator, and f is the potential in the medium. The current (J) is given by the multiplication of the conductivity. The electric field can then be computed as

$$J = -s\nabla f . \tag{3}$$

As there are no interior current sources, EIT simulation in the medium can be described in terms of a scalar voltage potential satisfying Kirchoff's voltage law

$$\nabla \cdot s\nabla f = 0 . \tag{4}$$

The boundary current density (j) can then be represented by

$$j = s\nabla f \cdot n . \tag{5}$$

According to this relationship, the problem of determining the potential inside the medium from boundary measurements can then be carried out [20].

3. Iterative Lavrentiev Regularization and L-Curve-Based EIT Image Reconstruction

To apply regularization-based image reconstruction methods, EIT problems can be formulated as a system of linear equations [21]

$$\begin{bmatrix} A_M + A_Z & A_v \\ A_V^{'} & \mathrm{A_D} \end{bmatrix} \cdot \begin{bmatrix} X \\ V_L \end{bmatrix} = \begin{bmatrix} 0 \\ I^d \end{bmatrix} \tag{6}$$

where $X \in \mathbb{R}^n$ is the nodal potential distribution, $V_L \in \mathbb{R}^n$ is the potential values on the boundary electrodes, A_Z, A_V and A_D are the local matrices. This equation can be represented by

$$AX + x = L \tag{7}$$

where x is the error in the data with $X = [U \quad \mathrm{V_L}]^* \in \mathbb{R}^{n+m}$ and $L = [0 \quad \mathrm{I_d}]^* \in \mathbb{C}^{n+m}$. One standard approach used to solve linear estimation problems is the least square estimation, but this estimate is unsatisfactory because the calculated independent conductivity region is too small.

The inverse of the A cannot be directly computed because the singular values will grow without bound. This will amplify the noise components in the solution associated with the numerical null space of A. That is to say,

small measurement perturbations $L \approx L + e$ may produce large variations in X such that the 3-norm residual error $\|AX - L\|_2$ is unbounded. Therefore, the matrix $A^T A$ is poor conditioned because EIT makes current injection and measurement on the medium surface including higher current densities near the surface where conductivity contrasts will result in more signal than for contrasts in the center. This problem can be resolved by regularization [22]. That is, assume A is an invertible and real-valued matrix, it can then be decomposed by singular value decomposition (SVD)

$$A = U\mathrm{diag}(s_i)V^T \tag{8}$$

Correspondingly, Equation (7) can be expressed by

$$A^{-1}L = V\mathrm{diag}(s_i^{-1})U^T L = X + \sum_{i=1}^{n} s_i^{-1}(u_i^T h)v_i \tag{9}$$

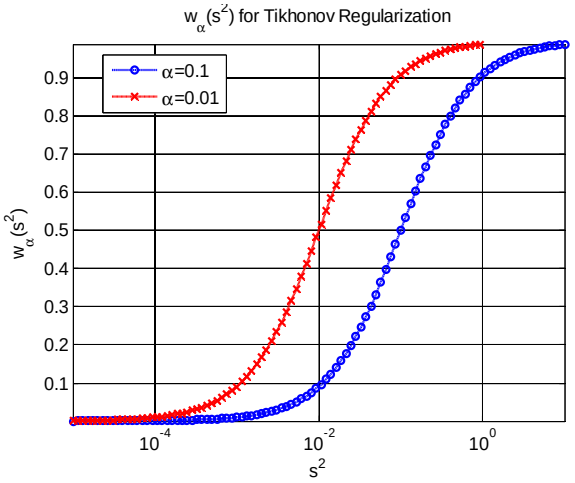

Figure 1. Tikhonov-based regularization filter $w_a(s^2)$ at different a

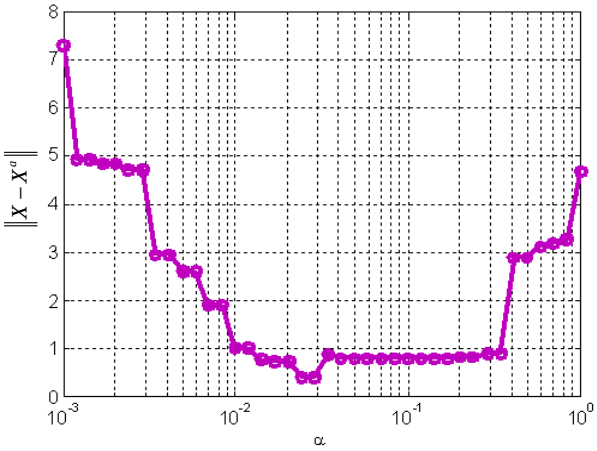

Figure 2. The norm of the regularization solution errors as a function of the regularization parameter of a

As instability may arises due to division by small singular values, to overcome this problem we apply an iterative Lavrentiev-based regularization algorithm.

Lavrentiev regularization replaces Equation (7) by [23]

$$AX^a + aX^a = L, \tag{10}$$

where a is the regularization parameter. Correspondingly, the iterative Lavrentiev regularization is

$$(A + aI)X_k = aX_{k-1} + L, \qquad k = 1,2,3,..... \tag{11}$$

This equation can be changed into

$$X_k = a(A + aI)^{-1}X_{k-1} + (A + aI)^{-1}L, \quad k = 1,2,3,..... \tag{12}$$

Suppose the solution of the Equation (7) is X

$$\begin{aligned} X - X_k &= X - a(A + aI)^{-1}X_{k-1} + (A + aI)^{-1}b \\ &= \left(\frac{a}{a + A}\right)^k X = \left(\frac{a}{a + A}\right)^k A^v X' \end{aligned} \tag{13}$$

where X' is the normalized function with $v > 0$. Note that v refers to the smoothness source conditions. Considering the function

$$F(A) = \left(\frac{a}{a + A}\right)^k A^v \tag{14}$$

when $A = \frac{v}{k - v}a$, it arrives its maximum

$$F_{\max}(A) = v^v \left(\frac{a}{k - v}\right)^v \left(\frac{k - v}{k}\right)^k \tag{15}$$

Hence, we have

$$\begin{aligned} \|X - X_k\| &= \left\|\left(\frac{a}{a + A}\right)^k A^v X'\right\| \\ &\le v^v \left(\frac{a}{k - v}\right)^v \left(\frac{k - v}{k}\right)^k \\ &\le M_v \left(\frac{a}{k}\right)^v, \end{aligned} \tag{16}$$

where M_v is a constant parameter for the specific v. Therefore, this algorithm is converged with a convergence rate of

$$\|X - X_k\| = O(k^v) \tag{17}$$

In fact, the Lavrentiev regularization just uses the filter function

$$w_a(s^2) = \frac{s^2}{s^2 + a} \tag{18}$$

with a regularization parameter of a, as shown in Figure 1. In conventional regularization-based reconstructed algorithms, the regularization parameter is often heuristically selected; however, it determines the cut-off of the filter, as shown in Figure 2. Further analysis results show that when the regularization parameter is very small, filtering of the noise will be inadequate and X^a will be highly oscillatory. In contrast, when the regularization parameter is too large, the reconstructed image will be overly smooth. Therefore, some effective algorithms should be developed to optimize the regularization parameter. To reach this aim, we apply an L-curve [24]-based optimization algorithm.

L-curve is a parametric plot of the squared norm of the regularized solution against the squared norm of the regularized residual for a range of values of regularization parameter. The L-curve criterion for regularization parameter selection is to pick the parameter value corresponding to the "corner" of this curve. Let X^a denote the regularized solution and let $r_a = HX^a - Y$ denote the regularized residual. Define

$$R(a) = \|r_a\|^2, \quad r(a) = \log\left[R(a)\right] \tag{19}$$

$$S(a) = \left\|X^a\right\|^2, \quad h(a) = \log\left[S(a)\right] \tag{20}$$

We can then select the value of a that maximizes the curvature function

$$k = \frac{\mu' \$'' - \mu'' \$'}{\left[\left(\mu'\right)^2 + \left(\$'\right)^2\right]^{3/2}}, \tag{21}$$

where μ and $\$$ are represented, respectively, by

$$\mu = 2\log\left(\left\|AX - L\right\|\right), \tag{22}$$

$$\$ = 2\log\left(\left\|X\right\|\right), \tag{23}$$

The μ', $\$'$, μ'' and $\$''$ denote the first and second derivatives of μ, $\$$ with respect to a. As shown in Figure 3, the L-curve has two characteristic parts: the more horizontal where the solution is dominated by the regularization errors, the vertical part where the solution is dominated by the right-hand errors. The solutions are over- and under-smoothed, respectively. The corner of the L-curve corresponds to a good balance between minimization of the sizes, and the corresponding regularization parameter a is a good one. In this way, an optimum regularization parameter a can be optimization determined.

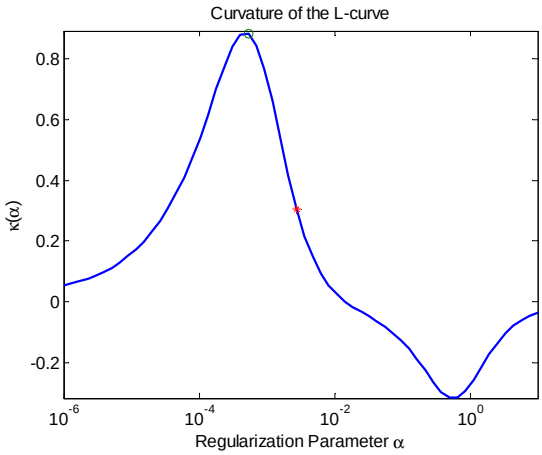

Figure 3. The curvature of the L-curve

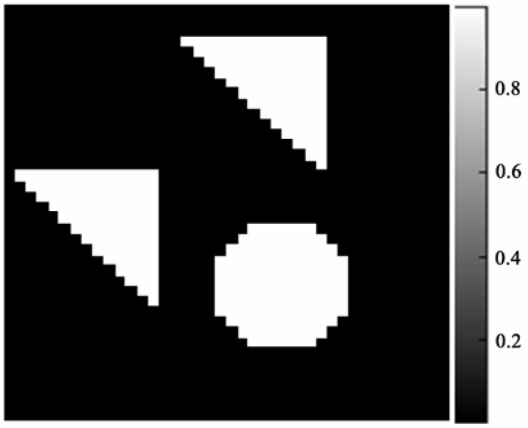

Figure 4. Simulated distribution

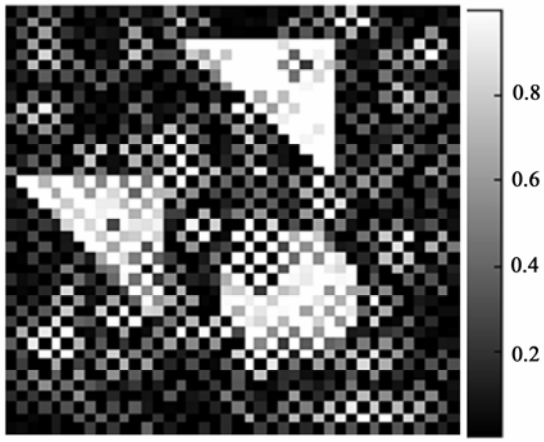

Figure 5. Iterative Lavrentiev reconstructed image with $a = 0.01$

4. Simulation Examples

In many industrial process and biomedical EIT applica-

tions, it is often the case that one knows in advance what materials (tissues) are included within the measurement domain. As mixtures of materials are known to have intermediate conductivities, this effectively restricts the admissible solutions, i.e., the pixels of the reconstructed images, to lie within a set of known values. In this sense, the bound-constrained (with bounds on the values of the admittivity distribution) is to locate the detected inhomogeneities.

As an example, one can allow that the admittivity distribution to be reconstructed is mainly homogenous with an unknown number of shaped inclusions. In EIT applications, the current with a frequency of 10-100kHz is widely used. These patterns are similar to those appearing in Figure 4, which shows the simulated admittivity distribution with the three inhomogeneity patterns. Although the geometry (shape and dimension) of these patterns is assumed to be known a priori, their number, admittivity values and exact location are to be recovered from the

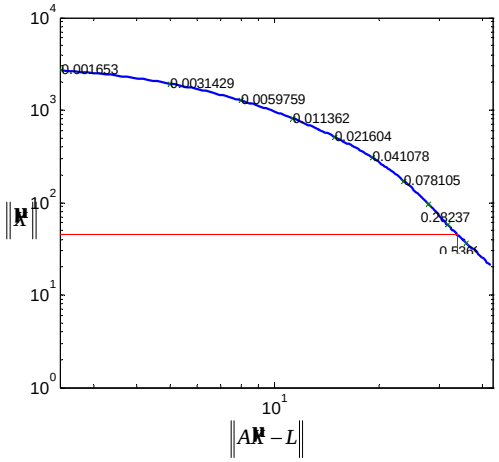

Figure 6. Regularization selection with L-curve-based optimization algorithm

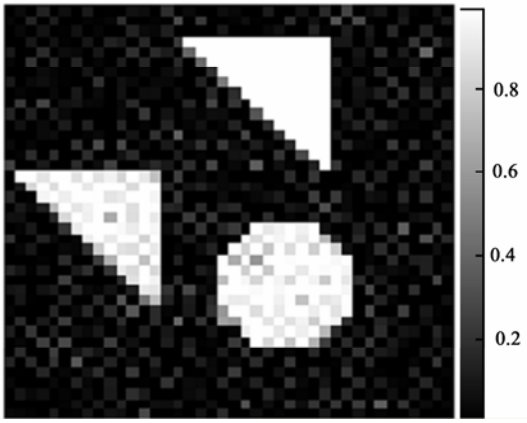

Figure 7. Iterative Lavrentiev reconstructed image with L-curve optimized regularization parameter

image reconstruction. For the reconstructions, simulated measurements contaminated with 2% Gaussian noise have been assumed. Regularization parameter $a = 0.01$ is often used in conventional regularization- based reconstruction methods, e.g., [25], but from Figure 5 we notice that it fails to capture the boundary shape and interior gap of the inhomogeneities. To get around this disadvantage, the regularization parameter is optimized with the L-curve algorithm, as shown in Figure 6. Correspondingly, Figure 7 gives the reconstructed image using the optimized regularization parameter (here is $a = 0.40$). Comparing the two images, the enhancement is obvious. This result comes in support of the fact that this method is robust to noise.

5. Conclusions

EIT is a technique used to create images of the electrical properties in the interior of a medium from measurements on its boundary, which is particularly important for medical and industrial applications [26,27]. Usually a set of voltage or current measurements is acquired from the boundaries of a conductive volume. In this paper, we presented an iterative Lavrentiev regularization and L-curve-based algorithm to reconstruct EIT images using knowledge of the noise variance of the measurements and the covariance of the conductivity distribution. The regularization parameter should be carefully selected, but it is often heuristically selected in conventional regularization-based reconstruction algorithms. So, an L-curve-based optimization algorithm is applied to choose the Lavrentiev regularization parameter. The method is validated with numerical analysis and simulation results. Further research efforts are planned to focus on experimental investigations [28,29] and other computational electromagnetic-based algorithms [30].

REFERENCES

[1] M. Cheney, D. Isaacson and J. C. Newell, "Cooling water system design," SIAM Review, Vol. 41, pp. 85–101, 1999.

[2] S. Jaruwatanadilok and A. Ishimaru, "Electromagetic coherent tomography array imaging in random scattering media," IEEE Antennas and Wireless Propagation Letters, Vol. 7, pp. 524–527, 2008.

[3] B. H. Brown, "Medical impedance tomography and process impedance tomography: a brief review," Measurement Science and Technology, Vol. 12, pp. 991–996, 2001.

[4] E. Martini, G. Carli and S. Maci, "An equivalance theorem based on the use of electric currents radiating in free space," IEEE Antennas and Wireless Propagation Letters, Vol. 7, pp. 421–424, 2008.

[5] U. A. Ahsan, S. Toda, T. Takemae, Y. Kosugi and M. Hongo, "A new method for electric impedance imaging

using an eddy current with a tetrapolar circuit," IEEE Transaction on Biomedical Engineering, Vol. 56, No. 2, pp. 400–406.

[6] P. Metherall, D. C. Barber, R. H. Smallwood and B. H. Brown, "Three dimensional electrical impedance tomography," Nature, Vol. 380, pp. 509–512, 1996.

[7] N. K. Soni, K. D. Paulsen, H. Dehghani and A. Hartov, "Finite element implementation of Maxwell's equations for image reconstruction in electrical impedance tomography," IEEE Transaction on Medical Imaging, Vol. 25, No. 1, pp. 55–61, 2006.

[8] M. H. Choi, T. J. Kao, D. Isaacson and G. J. Saulnier, "A reconstruction algorithm for breast cancer imaging with electrical impedance tomography in mammography geometry," IEEE Transaction on Biomedical Engineering, Vol. 54, No. 4, pp. 700–710, 2007.

[9] W. R. B. Lionheart, "EIT reconstruction algorithms pitfalls, challenges and recent developments," Physiological Measurement, Vol. 25, pp. 125–142, 2004.

[10] M. R. Hajihashemi and M. EI-Shenawee, "Shape reconstruction using the level set method for microwave applications," IEEE Antennas and Wireless Propagation Letters, Vol. 7, pp. 92–96, 2008.

[11] G. Wang, L. J. Schultz and J. Qi, "Bayesian image reconstruction for improving detection performance of Muon tomography," IEEE Transaction on Image Processing, Vol. 18, No. 5, pp. 1080–1089, 2009.

[12] S. K. Padhi, A. Fhager, M. Persson and J. Howard, "Measured antenna response of a proposed microwave tomography system using an efficient 3-D FTD model," IEEE Antennas and Wireless Propagation Letters, Vol. 7, pp. 689–692, 2008.

[13] J. Zhou, L. Senhadji, J. L. Coatrieux and L. Luo, "Iterative PET image reconstruction using translation invariant wavelet transform," IEEE Transaction on Nuclear Science, Vol. 56, No. 1, part 1, pp. 116–128, 2009.

[14] J. Trzasko and A. Manduca, "Highly undersampling magnetic resonance image reconstruction via homotopic l_0 -minization," IEEE Transaction on Medical Imaging, Vol. 28, No. 1, part 1, pp. 106–121, 2009.

[15] Adler and R. Guardo, "Electrical impedance tomography regularized imaging and contrast detection," IEEE Transaction on Medical Imaging, Vol. 15, No. 2, pp. 170–179, 1999.

[16] M. Benedetti, M. Donelli, D. Lesselier and A. Massa, "A two-step inverse scattering procedure for the qualitative imaging of homogenous cracks in known host media-preliminary results," IEEE Antennas and Wireless Propagation Letters, Vol. 6, pp. 592–595, 2007.

[17] M. Vauhkonen, J. P. Kaipio, E. Somersalo and P. A. Karjalainen, "Electrical impedance tomography with basis constraints," Inverse Problems, Vol. 13, pp. 523–530, 1997.

[18] P. M. Edic, G. J. Saulnier, J. C. Newell and D. Isaacson, "A real-time electrical impedance tomography," IEEE Transaction on Biomedical Engineering, Vol. 42, No. 9, pp. 849–859, 1995.

[19] R. D. Cook, G. J. Saulnier, D. G. Gisser, J. C. Goble, J. C. Newell, and D. Isaacson, "ACT3: a high-speed, high- precision electrical impedance tomography," IEEE Transaction on Biomedical Engineering, Vol. 41, No. 9, pp. 713–722, 1994.

[20] L. Di Rienzo, S. Yuferev, N. Ida, "Computation of the impedance mxtrix of multiconductor transmisson lines using high-order surface impedance boundary conditions," IEEE Transaction on Electromagnetic Compatibility, Vol. 50, No. 4, pp. 974–984, 2008.

[21] N. Polydorides, Image reconstruction algorithms for soft-field tomography, Ph. D thesis, University of Manchester Institute of Science and Technology, 2002.

[22] Y. Z. O'Connor and J. A. Fessler, "Fast predictions of variance images for fan-beam transmission tomography with quadratic regularization," IEEE Transaction on Medical Imaging, Vol. 26, No. 3, pp. 335–346, 2007.

[23] S. Morigi, L. Reichel and F. Sgallari, "An iterative Lavrentiev regularization method," BIT, Vol. 43, No. 2, pp. 1–14, 2002.

[24] P. C. Hansen and D. P. O'Leary, "The use of l-curve in the regularization of discrete ill-posed problems," SIAM Journal on Scientific Computing, Vol. 14, No. 6, pp.1487–1503, 1993.

[25] P. C. Hansen, "Rank-deficient and discrete ill-posed problems: Numerical aspects of linear inversion," SIAM, Philadelphia, 1998.

[26] V. Kolehmainen, M. Lassas and P. Ola, "Electrical impedance tomography problem with inaccuracy known boundary and contact impedance," IEEE Transaction on Medical Imaging, Vol. 27, No. 10, pp. 1404–1414, 2008.

[27] F. Ferraioli, A. Formisano, and R. Martone. Ramos, "Effective exploitation of prior information in electrical impedance tomography for thermal monitoring of hyperthermia treatments," IEEE Transaction on Magnetics, Vol. 45, No. 3, pp. 1554–1557, 2009.

[28] E. Hartinger, R. Guardo, A. Alder, and H. Gagnon, "Real-time management of faulty electrodes in electrical impedance tomography," IEEE Transaction on Biomedical Engineering, Vol. 56, No. 2, pp. 369–377, 2009.

[29] P. M. Ramos, F. M. Janeiro, M. Tlemcani and A. C. Seira, "Recent developments on impedance measurements with DSP-based ellipse-fitting algorithms," IEEE Transaction on Instrumentation and Measurement, Vol. 58, No. 5, pp. 1680–1689, 2009.

[30] Ergul, I. van den Bosch and L. Gurel, "Two-step lagrange interpolation method form multilevel fast multipole algorithm," IEEE Antennas and Wireless Propagation Letters, Vol. 8, pp. 69–71, 2009.

J. Electromagnetic Analysis & Applications, 2010, 2: 51-55
doi:10.4236/jemaa.2010.21008 Published Online January 2010 (http://www.SciRP.org/journal/jemaa)

Cation Distribution in Lithium Ferrite ($LiFe_5O_8$) Prepared via Aerosol Route

Sonal Singhal[1,*], Kailash Chandra[2]

[1]Department of Chemistry, Panjab University, Chandigarh, India; [2]Institute Instrumentation Centre, Indian Institute of Technology, Roorkee, India.
Email: sonal1174@gmail.com, chandfuc@iitr.ernet.in

Received July 16th, 2009; revised August 22nd, 2009; accepted September 7th, 2009.

ABSTRACT

Nano size lithium ferrite was prepared through aerosol route and characterized using TEM, XRD, magnetic measurements and Mössbauer spectroscopy. The particle size of as obtained samples were found to be ~10 nm through TEM, that increases upto ~80 nm on annealing at 1200 °C. *The unit cell parameter 'a' calculated using XRD, confirms the formation of a-$LiFe_5O_8$. Room temperature Mössbauer spectra of as obtained sample of all the ferrites exhibited broad doublet suggesting super paramagnetic nature. This doublet further resolved into two doublets and assigned to the surface region atoms and internal region atoms of the particles. The annealed samples (*1200 °C*) show broad sextets, which were fitted with two sextets indicating different local environment of both tetrahedrally and octahedrally coordinated Fe-cation. Cation distribution obtained from the X-ray, magnetic and Mössbauer data confirms that the three fifth of the iron atom goes in to the octahedral site.*

Keywords**:** *Nano Particles, Saturation Magnetization, Coercivity, X-Ray Diffraction, Mössbauer Spectra*

1. Introduction

Lithium iron oxides $LiFe_5O_8$ are of increasing scientific interest and are also promising candidates for cathode materials in rechargeable lithium batteries [1,2]. Its high curie temperature, high saturation magnetization and hysterisis loop properties after performance advantages over other spinel ferrites used in microwave frequency and magnetic core applications [1–4]. Two separate crystallographic ordered and disordered forms of $LiFe_5O_8$ - have been isolated. A super structured form in which lithium and iron atoms are ordered is called α- $LiFe_5O_8$ and has a subgroup of Fd-3m with a primitive cubic unit cell (space group $P4_33$ or $P4_13$, a = 8.3372 Å) [5]. They are based on the inverse spinel structure with lithium and three fifth of the total Fe^{3+} occupying octahedral sites [6]. However, disordered form of lithium ferrites has a random statistical distribution of lithium and iron over all the octahedral positions [7]. Various preparation methods have been developed such as double sintering ceramic techniques, hydrothermal precipitate, hydrothermal ball milling and so on [8,9]. The high temperature used in all these techniques lower the magnetization due to the precipitation of α-Fe_2O_3 or the formation of Fe_3O_4 [10].

The present work deals with the synthesis of nano particles of lithium ferrite via aerosol route at a temperature ~600 °C. This avoids the precipitation of α-Fe_2O_3 or Fe_3O_4. On the other hand in aerosol method particle size, degree of agglomeration, chemical homogeneity can be controlled with relative ease. Aerosol method has the potential of producing multicomponent materials and production of powder by this method is commercially viable [10,11].

The sample so prepared was characterized using transmission electron microscope (TEM), X-ray diffractometer (XRD), magnetic and Mössbauer spectrometer. This work is an attempt to investigate the cation distribution using XRD, magnetic and Mössbauer measurements.

2. Experimental

Nano particles of lithium ferrite ($LiFe_5O_8$) were prepared via aerosol route using a setup described in our earlier papers [12–14]. The desired proportions of lithium and iron nitrates were weighed and dissolved in water to prepare 5 x 10^{-2} M solutions. Air pressure, sample uptake and furnace temperature were maintained at 40 psi, 3-4 ml/min and ~600 °C respectively during preparation. The ferrite powder was deposited on the teflon coated pan.

The elemental analysis was carried out on an electron probe micro analyzer (EPMA) (JEOL, 8600 M) and atomic absorption spectrophotometer (AAS) (GBC, Avanta),

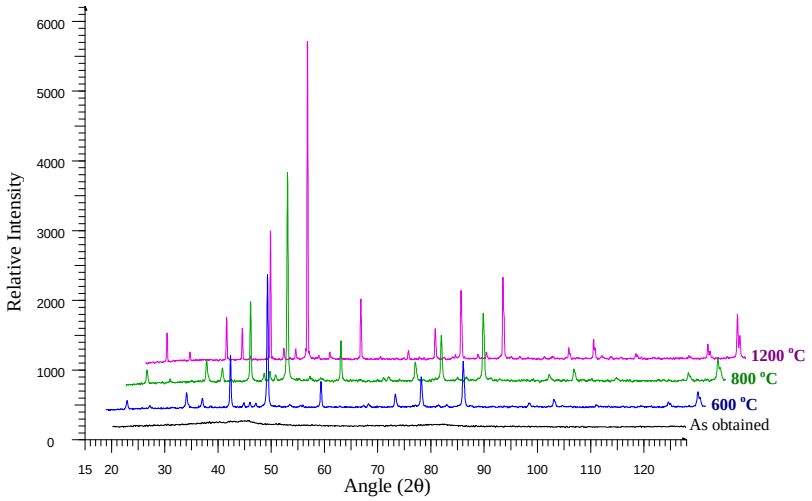

Figure 1. X-ray diffractographs of $LiFe_5O_8$ after annealing at various temperatures

while the particle morphology was examined by transmission electron microscope (TEM) (Philips, EM400). The X-ray diffraction (XRD) studies were carried on X-ray spectrometer (Bruker AXS, D8 Advance) with FeKα radiation and magnetic measurements were made on a vibrating sample magnetometer (VSM) (155, PAR). Mössbauer spectra were recorded on a constant acceleration transducer driven Mössbauer spectrometer using ^{57}Co(Rh) source of 25 mCi initial activity. The spectrometer was calibrated using a natural iron foil as well as recrystallized sodium nitroprusside dihydrate (SNP) as standards.

3. Results and Discussion

Elemental analytical data for Li and Fe were obtained by EPMA. About 2 mm thick pellet was prepared, fixed on the sample holder and coated with the carbon to make them conducting. Elemental analysis was carried out at eight different points on each pellet with spot size of ~10 μm dia and results were found to be consistent. The results were further verified by atomic absorption spectrophotometer.

3.1 Transmission Electron Microscope

The TEM micrograph of a very small amount of as obtained samples placed on the carbon grid shows spherical particles of ~100-300 nm size as reported in our earlier papers [13,14]. However, after agitating ultrasonically and taking the suspended particles on the carbon grid shows well separated particles of size ~10 nm. The micrographs for sample annealed at 1200 ^oC shows that the particle size increases with annealing temperature. It is widely believed that the net decrease in free energy of solid-solid and solid-vapour interface provides the necessary driving force for particle growth during annealing process [15].

3.2 X-Ray Diffractographs

The powder X-ray diffractographs of as obtained sample and that of annealed at various temperatures is given in Figure 1. The diffraction pattern of as obtained samples confirms the amorphous nature of the samples. Peaks start appearing and the lines become sharper as the annealing temperature increases due to the grain growth at higher temperatures. The crystallite size was calculated from the most intense peak (311) using Sherrer equation [16]. It is seen that the particle size increases upto ~80 nm as the annealing temperatures are raised to 1200 ^oC. The lattice parameters were calculated using Powley as well as Le Bail refinement methods (built in TOPAS V2.1 of BRUKER AXS) and found to be a = b = c = 8.33103 Å and V = 578.22 $Å^3$. The data confirm the presence of α-$LiFe_5O_8$ formation. Rietvald analysis of the annealed sample further confirms a single phase cubic spinel structure, α-$LiFe_5O_8$, as given in Figure 2.

X-ray diffraction intensity calculations were carried out using the formula suggested by Buerger [17]

$$I_{hkl} = \left| F_{hkl} \right|^2 PL_p$$

where, notations have their usual meanings. It is well known that, the intensity ratio of planes I(220)/I(400), I(220)/I(440) and I(400)/I(440) are considered to be sensitive to the cation distribution, therefore, these ratios were used in estimating cation distribution. Finally, the cation distribution is estimated from X-ray intensity calculations for the best fit cation distribution and found to be $[Fe_2]^A[LiFe_3]^BO_8$.

3.3 Magnetic Measurements

Magnetic hysteresis loops, at room temperature were recorded for the as obtained as well as annealed sample. Typical loops for as obtained $LiFe_5O_8$ and after annealing at 1200 ^oC are shown in Figure 3. The as obtained sam-

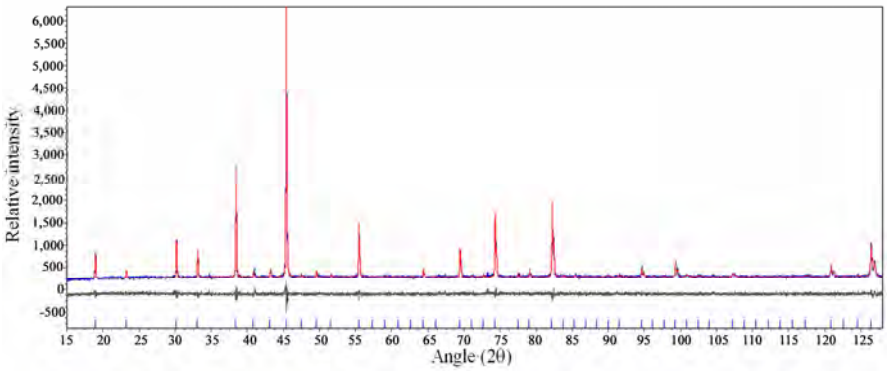

Figure 2. Rietvald analysis of $LiFe_5O_8$ after annealing the sample at 1200 ^{0}C

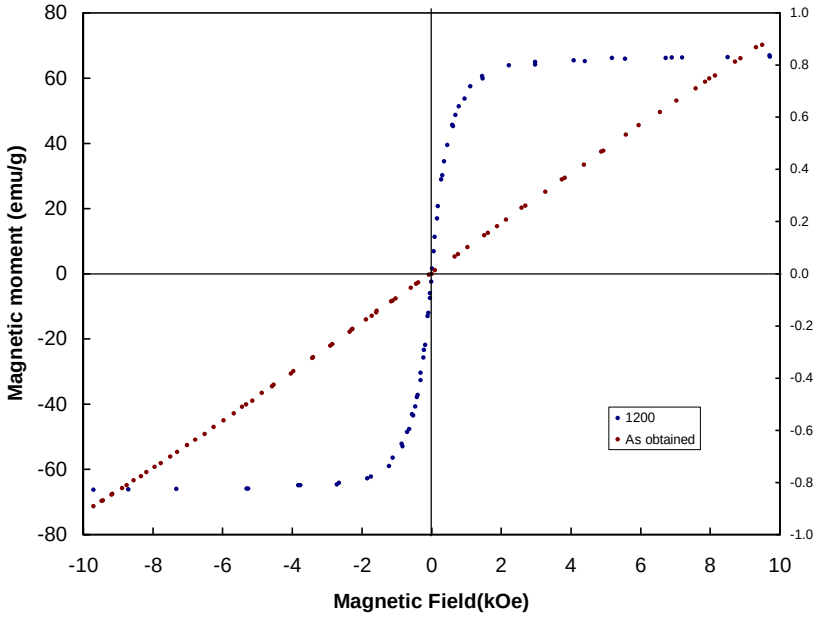

Figure 3. Hysterisis loop of lithium ferrite sample (a) as obtained and (b) after annealing at 1200

ple exhibits no hysteresis, which may be attributed to superparamagnetic relaxation as confirmed by XRD. The values of saturation magnetization and magnetron n_B (the saturation magnetization per formula unit in Bohr magnetron) at 300 K for the annealed sample were obtained from the hysterisis loop and found to be 66.92 emu/g and 4.99 respectively. According to Neel's two sublattice model of ferrimagnetism, the magnetic moment per formula unit (μ_B), $n_B^N(x)$ is expressed as:

$$n_B^N(x) = M_B(x) - M_A(x)$$

where M_B and M_A are the B- and A- sublattice magnetic moment in μ_B respectively. The $n_B^N(x)$ value was calculated using the ionic magnetic moments of Fe^{3+} and Li^+ which are 5 μ_B and 0 μ_B respectively. The calculated value (5 μ_B) clearly indicates the inverse spinel structure with lithium and three fifth of the total Fe^{3+} occupying octahedral sites and two fifth occupying tetrahedral site.

3.4 Mössbauer Spectra

Figure 4 shows the typical Mössbauer spectra of $LiFe_5O_8$ at room temperature for the as obtained sample. The presence of broad doublet in this figure indicates the superparamagnetic nature of the sample. Since in the small particles (<10 nm) a substantial fraction of atoms resides on the surface, a different environment is experienced by them as compared to those inside the particle. Therefore, this broad doublet was fitted with two sets of doublets, one for atoms in the surface region (δ = 0.45 mms^{-1} and ΔE_Q = 1.02 mms^{-1}) and the other for those in the internal region (δ = 0.45 mms^{-1} and ΔE_Q = 0.60 mms^{-1}) of the particles. Larger quadrupole splitting due to surface region atoms compared to internal region atoms can be attributed to the existence of a broader distribution of interatomic spacing and partly disordering in the surface region of the ultrafine particles. It is clear that the contri-

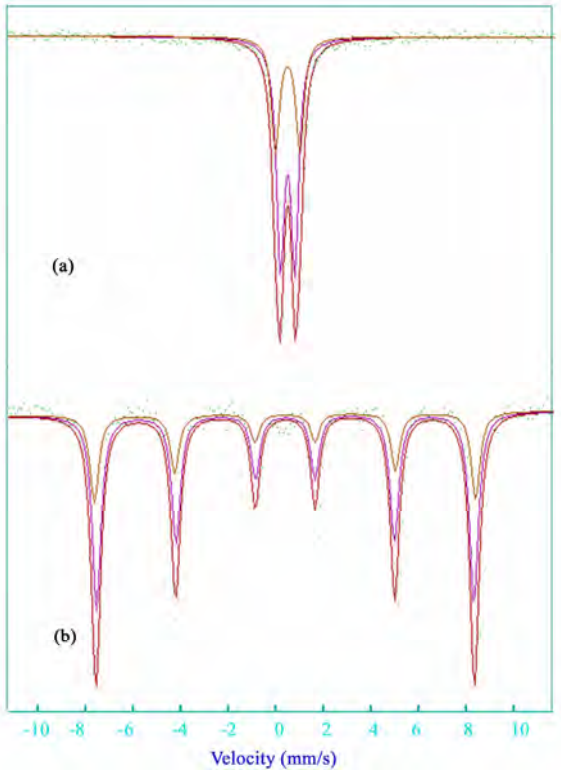

Figure 4. Mössbauer spectra of lithium ferrite (a) as obtained and (b) after annealing at 1200 ^{0}C

bution of surface region atoms is 42 % of total area of the experiment spectrum. This is in agreement with the percentage (44 %) of the volume of surface region atoms to the total volume of the particle with an average grain size (8 nm) by Ma *et al.* [18].

The Mössbauer spectra recorded at 300 K after annealing at 1200 ^{o}C (Figure 4b) exhibit two normal zeeman split sextets due to the A-site Fe^{3+} ions and other due to B-site Fe^{3+} having hyperfine fields 500 and 484 kOe respectively, which indicates ferrimagnetic behaviour of the sample. The cation distribution was also calculated using the intensity ratio of the sextets corresponding to the tetrahedral and octahedral sites. The intensity ratio was found to be 2 : 3 which further confirms that the three fifth iron atoms goes in to octahedral site. The cation distribution obtained from the X-ray intensity data and magnetic moment data agrees fairly well with the cation distribution estimated from Mössbauer data.

4. Conclusions

Lithium ferrite has been prepared successfully with particle size ~10 nm by aerosol route with high yield. After annealing the sample at 1200 ^{o}C confirms the formation of single phase α-$LiFe_5O_8$. The cation distribution obtained from the X-ray, magnetic and Mössbauer data confirms that the three fifth of the iron atom goes in to the octahedral site.

Since Lithium ferrite and mixed lithium ferrites have very high potential for cathode materials in rechargeable lithium batteries, microwave applications and, especially as replacements for garnets, due to their low cost. The squareness of the hysteresis loop and superior temperature performance are other prominent advantages that have made them very promising candidates for application in microwave devices. In this communication we report our studies on the synthesis of lithium ferrite and their magnetic properties and the work is going on with the mixed lithium ferrites to improve their magnetic properties and their applications in different fields.

REFERENCES

[1] P. D. Baba and G. M. Argentina, "Microwave lithium ferrites: An overview," IEEE Transactions Microwave Theory and Techniques, Vol. 22, pp. 652–658, June 1974.

[2] H. M. Widatallah, C. Johnson, F. J. Berry, and M. Pekala, "Synthesis, structural, and magnetic characterisation of magnesium-doped lithium ferrite of composition $Li_{0.5}Fe_{2.5}O_4$," Solid State Communications, Vol. 120, pp. 171–175, October 2001.

[3] V. Berbenni, A. Mariniand, and D. Capsoni, "Solid state reaction study of the system Li_2CO_3/Fe_2O_3," Z. Naturforsch, Vol. 53(a), pp. 997–1003, November 1998.

[4] J. S. Baijal, S. Pehanjoubam and D. Kothari, "Hyperfine interactions and magnetic studies of Li-Mg ferrites," Solid State Communications, Vol. 83, pp. 679–681, September 1992.

[5] H. M. Widatallah and F. J. Berry, "The influence of mechanical milling and subsequent calcination on the formation of lithium ferrites," Journal of Solid State Chemistry, Vol. 164, pp. 230–236, March 2002.

[6] N. K. Gill and R. K. Puri, "D.C. resistivity of Cr^{3+} substituted lithium ferrites," Journal of Materials Science Letters, Vol. 4, pp. 396–398, April 1985.

[7] H. Yang, Z. Wang, M. Zhao, J. Wang, D. Han. H. Luo, and L. Wang, "A study of the magnetic properties of nanocrystalline $LiFe_5O_8$ and $Li_{0.5}Fe_{2.3}Cr_{0.2}O_4$ particles," Materials Chemistry and Physics, Vol. 48, pp. 60–63, March 1997.

[8] A. Ahniyaz, T. Fujwara, S. Song, and M. Yoshimura, "Low temperature preparation of β-$LiFe_5O_8$ fine particles by hydrothermal ball milling," Solid State Ionics, Vol. 151, pp. 419–423, November 2002.

[9] R. Laishram, C. Prakash, S. Phanjoubam, and H. N. K. Sarma, "Mössbauer effect studies on lithium ferrite substituted with chromium and antimony," Modern Physics Letters, Vol. B17, pp. 67–73, January 2003.

[10] E. J. Cukauskas, L. H. Allen, H. S. Newman, R. L. Henry, and P. K. Van Damme, "The properties of $Y_1Ba_2Cu_3O_{7-\delta}$ thin films with silver doping prepared by spray pyroly-

sis," Journal of Applied Physics, Vol. 67, pp. 6946–6952, June 1990.

[11] M. J. Hampden-Smith and T. T. Kodas," Chemical aspects of aerosol synthesis of inorganic materials," Journal of Aerosol Science, Vol. 26, S547–S548, September 1995.

[12] S. Singhal, A. N. Garg and K. Chandra, "Evolution of the magnetic properties during the thermal treatment of nanosize $BaMFe_{11}O_{19}$ (M=Fe, Co, Ni and Al) obtained through aerosol route," Journal of Magnetism and Magnetic Materials, Vol. 285, pp. 193–198, January 2005.

[13] S. Singhal, S. K. Barthwal, and K. Chandra, "Preparation and characterization of nanosize nickel-substituted cobalt ferrites ($Co_{1-x}Ni_xFe_2O_4$)," Journal of Solid State Chemistry, Vol. 178, pp. 3183–3189, October 2005.

[14] S. Singhal, S. K. Barthwal, and K. Chandra," Structural, magnetic and Mössbauer spectral studies of nanosize aluminum substituted Nickel-zinc ferrites," Journal of Magnetism and Magnetic Materials, Vol. 296, pp. 94–103, January 2006.

[15] A. C. F. Costa, E. Tortella, M. R. Morelli, E. F. Neto, and R. H. G. A. Kiminami, "Sintering of Ni-Zn ferrite nanopowders by the constant heating rate (CHR) method, Materials Research," Vol. 7, pp. 523–528, December 2004.

[16] H. P. Klug and L. E. Alexander, "X-ray diffraction procedures for poly crystalline and amorphous materials," Second Edition, Wiley, 1974.

[17] M. G. Buerger, "Crystal structure analysis," Wiley Interscience, New York, 1960.

[18] Y. G. Ma, M. Z. Jin, M. L. Liu, G. Chen, Y. Sui, Y. Tian, G. J. Zhang, and Y. Q. Jia, "Effect of high pressure on Mössbauer spectra of $NiFe_2O_4$ ultrafine particles with different grain sizes, " Materials Chemistry and Physics, Vol. 65, pp. 79–84, June 2000.

J. Electromagnetic Analysis & Applications, **2010, 2: 56-62**
doi:10.4236/jemaa.2010.21009 Published Online January 2010 (http://www.SciRP.org/journal/jemaa)

Synthesis, Permeability and Microstructure of the Optimal Nickel-Zinc Ferrites by Sol-Gel Route

S. ZAHI

Faculty of Engineering and Technology, Multimedia University, Melaka, Malaysia.
Email: souizahi@yahoo.co.uk, souilah.zahi@mmu.edu.my

Received July 22nd, 2009; revised September 15th, 2009; accepted September 20th, 2009.

ABSTRACT

The optimum ferrite can be obtained through free-microstructural defects where such defects are always encountered in the conventional ferrites often caused by chemical inhomogeneity. In this study, Ni-Zn ferrite was synthesized and fabricated by means of a sol-gel route. Thermal gravimetric analysis (TGA) was used to study the thermal transformation of the ferrite in air. Parts of the sol-gel powder heated at elevated temperatures were characterized by X-ray diffraction (XRD) method and Scanning Electron Microscopy (SEM) to reveal the crystallized single-phase and the structure of the obtained ferrite. Fourier transform infrared spectroscopy (FT-IR) was assisted to investigate the structure. The microstructures of the toroidal cores were obtained at two different sintering temperatures and compared with those obtained via the classic method. In addition to that, the magnetic properties were measured. The initial magnetic permeability was found to increase with the increasing of the frequency as a result of the domain wall motions and the corresponding loss was small. Therefore, a well defined polycrystalline microstructure ferrite via an easier preparation methodology as compared to the classic method is obtained.

Keywords*: *Ni-Zn Ferrite, RLF, Eddy Current, Sintering, Initial Permeability, Microstructure

1. Introduction

Nickel-zinc ferrites are the most important soft ferrites whereby the high permeability and low power loss have become the most principal requirements for the electronic devices. However, the metal oxides used in the classical ceramic process, the conventional process, produce deterioration in the final product and its properties as well as the increased handling difficulties in both the preparation and end up usages. Some of these deteriorations include the shrinkage of the materials, variations in the composition and poor homogeneity in both the chemical and crystalline structures, which mainly influence the electrical and magnetic properties [1]. Hence, the challenge is to produce the optimum soft ferrite by making changes in both the metal oxides and manufacturing process.

The sol-gel chemical methods have given numerous advantages in terms of the properties and simplicity of the technique. The attractively sol-gel favors could be represented in the ability to overcome the most drawbacks resulted from the conventional process as well as the ability to produce the nano-sized ferrite particles. The investigations on the nano-crystalline ferrite particles containing nickel and zinc using the sol-gel methods have been given much attention [2–4]. However, the principle requirements of the ferrites have been less reported. Some advantages identified in this study are the homogenous microstructure indicating the ability to better control the electro-magnetic properties as well as the shorter period and temperature of the heat treatments which decrease the variations in the composition and the impurities produced during the preparation. The sol-gel route is relatively a new technique that uses organic compounds to produce ferrite cores, which at the moment imposes a high cost in its chosen starting materials.

The ferrite which contains nickel and zinc was found to form homogenously at lower temperatures and given well controlled properties [5]. In the present paper, an extensive study on the synthesis and measurements of the initial magnetic permeability (μ_i)/ relative loss factor (RLF) were made on toroidal ferrite cores at lower and higher temperatures. The microstructural analyses were reported on the Ni-Zn ferrites prepared via both the sol-gel route at lower and higher temperatures and the classic ceramic process.

2. Experimental Procedures

2.1 Synthesis

The starting materials, $Ni(CH_3COO)_2$, $Zn(CH_3COO)_2$ and

$Fe(CH_3COO)_3$ were weighed to form the spinel single-phase $Ni_{0.3}Zn_{0.7}Fe_2O_4$. These were dissolved for few hours in a small amount of acetic acid, about 5-20 ml, and adding a small amount of water facilitated their dissolutions. The clear solutions were then mixed together and stirred, while the temperature of the solution was raised from the room temperature (30 ^oC) up to 70 ^oC and kept for a few hours. When the solution became viscous, the gel was formed and later taken out and dried at 115 ^oC overnight.

Parts of the dried gel were first calcined at different temperatures ranging from 600 to 1000 ^oC and subjected to the XRD analysis in order to reveal the crystallization of the ferrite. The dried powder was then preheated at the temperature of 600 ^oC maintained for 4 hours in air. The preheated powder was afterwards mixed with polyvinyl alcohol (PVA), dried between 1 and 2 wt. %, crushed and sieved to 75-μm finish. In order to make one toroid with the thickness of 4 mm, the outer diameter of 20 mm and inner diameter of 12 mm, 3.75 g of the sieved powder was blended with 0.3 wt. % of zinc stearate. The granulated powder was subsequently molded and pressed at the pressure of 220 MPa. The toroidal shapes were finally sintered at the different temperatures of 1200 and 1400 ^oC for 4 hours in air. The toroidal cores of the same composition made by the classic ceramic method were prepared to take the Scanning Electron Microscopic (SEM) images.

2.2 Characterization

The gel was thermally analyzed by different analytical technique (TG) in order to characterize the process produced by the heating treatment: A 6 mg sample weight was heated in the Shimadzu TGA-500 up to 900 ^oC in the atmosphere air under the heating rate of 10 ^oC/min. The phase was analyzed by the XRD using Cu K_α radiation on a D8 Advance-Bruker diffractometer. Fourier transform infrared spectroscopic (FT-IR) analyses obtained in nickel-zinc ferrite synthesis were carried out using Perkin Elmer GX Spectrometer. The photomicgraphs of the calcined samples were obtained by the Scanning Electron Microscope (JEOL JSM-6400). Both the initial permeability (μ_i) and loss factor (RLF) were calculated by substituting respectively the corresponding inductance L_p and Q factor values which were measured on the sintered toroids wound with 10 turns of 340 mm long red copper wire, the ends of which scratched using the SiC papers and coated with Tin and finally connected to the HP network spectrum analyzer model 4195A in the frequency range 10-500 MHz on the toroidal ferrite to their resonance frequency. The photomicrographs of the sol-gel and 10-h conventional sintered shapes were obtained on thin samples with the help of the SEM and the grain sizes were measured by the linear intercept method.

3. Results and Discussions

The thermo gravimetric analysis (TGA) curve recorded

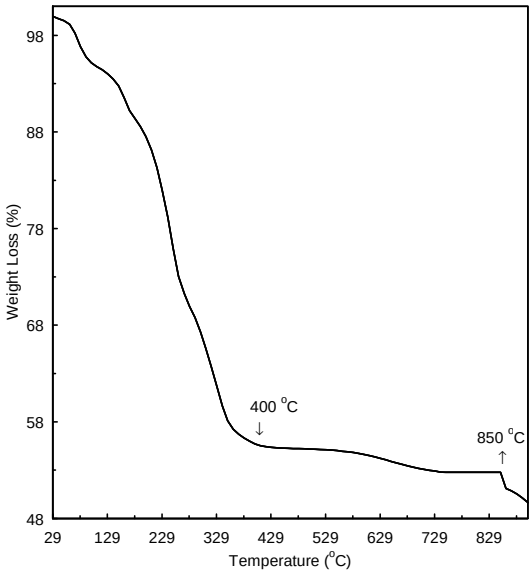

Figure 1. TG curve of the dried gel Ni-Zn ferrite powder

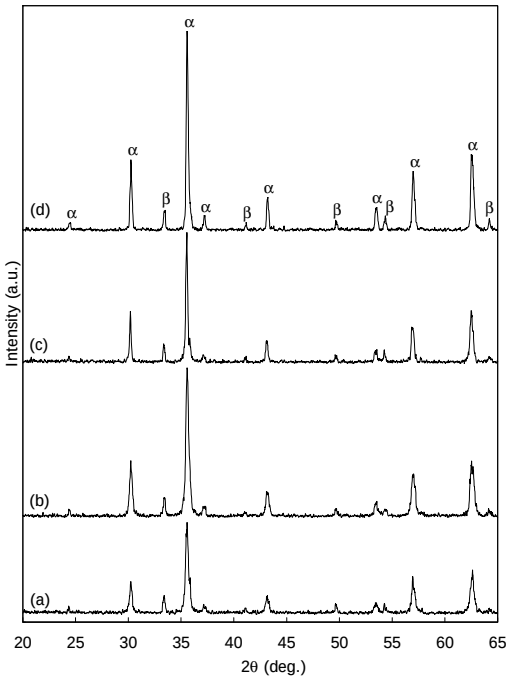

Figure 2. The crystalline phase of Ni-Zn ferrite (α: nickel-zinc ferrite; β: iron oxide) at different heating temperatures: (a) 600 ^oC, (b) 700 ^oC, (c) 800 ^oC, and (d) 900 ^oC for 4 h in air

while heating the dried gel in the air is shown in Figure 1. The thermal transformation can be observed in three stages. The first stage below 400 ^oC was attributed to the evaporation of water and the acetate complex decomposition. The mass losses connected with carboxylate ions and O-H hydroxyl ions lied in the range of 400 to 850 ^oC. The weight of the as-dried Nickel-zinc ferrite considerably decreased above the temperature of 600 ^oC which was

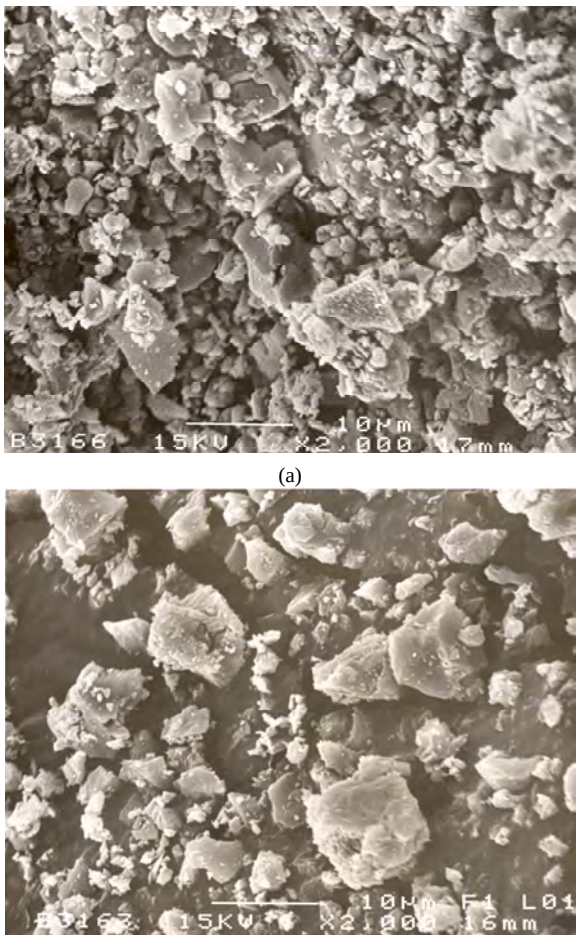

(a)

(b)

Figure 3. Micrographs of Nickel-zinc ferrite calcined at 500 °C

in accordance with the reported results [6]. The sharp decrease above 850 °C indicated the last residual effect.

The XRD spectra of the powder heated at different temperature ranges for 4 h in air are given in Figure 2. In addition, the diffraction patterns of the powder preheated at 600 °C for 4 h are also presented in Figure 2. The diffraction signatures corresponding to the single-phase Nickel-zinc ferrite (α-phase) were detected, indicating the formation of Nickel-zinc ferrite. However, the XRD patterns corresponding to iron oxide Fe_2O_3 (β-phase) were also detected. The ferrite was a solid solution of Ni and Zn metals containing ferric Fe^{3+} as the main element. Thus, the appearance of the secondary phase Fe_2O_3 meant there was more than 50 mole percent of the normal Fe_2O_3 content of the formula of spinel ferrite. On the other hand, the extra iron was to form Fe^{2+} ions in order to control the magnetic properties. The formation of Fe_2O_3 might also be attributed to the insufficient energy needed to attach all Ni and Zn ions with iron oxide to determine the crystal structure, as in this preheating stage the ferrite was usually partially formed where an initial and uniform aggregate of the crystallites related to the formation of Nickel-zinc ferrites occurred as previously demonstrated [5]. Moreover, the major changes observed were the increment in the intensity of the ferrite samples by more than 3 times as the heating temperature was increased. The increase in the intensity means that either the contents of the phases were increased or the concentration of the atoms in alloy was higher. Thus, the reaction was composed with the constituents of the ferrite phase.

The purpose of preheating was also to decompose the carbonates or carboxylate ions which formed from the acetate complex or O-H hydroxyl ions, thus, to start forming the ferrite lattice. Figure 3a represents the SEM micrographs of the Ni-Zn ferrite powders calcined at 500 °C for 4 h. The powder was an aggregation of particles ranging in size from less than 1 micrometer to 10 micrometers. The particles were observed as uniform grains (Figure 3b) confirming the crystalline structure of Nickel-zinc ferrite which were detected by the XRD profile. The formation of Fe_2O_3 was chemically favored during the heating, whereas, the final reaction was completed during the sintering where the pores between the particles were removed combined with growth, and strong bonds between the adjacent particles were formed.

The FTIR spectra are shown in Figure 4 which helps in confirming the formation of the spinel structure in the Nickel-zinc samples. Several absorption bands were recorded in a decreasing number as the calcined temperature increased from 200 to 800 °C. At the temperature of 800 °C, there were two considerable bands appeared at 560 (ν_1) and 2350 cm^{-1} (ν_4) which were assigned to the metal ion-oxygen complexes in the tetrahedral sites− $M_{tetra} \leftrightarrow O-$ and traces of adsorbed or atmospheric CO_2, respectively. The light band at1640 (ν_3) could be attributed to the adsorbed water or humidity [7]. On the other hand, the insensitive broadband (ν_6), around 3400 cm^{-1}, due to $O \leftrightarrow H$ was not observed at the temperature of 800 °C indicating the decomposition of the carboxylate ions.

The initial permeability (μ_i) as a function of frequency for both the ferrites sintered at 1200 °C and 1400 °C is shown in Figure 5. The frequency band was determined up to the value below the resonance frequency. It is evident that both curves have the same trend but the initial permeability values obtained at higher temperatures are higher than the ones at the lower temperatures. The change in the initial permeability (μ_i), or the change in the magnetic flux density (B) represents magnetization by displacing the domain wall which is a boundary between two adjacent domains. Each grain or crystallite in this polycrystalline ferrite contained a number of domains, each differing from its neighbor only in terms of the direction of magnetization. The magnetic field (H) for the initial permeability increased the magnetization through the reversible motion of the walls. The initial permeability increased with the increasing of frequency

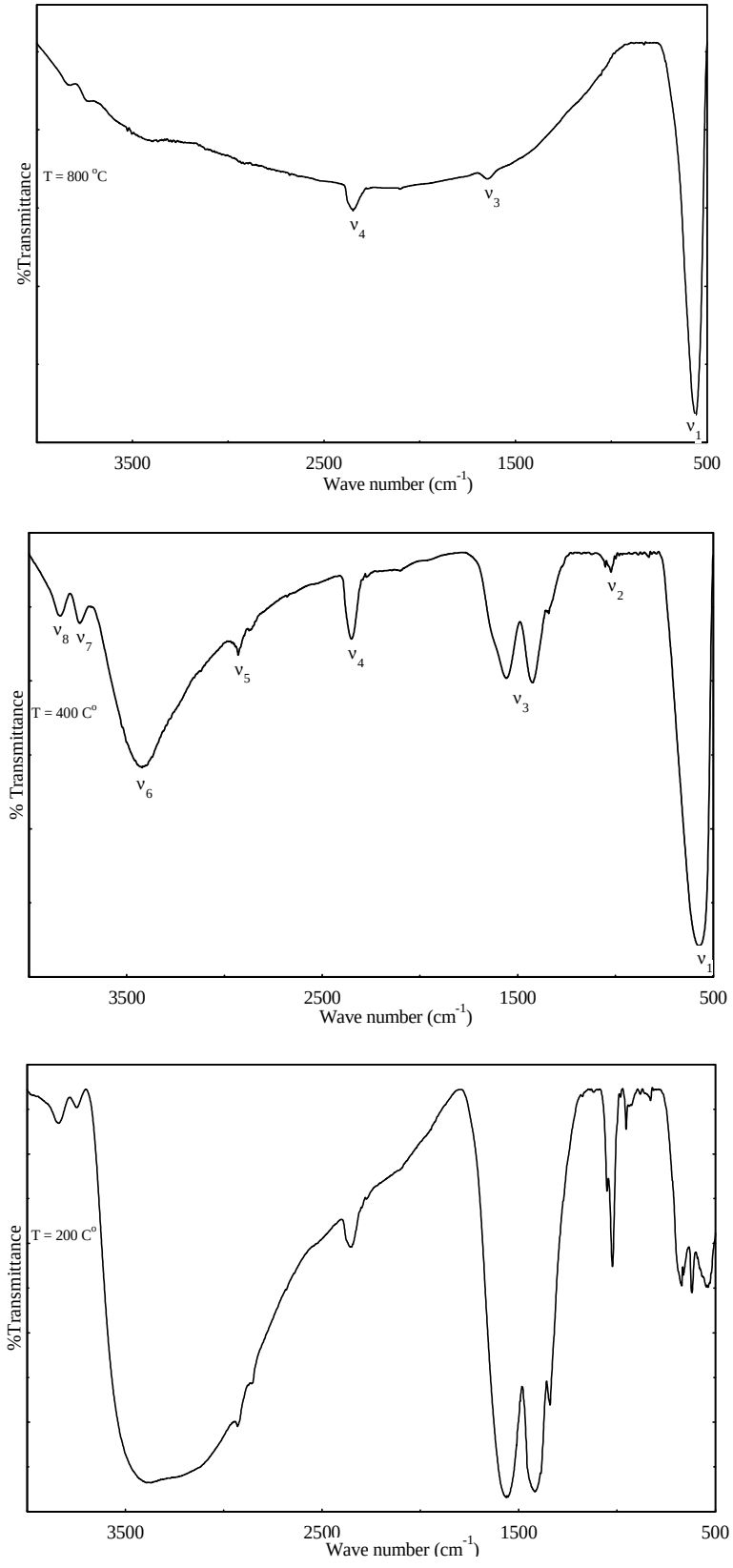

Figure 4. FTIR spectra of Nickel-zinc ferrite at the calcined temperatures of 200, 400, and 800 °C from bottom to top respectively

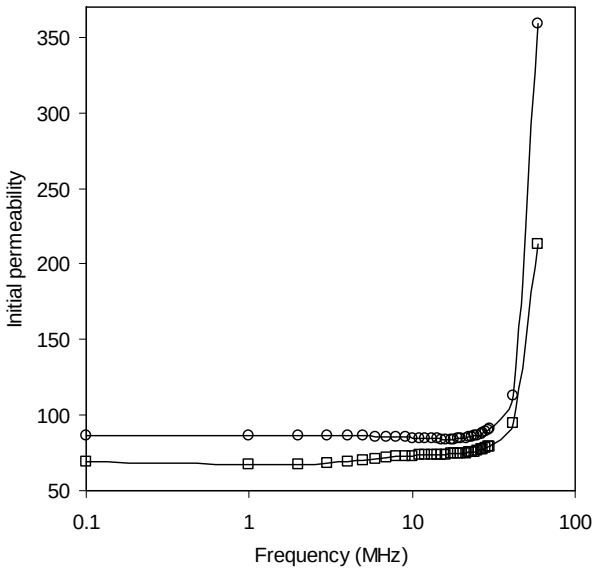

Figure 5. The initial permeability μ_i, versus frequency: □, sintered at 1200 °C; ○, sintered at 1400 °C

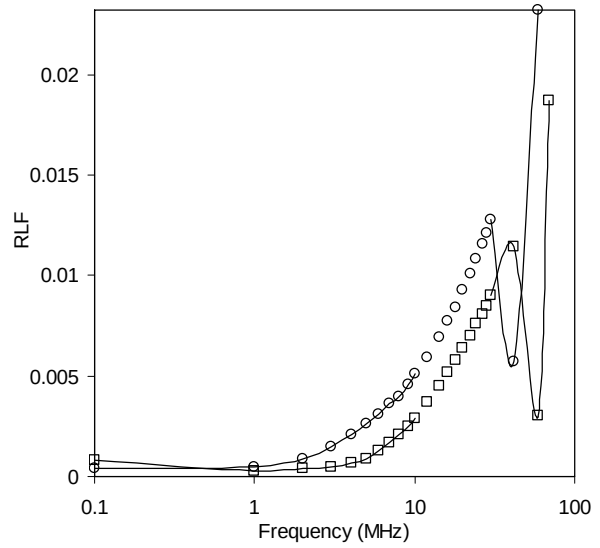

Figure 6. RLF losses versus frequency: □, sintered at 1200 °C; ○, sintered at 1400 °C

as a result of the increase in the size of domains owing to the fact that magnetization was projected along the same direction of the magnetic field. The increase in the magnetization was also due to the moment rotation inside the domains, which was against the anisotropy field.

The high initial magnetic permeability μ_i is determined by the low magnetic anisotropy K_1 and the high saturation of the magnetization B_s (or M_s). Both the magnetic anisotropy and magnetostriction of the ferrites with the same composition are unchangeable at the room temperature, thus, a major contribution to μ_i is from the domain wall movements. Therefore, the increased initial permeability values at the higher temperature were due to the significant change in the domain wall motions. Ahmed [8] reported that the high permeability was attributed to the domain wall contribution, which was controlled by the increased grain size induced by higher post-sintering density. Therefore, the high initial permeability could also be controlled through the microstructure. The relationship between the grain size and initial permeability is generally linear when the grain growth is normal. Both the density and the grain size of the ferrites increased when the sintering temperature increased as many pores and open crystal structures had became closed. As a result, fewer grain boundaries and larger grains led to the higher initial permeability.

The RLF, the energy losses, versus frequency is displayed in Figure 6. The loss factor is usually analyzed into hysteresis, eddy current and residual losses. The residual loss can be considered when both the hysteresis and eddy current losses are very small. As illustrated in Figure 6, the samples prepared at 1200 °C have smaller loss and higher resonant frequency (69 MHz). Besides, the samples prepared at 1400 °C have higher loss and lower resonant frequency (64.7 MHz). The loss measured at 10 kHz is 29 and 51 ($\times 10^{-4}$) for the samples at the lower and higher temperatures, respectively. The hysteresis loss which gives rise to a loss tangent proportional to the peak value of the flux density ($\tan\delta_h \propto \hat{B}$) decreases with the saturation magnetization M_s. Thus, when the sintering temperature increased, the domains or the wall motions were activated, i.e. increasing the magnetization and the magnetic loss. The contribution of the eddy current loss could be estimated via the grain boundary resistivity. Usually, small grains with prominent grain boundaries lead to higher resistivity, the eddy current loss of which is negligible. Therefore, the increased losses in the samples sintered at the higher temperature were mainly due to the significant eddy current as well as the energy lost as the magnetization increased.

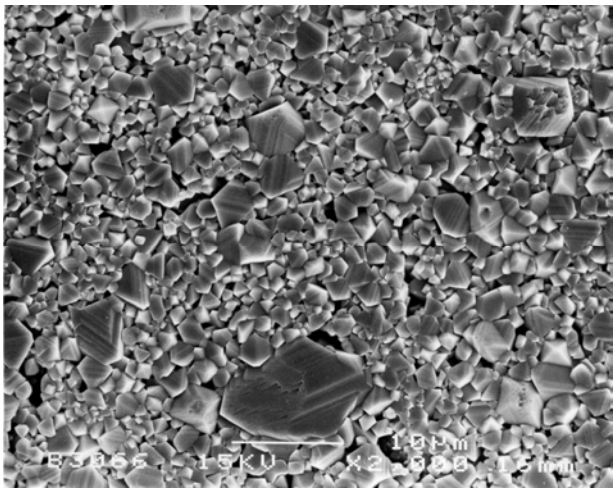

Figure 7. Micrographs of Ni-Zn ferrite sinterd at 1200 °C

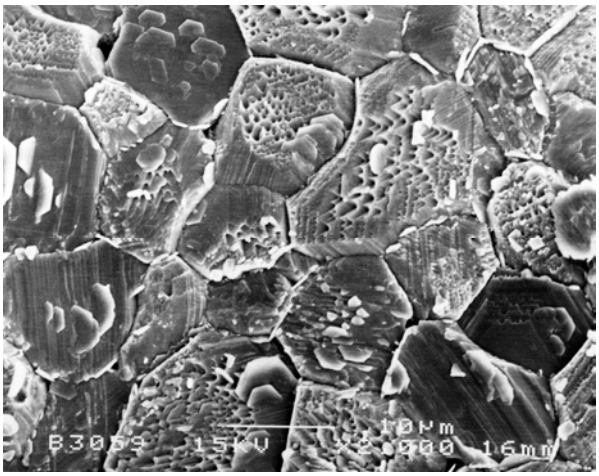

Figure 8. Micrographs of Ni-Zn ferrite sinterd at 1400 ^{o}C

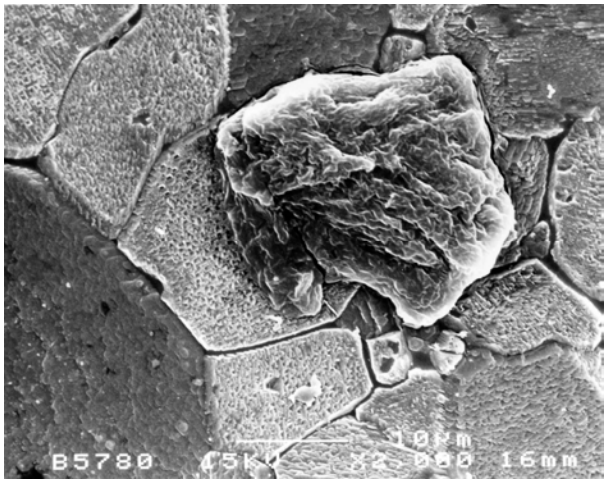

Figure 9. Micrographs of the conventional Ni-Zn ferrite showing segregation

The microstructures of the Ni-Zn ferrites sintered at the lower and higher temperatures are given in Figures 7 and 8, respectively. Both the ferrites showed the grains and the grain boundaries. The grain size measured at 1200 ^{o}C was 1.6 μm indicating smaller grains, while at 1400 ^{o}C was 18.8 μm indicating bigger grains. The microstructure of the same composition which was 10-h conventionally obtained at 1300 ^{o}C is shown in Figure 9.

There were many grains presented (Figure 7) and a large number of grain boundary regions or small contact between the adjacent grains. These small grains are to contain a small number of domains but many grains normally contain many domains. Hence, the grain boundaries acted as the impediment to the domain wall movement, which limited the permeability. The undesirable imperfections that could impede the domain wall motion such as pores, impurities, second phases and other defects such as duplex structure were not signed on both the X-ray signatures and microstructure.

The SEM of the ferrite sintered at the higher temperatures (Figure 8) showed larger grains with intragranular pores (i.e., on grains). There were fewer grains and higher adjacent contacts which led to the higher permeability. The high temperature caused a rapid grain grow in some grains; they are bigger than the other narrow grains. This led to many intragranular pores which possibly contributed in decreasing permeability and increasing the losses. On the other hand, such pores were not seen in the ferrite sintered at the lower temperatures, except for the intergranular pores (i.e., between grains) which were observed and could be eliminated by increasing the presintering temperature. Therefore, these facts suggest a very high homogeneity as the microstructure is also similar in the final composition.

In the conventional ferrite, the impurities presented in the raw materials would be present in the finished ferrite which put a considerable burden to produce a good quality ferrite. Conventionally, the duplex structure (Figure 9) which has some very large grains in the matrix of fine grains is mostly due to the segregation of a particular impurity such as SiO_2. Goldman [9] proved that the segregations could affect the surrounding area, trap pores, and limit permeability by pinning domain walls and increases losses. At still higher concentration, the impurity SiO_2 could be reacted with any additives such as CaO, possibly through the formation of $CaSiO_3$, which led to the uncontrolled and undesired electro-magnetic properties.

4. Conclusions

The sol-gel method is convenient for the fabrication of Ni-Zn ferrite optimum cores. The compound $Ni_{0.3}Zn_{0.7}$ ferrite has been studied using TGA, XRD, SEM, and FTIR analyses. In addition, the electromagnetic and microstructural properties of the cores for electronic applications have been investigated. The analysis has led to the conclusions as follows: 1) the crystallized single-phase ferrite was formed at low cost sol gel preparation; 2) the extra Fe^{+3} ions in the normal Fe_2O_3 content of the formula of spinel ferrite led to the formation of secondary phase for the control of the magnetic properties; 3) the high initial magnetic permeability, small magnetic and eddy current losses were obtained at lower temperatures; 4) higher initial magnetic permeability and relatively small magnetic and eddy current losses were further obtained through controlling the grain size; 5) fine-grained microstructures obtained through easier preparation methodology as compared to the conventional ferrite was realized, mainly by reducing time and temperature of the heat treatments and eliminating the mixing and milling steps; and 6) the technique seemed to be further simplified through choosing new starting materials.

5. Acknowledgements

The authors wish to thank Professor A.R. Daud from National University of Malaysia for his help to carry out the FTIR measurements, and Associate Professor M. Hashim from the University Putra of Malaysia for his comments at a stage of the preparation of the manuscript.

REFERENCES

[1] E. E. Sileo, R. Rotelo, and S. E. Jacobo, "Nickel-zinc ferrites prepared by the citrate precursor method," Physica B: Condensed Matter, Vol. 320, pp. 257–260, 2002.

[2] H. E. Zhang, B. F. Zhang, G. F. Wang, X. H. Dong, and Y. Gao, "The structure and magnetic properties of $Zn_{1-x}Ni_xFe_2O_4$ ferrite nanoparticles prepared by sol-gel auto-combustion," Journal of Magnetism and Magnetic Materials, Vol. 312, pp. 126–130, 2007.

[3] J. Azadmanjiri, "Structural and electromagnetic properties of Ni-Zn ferrites prepared by sol-gel combustion method," Materials Chemistry and Physics, Vol. 109, pp. 109–112, 2008.

[4] M. Yu, J. Liu, and S. Li, "Fabrication and characterization of highly ordered $Ni_{0.5}Zn_{0.5}Fe_2O_4$ nanowire/tube arrays by sol-gel template method," Journal of University of Science and Technology Beijing, Vol. 14, pp. 469–472, 2007.

[5] S. Zahi, M. Hashim, and A. R. Daud, "Synthesis, magnetic properties and microstructure of Ni-Zn ferrite by sol–gel technique," Journal of Magnetism and Magnetic Materials, Vol. 308, pp. 177–182, 2007.

[6] Y. P. Fu, C-H. Lin, and C-W. Liu, "Preparation and magnetic properties of $Ni_{0.25}Cu_{0.25}Zn_{0.5}$ ferrite from microwave-induced combustion," Journal of Magnetism and Magnetic Materials, Vol. 283, pp. 59–64, 2004.

[7] M. Jalaly, M. H. Enayati, F. Karimzadeh, and P. Kameli, "Mechanosynthesis of nanostructured magnetic Ni-Zn ferrite," Powder Technology, Vol. 193, pp. 150–153, 2009.

[8] T. T. Ahmed, I. Z. Rahman, and M. A. Rahman, "Study on the properties of the copper substituted Ni-Zn ferrites," Journal of Materials Processing Technology, Vol. 153–154, pp. 797–80, 2004.

[9] A. Goldman, "Modern ferrite technology," Van Nostrand Reinhold, New York, pp. 121–12, 1990.

Call for Papers

Journal of Electromagnetic Analysis and Applications (JEMAA)

ISSN: 1942-0730 (Print), 1942-0749 (Online)
www.scirp.org/journal/jemaa

JEMAA is a professional journal in the field of electromagnetic analysis, testing and application. The goal of this journal is to provide an international platform for engineers and academicians all over the world to promote, share, and discuss various new issues and developments in the field of electromagnetic. This journal is edited to encourage deeper understanding and greater effectiveness in theory analysis, testing, numerical calculation and engineering application that relevant electromagnetic fields.

Editors-in-Chief

Subject Coverage

JEMAA publishes four categories of original technical reports: papers, communications, reviews, and discussions. Papers are well-documented final reports of research projects. Communications are shorter and contain noteworthy items of technical interest or ideas required rapid publication. Reviews are synoptic papers on a subject of general interest, with ample literature references, and written for readers with widely varying background. Discussions on published reports, with author rebuttals, form the fourth category of JEMAA publications. Topics of interest include, but are not limited to:

- Electromagnetic Numerical Analysis
- Multiphysics Coupled Problems
- Electromagnetic Inverse Problems
- Electromagnetic Structure Optimization
- Test Electromagnetic Analysis Method
- Workshop Benchmark Problems
- Electromagnetic Devices
- Electromagnetic Compatibility
- Electromagnetic Nondestructive Testing
- Electromagnetic Material Modelling

Notes for Intending Authors

Submitted papers should not be previously published nor be currently under consideration for publication elsewhere. Paper submission will be handled electronically through the website. All papers will be peer reviewed. For more derails about the submissions, please access the website.

Website and E-Mail

http://www.scirp.org/journal/jemaa jemaa@scirp.org

J. Electromagnetic Analysis & Applications, 2010
Published Online January 2010 in SciRes (http://www.SciRP.org/journal/jemaa).

CONTENTS

Volume 2 Number 1 **January 2010**

9771942073000 05